Electrodeposition of reactive metals and alloys from non-aqueous electrolytes and their applications

Shota Higashino

Electrodeposition of reactive metals and alloys from non-aqueous electrolytes and their applications

Shota Higashino

2020

Contents

Chapter 1

General Introduction

1.1. Advantages of electrodeposition

Electrodeposition is a process to obtain an adherent deposit onto an electrode by reducing metal ion dissolved in an electrolyte. Compared with other dry processes such as vapor deposition, sputtering and chemical vapor deposition, electrodeposition is advantageous in that (1) high vacuum or high temperature is not required, (2) substrates with a complex shape can be used, (3) deposition rate is relatively high, and (4) patterning or microfabrication is possible by using an insulating mask. Owing to these advantages, electrodeposition is a favorable process for obtaining metal films for a variety of applications such as decorative or protective coatings, electric circuits, large surface battery electrodes, and micro electro mechanical systems (MEMS) components.

1.2. Electrodeposition of metals from non-aqueous electrolytes

Although aqueous solutions were most conventional electrolytes for electrodeposition, in the middle 20th century and later, electrodeposition from non-aqueous electrolyte gained research attention with the aim of obtaining reactive metals that cannot be electrodeposited from aqueous systems. The scientific research on non-aqueous electrolytes has also been motivated by the demand of rechargeable batteries. Most simple non-aqueous system was molten salts composed of metal halides, and various reactive metals such as Al, Mg, Ti, and W were obtained from molten salts[1]. One drawback of molten salts is that they need to be maintained at high temperature and the substrate is limited to heat resistant materials. In order to achieve a melting point that is as low as ambient temperature, room temperature molten salt called as ionic liquid (IL) was developed [2]. The lower melting point of ILs is achieved owing to their relatively large ions. In the 1980s, Wilkes developed 1-ethyl-3-methylimidazolium chloride (EMIC)–$AlCl_3$ system, which has low melting point below 0°C, negligible vapor pressure, and wide electrochemical window [3–5]. In the past 20 years EMIC–$AlCl_3$ has been the most popular

IL in which electrochemical behavior of reactive materials such as Al, Li, Zn, and Fe is studied [2].

Molecular organic solvents such as esters, ethers [6], sulfones [7] in which metal halide are dissolved are also known as alternative non-aqueous electrolytes. However, relatively high melting point or low conductivity needs to be addressed in some systems.

Recently, a new class of non-aqueous electrolytes called as deep eutectic solvent (DES) has been studied intensively, with the aim of developing low-cost non-aqueous electrolytes [8,9]. Being deep eutectic means that a mixture of two substances has a significantly lower melting point than those of its single constituent. In this sense DESs are not different from ILs but DESs can contain even electrically neutral molecular substances whereas ILs are composed only of ions. DESs are usually mixtures of quaternary ammonium salt and a metal halide or hydrogen bond donor [9]. The low cost of constituting substances and easy synthesis make DESs suitable for large scale electrochemical applications. In the following sections, electrodeposition from molten salt, IL and DES is described. Al, W and Fe are taken as subjects of scientific and industrial interest.

1.2.1. Aluminum

Al is an important material for industry owing to its high electrical and thermal conductivity, corrosion and oxidation resistance, high reflectivity, and abundance in mineral resource. The possible applications of Al electrodeposition are corrosion protective coating, electric circuit, and Li secondary battery cathode.

Al is an electrochemically negative material with a redox potential of −1.7 V vs. SHE [10], and therefore it is almost impossible to obtain Al by electrodeposition from aqueous solutions. History of Al electrodeposition goes back to development of Al production process, which is known as Hall-Héroult process using $NaF–AlF_3–Al_2O_3$ molten salt. The temperature of this system is as high as 1000°C and thus Al is obtained as liquid on the cathode. Electrodeposition at such a high temperature is not suitable for surface finishing or any other application described above. Molten salts with lower melting temperature have been developed and one representative example is $NaCl–AlCl_3$ and $NaCl–KCl–AlCl_3$ systems, which melt at around 120°C [11]. In these systems, however, the hazardous $AlCl_3$ fume is generated, and it is difficult to obtain a dense and smooth Al film probably because of the high viscosity of the electrolyte [12]. Recently, ILs [13], DESs [14] and other organic solvents such as sulfones [7,15] and ethers [6,16] have become popular as an electrolyte for Al electrodeposition owing to lower melting point and lower vapor pressure. Examples of these electrolytes are shown in Fig. 1–1.

Corrosion protective coating is one of the interesting applications of Al electrodeposition [13]. Researchers have paid significant efforts to obtain dense and smooth Al films by using additives [17,18] or to improve the anticorrosion performance and mechanical durability of Al by eliminating nonmetal impurities [19–21]. In order to improve the corrosion resistance and mechanical durability of Al, alloying of Al with other transition metals seems to be effective. A series of studies on pitting corrosion of sputtered Al alloys showed that alloying of Al with refractory metals such as Cr, Mo and W improves the pitting corrosion resistance of Al significantly and that Al–W alloys with around 10 at.% W have the highest corrosion resistance [22–24]. Many researchers have studied electrodeposition

of binary or ternary Al alloys and a variety of Al alloys have been obtained successfully [13,25]. However, the low solubility of W in electrolytes has made it difficult to obtain Al–W alloys by electrodeposition [26,27].

1.2.2. Tungsten

W has high melting point, high strength, and low thermal expansion ratio. Thus W is widely used as a material for heat-resistant or ultra-hard materials. In recent years, W is also expected to find applications in microfabrication of thin heat sinks and MEMS components [28–30]. However, the high melting point and high hardness of W have made it difficult to process W into a thin film or nanostructure by using conventional techniques. Therefore application of electrodeposition combined with well-developed LIGA (Lithographie, Galvanoformung, Abformung) process is of interest [31].

W is not as electrochemically negative as Al [10], and alloys of W with other transition metals such as Fe–W and Ni–W can be electrodeposited from aqueous electrolytes [32]. However, electrodeposition of pure W from aqueous electrolytes has not been realized, and it is suggested that using non-aqueous electrolytes is necessary. The first electrodeposition of pure W was achieved by Senderoff et al. using a molten fluoride salt in the temperature range of 700–850°C [33]. Since this achievement, researchers have attempted to lower the electrolyte temperature using a variety of molten salt or ILs. Lowest deposition temperature of 250°C was achieved using $ZnCl_2$–NaCl–KCl molten salt [29]. However, this temperature is still harmful to insulating masks used in LIGA process and even lower temperature is needed.

1.2.3. Iron

Fe could be the most essential materials for our civilization, owing to its abundance in mineral resource, relatively low cost of production and recycling, and designability of its physicochemical and magnetic properties by controlling alloying elements. Therefore, electrodeposition of Fe and Fe alloys has been a significant topic.

Fe can be electrodeposited from aqueous electrolytes. However, hydrogen evolution on the cathode can cause hydrogen embrittlement. At the same time, precipitation of Fe hydroxides is also noted due to the local increase of pH at the cathode surface [34]. In addition, it is difficult to obtain Fe alloys containing less noble elements such as Si, Nd and Al, even though these elements are known to improve the magnetic property of Fe and bring about thermoelectric properties [35,36]. These drawbacks and limitations of the conventional aqueous electrolytes have motivated researchers to develop non-aqueous electrolytes for Fe electrodeposition.

Electrochemical behavior of iron in imidazolium and pyrrolidinium based ILs has been investigated [35,37], and electrodeposition of elemental Fe, Fe–Al and Fe–Si alloys was demonstrated in some of them[35,36]. However, these Fe films suffered from powdery morphology probably because the viscosity of the electrolyte is high [35]. The cost of these ILs also needs to be addressed.

Recently, DESs have been becoming popular as an electrolyte for electrodeposition of Fe group metals (Fe, Ni and Co) [9]. The motivation of using DESs seems to be eliminating H_2O from the electrolyte. However, many of the DESs used for Fe electrodeposition in literature contained OH groups as in ethylene glycol or H_2O molecule as in $FeCl_2 \cdot 6H_2O$, and therefore hydrogen evolution can occur in these systems [38,39]. Development of DESs that do not contain protonic species is of interest as a low-cost non-aqueous electrolyte for Fe electrodeposition.

1.3. Objectives of this study

As described above, electrodeposition from low-temperature non-aqueous electrolytes is studied intensively, but some metals and alloys cannot be obtained yet.

In the study described in chapter 2 of this thesis, to begin with, electrodeposition of corrosion resistant Al–W alloy films with a high W content is investigated in EMIC–$AlCl_3$ bath containing W(II) chloride. The electrochemical behavior of W, film morphology, crystallinity, and corrosion properties are investigated. The possibility of electrodeposition of elemental W is also discussed.

The mechanical properties of corrosion protective coatings are important, because mechanical damages penetrating through the film can promote the corrosion of the substrate. In chapter 3, the hardness and Young's modulus of electrodeposited Al–W alloy films are evaluated by using nanoindentation. The effects of W content and microstructure on the hardness and Young's modulus are discussed.

It is expected that the increase in W content of the Al–W alloy films should enhance their properties. However, as described on chapters 2 and 3, the W content of the Al–W alloy films is not higher than ~12 at.% when EMIC–$AlCl_3$ baths with the $AlCl_3$/EMIC molar ratio of 2 are used. A decrease in the $AlCl_3$/EMIC molar ratio is expected to suppress the electrodeposition rate of Al, and therefore, to increase the W content of the resulting films. In chapter 4, electrodeposition in EMIC–$AlCl_3$–W_6Cl_{12} baths with an $AlCl_3$/EMIC molar ratio of 1.5 was carried out to obtain Al–W alloy films with a higher W content.

In chapter 5, a new process to provide the Al–W alloy films with photocatalytic self-cleaning ability is described. Tungsten(VI) oxide (WO_3) is known to have a visible light-driven photocatalytic ability [40–42]. This chapter describes a new process for providing the corrosion-resistant Al–W alloy films with self-cleaning properties through the formation of a WO_3 surface layer. This process is comprised of a chemical dissolution step and heat treatment. Al is selectively removed by dissolution in an acidic solution, and a W-enriched layer is formed at the surface of the Al–W alloy film. Subsequent heat

treatment in air converts the W-enriched surface layer to photocatalytic WO_3. The self-cleaning ability under visible light illumination of the resulting films is investigated.

In chapter 6, the formation of a DES by the mixture of $FeCl_3$ and acetamide is described. This mixture can be expected as a low cost non-aqueous electrolyte for Fe electrodeposition. The physicochemical properties of the mixtures such as melting point, viscosity, and electrical are determined. These properties are discussed with the Fe speciation analyzed by spectroscopic techniques. Electrodeposition of metallic Fe is also demonstrated.

References

[1] R.S. Sethi, Electrocoating from molten salts, J. Appl. Electrochem. 9 (1979) 411–426.

[2] F. Endres, D. MacFarlane, A. Abbott, eds., Electrodeposition from ionic liquids, Wiley, Weinheim, 2008.

[3] J.S. Wilkes, J.A. Levisky, R.A. Wilson, C.L. Hussey, Dialkylimidazolium Chloroaluminate Melts: A New Class of Room-Temperature Ionic Liquids for Electrochemistry, Spectroscopy, and Synthesis, Inorg. Chem. 21 (1982) 1263–1264.

[4] A.A. Fannin, D.A. Floreani, L.A. King, J.S. Landers, B.J. Piersma, D.J. Stech, R.L. Vaughn, J.S. Wilkes, Properties of 1,3-dialkylimidazolium chloride-aluminum chloride ionic liquids. 2. Phase transitions, densities, electrical conductivities, and viscosities, J. Phys. Chem. 88 (1984) 2614–2621. https://doi.org/10.1021/j150656a038.

[5] A.A. Fannin, L.A. King, J.A. Levisky, J.S. Wilkes, Properties of 1,3-dialkylimidazolium chloride-aluminum chloride ionic liquids. 1. Ion interactions by nuclear magnetic resonance spectroscopy, J. Phys. Chem. 88 (1984) 2609–2614. https://doi.org/10.1021/j150656a037.

[6] A. Kitada, K. Nakamura, K. Fukami, K. Murase, AlCl3-dissolved Diglyme as Electrolyte for Room-Temperature Aluminum Electrodeposition, Electrochemistry. 82 (2014) 946–948. https://doi.org/10.5796/electrochemistry.82.946.

[7] S. Shiomi, M. Miyake, T. Hirato, Electrodeposition of aluminum at near-ambient temperature, J. Japan Inst. Light Met. 63 (2013) 234–242.

[8] A.P. Abbott, G. Capper, D.L. Davies, R.K. Rasheed, V. Tambyrajah, Novel solvent properties of choline chloride/urea mixtures, Chem. Commun. (2003) 70–71. https://doi.org/10.1039/b210714g.

[9] E.L. Smith, A.P. Abbott, K.S. Ryder, Deep Eutectic Solvents (DESs) and Their Applications, Chem. Rev. 114 (2014) 11060–11082. https://doi.org/10.1021/cr300162p.

[10] M. Pourbaix, Atlas of Electrochemical Equilibria in Aqueous Solutions, National Association of Corrosion Engineers, 1974.

[11] R.C. Howie, D.W. Macmillan, The electrodeposition of aluminium from molten aluminium chloride/sodium chloride, J. Appl. Electrochem. 2 (1972) 217–222.

[12] M. Ueda, K. Ui, Alminum and Aluminum Alloy Electrodeposition in Low-Temperature Molten Salts and Room-Temperature Ionic Liquids, J. Surf. Finish. Soc. Japan. 60 (2009) 491–496.

[13] T. Tsuda, G.R. Stafford, C.L. Hussey, Review—Electrochemical Surface Finishing and Energy Storage Technology with Room-Temperature Haloaluminate Ionic Liquids and Mixtures, J. Electrochem. Soc. 164 (2017) H5007–H5017. https://doi.org/10.1149/2.0021708jes.

[14] H.M.A. Abood, A.P. Abbott, A.D. Ballantyne, K.S. Ryder, Do all ionic liquids need organic cations? Characterisation of $[AlCl_2 \cdot nAmide]^+$ $AlCl_4^-$ and comparison with imidazolium based systems, Chem. Commun. 47 (2011) 3523–3525. https://doi.org/10.1039/c0cc04989a.

[15] T. Hirato, J. Fransaer, J.-P. Celis, Electrolytic Codeposition of Silica Particles with Aluminum from AlCl3-Dimethylsulfone Electrolytes, J. Electrochem. Soc. 148 (2001) C280–C283. https://doi.org/10.1149/1.1354616.

[16] A. Kitada, K. Nakamura, K. Fukami, K. Murase, Electrochemically active species in aluminum electrodeposition baths of AlCl3/glyme solutions, Electrochim. Acta. 211 (2016) 561–567. https://doi.org/10.1016/j.electacta.2016.05.063.

[17] L. Barchi, U. Bardi, S. Caporali, M. Fantini, A. Scrivani, A. Scrivani, Electroplated bright aluminium coatings for anticorrosion and decorative purposes, Prog. Org. Coatings. 67 (2010) 146–151. https://doi.org/10.1016/j.porgcoat.2009.09.025.

[18] S. Shiomi, M. Miyake, T. Hirato, Electrodeposition of Bright Al-Zr Alloy Coatings from Dimethylsulfone-Based Baths, J. Electrochem. Soc. 159 (2012) D225–D229. https://doi.org/10.1149/2.079204jes.

[19] M. Miyake, H. Motonami, S. Shiomi, T. Hirato, Electrodeposition of purified aluminum coatings from dimethylsulfone-AlCl3 electrolytes with trimethylamine hydrochloride, Surf.

Coatings Technol. 206 (2012) 4225–4229. https://doi.org/10.1016/j.surfcoat.2012.04.027.

[20] C. Kuma, K. Sato, Y. Hanaoka, I. Matsui, Y. Takigawa, T. Uesugi, K. Higashi, Reduction of impurity contents in aluminum plates electrodeposited from a dimethylsulfone-aluminum chloride bath, J. Alloys Compd. 783 (2019) 919–926. https://doi.org/10.1016/j.jallcom.2018.12.355.

[21] C. Kuma, K. Sato, I. Matsui, Y. Takigawa, T. Uesugi, K. Higashi, Ductile electrodeposited Al from a dimethylsulfone bath with trace amounts of tin chloride, Mater. Lett. 244 (2019) 192–194. https://doi.org/10.1016/j.matlet.2019.02.074.

[22] Z. Szklarska-Smialowska, Pitting corrosion of aluminum, Corros. Sci. 41 (1999) 1743–1767. https://doi.org/10.1016/S0010-938X(99)00012-8.

[23] B.A. Shaw, T.L. Fritz, G.D. Davis, W.C. Moshier, The Influence of Tungsten on the Pitting of Aluminum Films, J. Electrochem. Soc. 137 (1990) 1317–1318. https://doi.org/10.1149/1.2086658.

[24] B.A. Shaw, G.D. Davis, T.L. Fritz, B.J. Rees, W.C. Moshier, The Influence of Tungsten Alloying Additions on the Passivity of Aluminum, J. Electrochem. Soc. 138 (1991) 3288–3295. https://doi.org/10.1149/1.2085404.

[25] T. Tsuda, C.L. Hussey, G.R. Stafford, Progress in Surface Finishing with Lewis Acidic Room-Temperature Chloroaluminate Ionic Liquids, ECS Trans. 3 (2007) 217–231. https://doi.org/10.1149/1.2798664.

[26] K. Sato, H. Matsushima, M. Ueda, Electrodeposition of Al-W Alloys in $AlCl_3$-NaCl-KCl Molten Salt Containing WCl_4, ECS Trans. 75 (2016) 305–312. https://doi.org/10.1149/07515.0305ecst.

[27] T. Tsuda, Y. Ikeda, T. Arimura, M. Hirogaki, A. Imanishi, S. Kuwabata, G.R. Stafford, C.L. Hussey, Electrodeposition of Al-W Alloys in the Lewis Acidic Aluminum Chloride-1-Ethyl-3-Methylimidazolium Chloride Ionic Liquid, J. Electrochem. Soc. 161 (2014) D405–D412. https://doi.org/10.1149/06404.0563ecst.

[28] H. Nakajima, T. Nohira, R. Hagiwara, K. Nitta, S. Inazawa, K. Okada, Electrodeposition of metallic tungsten films in ZnCl2-NaCl-KCl-KF-WO3 melt at 250 °C, Electrochim. Acta. 53 (2007) 24–27. https://doi.org/10.1016/j.electacta.2007.04.082.

[29] K. Nitta, T. Nohira, R. Hagiwara, M. Majima, S. Inazawa, Electrodeposition of tungsten from ZnCl2-NaCl-KCl-KF-WO3 melt and investigation on tungsten species in the melt, Electrochim. Acta. 55 (2010) 1278–1281. https://doi.org/10.1016/j.electacta.2009.10.021.

[30] K.A. Arpin, M.D. Losego, P. V. Braun, Electrodeposited 3D tungsten photonic crystals with enhanced thermal stability, Chem. Mater. 23 (2011) 4783–4788. https://doi.org/10.1021/cm2019789.

[31] K. Nitta, T. Nohira, R. Hagiwara, M. Majima, S. Inazawa, Characteristics of a tungsten film electrodeposited in a KF-B2O3-WO3 melt and preparation of W-Cu-W three-layered films for heat sink application, J. Appl. Electrochem. 40 (2010) 1443–1448. https://doi.org/10.1007/s10800-010-0121-y.

[32] N. Tsyntsaru, H. Cesiulis, M. Donten, J. Sort, E. Pellicer, E.J. Podlaha-Murphy, Modern trends in tungsten alloys electrodeposition with iron group metals, Surf. Eng. Appl. Electrochem. 48 (2013) 491–520. https://doi.org/10.3103/S1068375512060038.

[33] S. Senderoff, G.W. Mellors, Electrodeposition of coherent deposits of refractory metals. V. Mechanism for the deposition of molybdenum from a chloride melt, J. Electrochem. Soc. 114 (1967) 556–560. https://doi.org/10.1149/1.2426655.

[34] G. Panzeri, A. Accogli, E. Gibertini, C. Rinaldi, L. Nobili, L. Magagnin, Electrodeposition of high-purity nanostructured iron films from Fe(II) and Fe(III) non-aqueous solutions based on ethylene glycol, Electrochim. Acta. 271 (2018) 576–581. https://doi.org/10.1016/j.electacta.2018.03.174.

[35] P. Giridhar, B. Weidenfeller, S.Z. El Abedin, F. Endres, Electrodeposition and magnetic characterization of iron and iron-silicon alloys from the ionic liquid 1-butyl-1-methylpyrrolidinium trifluoromethylsulfonate, ChemPhysChem. 15 (2014) 3515–3522.

https://doi.org/10.1002/cphc.201402406.

[36] P. Giridhar, B. Weidenfeller, S.Z. El Abedin, F. Endres, Electrodeposition of iron and iron-aluminium alloys in an ionic liquid and their magnetic properties, Phys. Chem. Chem. Phys. 16 (2014) 9317–9326. https://doi.org/10.1039/c4cp00613e.

[37] Z. Guo, T. Zhang, M. Khan, S. Gao, T. Liu, J. Yu, Electrochemical behavior of iron-based imidazolium chloride ionic liquids, Electrochim. Acta. 142 (2014) 132–143. https://doi.org/10.1016/j.electacta.2014.07.110.

[38] M.A. Miller, J.S. Wainright, R.F. Savinell, Iron Electrodeposition in a Deep Eutectic Solvent for Flow Batteries, J. Electrochem. Soc. 164 (2017) A796–A803. https://doi.org/10.1149/2.1141704jes.

[39] R. Böck, S.E. Wulf, Electrodeposition of iron films from an ionic liquid (ChCl/urea/$FeCl_3$ deep eutectic mixtures), Trans. Inst. Met. Finish. 87 (2009) 28–32. https://doi.org/10.1179/174591908X379601.

[40] I.P. Parkin, R.G. Palgrave, Self-cleaning coatings, J. Mater. Chem. 15 (2005) 1689–1695. https://doi.org/10.1039/b412803f.

[41] M. Miyauchi, Photocatalysis and photoinduced hydrophilicity of WO_3 thin films with underlying Pt nanoparticles, Phys. Chem. Chem. Phys. 10 (2008) 6258–6265. https://doi.org/10.1039/b807426g.

[42] P. Dong, G. Hou, X. Xi, R. Shao, F. Dong, WO3-based photocatalysts: morphology control, activity enhancement and multifunctional applications, Environ. Sci. Nano. 4 (2017) 539–557. https://doi.org/10.1039/C6EN00478D.

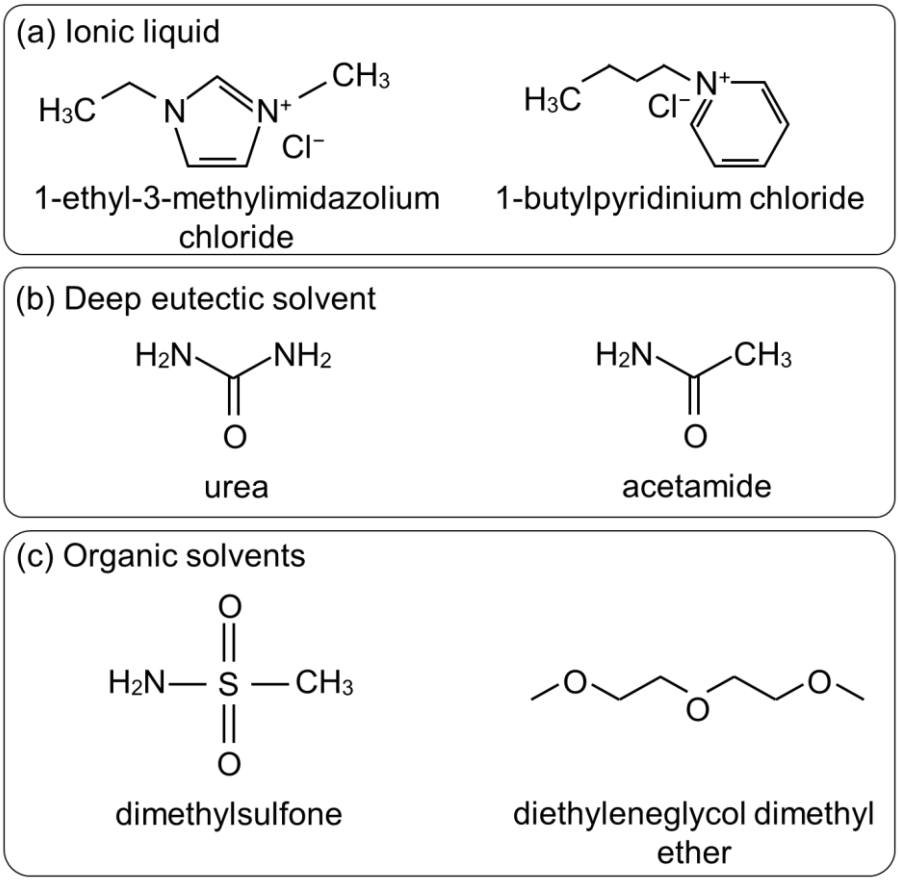

Figure 1–1. Examples of components that form (a) ionic liquid, (b) deep eutectic solvent, and (c) organic solvent used for Al electrodeposition. These components are usually mixed with $AlCl_3$ to prepare electrolytes.

Chapter 2

Electrodeposition of Al–W alloy films using tungsten(II) chloride

2.1. Introduction

Aluminum and its alloys are highly resistant to corrosion and oxidation. Thus they have attracted attention as corrosion-protective coatings for reactive materials such as Mg alloys and steels [1–3]. Among Al-based binary alloys, Al–W alloys containing approximately 10 at.% W are known to have the highest resistance to chloride-induced pitting corrosion [4,5].

Since the maximum solubility of W in Al phases is only 0.022 at.% at 640 °C in the equilibrium state [6], the formation of Al–W alloy films having high corrosion resistances requires non-equilibrium processes, such as sputtering [4,5,7–11], ion implantation [12], laser alloying [13], and electrodeposition [14–19]. Of these methods, electrodeposition is advantageous in that low pressure or high temperature is not required, and a uniform film can be formed onto substrates with a complex shape. Various Al based alloy films have been electrodeposited in molten salts such as NaCl–$AlCl_3$ containing alloying element precursors. Recently, electrodeposition using ionic liquids has become more popular owing to their low melting point and low volatility. A representative ionic liquid used for the electrodeposition of Al alloys is 1-ethyl-3-methylimidazolium chloride (EMIC)–$AlCl_3$ (where the $AlCl_3$/EMIC molar ratio >1). Electrodeposition of Al alloys such as Al–Ni [20], Al–Ti [21], Al–V [21], Al–Zr [22], Al–Mo [23], Al–Mn [24], and Al–Hf [25] has been reported and several review articles are available in literature [3,26–31].

A previous study reported that electrodeposition in an EMIC–$AlCl_3$ bath containing W(IV) chloride (WCl_4) yielded Al–W alloys but the W content was lower than 1 at.% [14]. More recently electrodeposition of Al–W alloy films in an EMIC–$AlCl_3$ bath containing potassium W(III) chloride ($K_3W_2Cl_9$) was reported [15,32]. Although the W content of the resulting Al–W alloys reached nearly 96 at.%, the deposits with high W content had a powdery morphology. When the current density was

high (>20 mA cm^{-2}), dense Al–W alloy films were obtained, but the W content decreased to <3 at.%. This decrease in the W content at high current density was due the rate of W deposition being controlled by the diffusion of W ions. The diffusion-controlled deposition of W was inevitable in this liquid because the saturation concentration of $K_3W_2Cl_9$ was as low as 8 mM at 80 °C.

To electrodeposit dense Al–W alloy films with a high W content, an effective approach could be to use a W ion source that can dissolve in EMIC–$AlCl_3$ at high concentration. In our preliminary experiments, it was found that the solubility of W(II) chloride (W_6Cl_{12}) in EMIC–$AlCl_3$ is significantly higher than that of $K_3W_2Cl_9$. In addition, the oxidation number of W is lower in W_6Cl_{12} (i.e., II) than in $K_3W_2Cl_9$ (i.e., III), and therefore it was expected that W_6Cl_{12} would be reduced more readily to metallic W. In this study, electrodeposition of Al–W alloys in EMIC–$AlCl_3$ containing W_6Cl_{12} was examined. The W content, surface morphology, and crystal structure of the resulting deposits were investigated. Furthermore, the pitting corrosion resistance of the resulting dense Al–W alloy films was evaluated.

2.2. Methods

Preparation of the electrolytic bath

The electrolytic bath was prepared by adding anhydrous aluminum chloride ($AlCl_3$, 99%, Fluka) to EMIC (97%, Tokyo Chemical Industry) at a molar ratio of 2:1. The EMIC was dried under vacuum at 120 °C prior to use. The W ion source, W_6Cl_{12}, was synthesized by a method similar to those described in previous reports [33,34]. Briefly, a mixture of tungsten(VI) chloride (WCl_6, 99.9%, Wako) and bismuth powder (Bi, 99.9%, Wako) at a molar ratio of 3:4 was charged into a two-chamber glass tube and flame-sealed under vacuum. The mixture placed in one chamber was heated in a furnace, first at 280 °C for 2 days and then at 355 °C for more than 5 days. During the heating at 355 °C, WCl_6 was reduced by Bi to produce W_6Cl_{12}, and the byproduct, $BiCl_3$, was sublimed into the other chamber, which was exposed to a lower temperature. After heating, black powder collected from the product chamber was washed with concentrated aqueous HCl at room temperature, and then dissolved in

boiling concentrated aqueous HCl. From the solution, yellow crystals of $(H_3O)_2[W_6Cl_{14}]\cdot 7H_2O$ were recrystallized. The crystals of $(H_3O)_2[W_6Cl_{14}]\cdot 7H_2O$ were heated at 325 °C for 1 h in vacuum, yielding a bright yellow powder of W_6Cl_{12}. EDX confirmed that the Cl/W atomic ratio of the powder was 2. XRD patterns of the powder agreed with that of poorly crystallized W_6Cl_{12} [35]. The synthesized W_6Cl_{12} powder was added to the EMIC–$AlCl_3$ bath until it was saturated.

Electrochemical experiments

Electrochemical experiments using the EMIC–$AlCl_3$–W_6Cl_{12} bath were carried out in an argon-filled glove box (SDB-1AO, MIWA MFG). A glass vessel with a volume of 25 mL was used as an electrolytic cell. The bath temperature was kept at 80 °C by a heater and thermostat (TJA-550, AS ONE) connected to a rubber heater wound around the cell and a thermocouple soaked in the bath. Cyclic voltammograms were recorded using a Pt electrode and an Al plate as the working and counter electrodes, respectively. An Al wire immersed in neat EMIC–$AlCl_3$ (1:2) ionic liquid separated from the bath by a porous glass frit (BAS) was used as the reference electrode. The potential scan was started from the open circuit potential to the cathodic direction at a sweep rate of 10 mV s^{-1}.

Potentiostatic electrodeposition was performed on a mirror polished Cu plate. A section of the Cu plate was covered with PTFE tape so that a certain area (5 mm × 5 mm) would be exposed. An Al plate and the Al wire electrode were used as the counter and reference electrodes, respectively. The Cu plate and Al plate were placed vertically and in parallel with each other. The distance between the Cu and Al plates was less than 10 mm. During the electrodeposition process, the bath was agitated at 150 rpm using a magnetic stirrer (PC-420D, CORNING) and a magnetic flea (15 mm × 5 mm). The electrochemical experiments described above were carried out using an electrochemical analyzer (660c, ALS). After electrodeposition, the deposit was washed with distilled water and ethanol.

Characterization of the deposit

A scanning electron microscope (SEM, S-3500, Hitachi) combined with energy dispersive X-ray

spectroscopy (EDX, INCAxact, Oxford Instruments) was used to observe the morphology and measure the elemental composition of the deposit. X-ray diffraction (XRD) patterns were obtained using an X-ray diffractometer (X'pertPRO-MPD, PANalytical) with Cu-Kα radiation. Some of the deposits were analyzed with X-ray photoelectron spectrometry (XPS; JPS-9010TRX, Nihon Denshi). The partial current density for the deposition of W was calculated from the amount of deposited W, as determined by inductively coupled plasma-atomic emission spectroscopy (ICP-AES; Optima 5300 DV, PerkinElmer). The sample solution for the ICP-AES was prepared by dissolving the deposit in 5 mM aqueous NaOH solution. To promote the dissolution of W, a small amount of H_2O_2 solution was added to the solution. After the deposit was completely dissolved, residual H_2O_2 was vaporized by heating the solution to 70 °C. The pitting corrosion resistance of an Al plate (99.5%, Nilaco) and the Al–W alloy films was evaluated from potentiodynamic polarization curves in 3.5 wt.% aqueous NaCl solution, which was deaerated with bubbling argon gas prior to each experiment. A Pt plate and an Ag/AgCl/sat. KCl electrode were used as the counter and reference electrodes, respectively. The potential scan was started from −0.8 V in the anodic direction at a sweep rate of 0.5 mV s^{-1}. The potential scan was performed using an electrochemical analyzer (HZ-5000, Hokuto Denko).

2.3. Results and discussion

Solubility of W_6Cl_{12} in EMIC–$AlCl_3$

W_6Cl_{12} was added to the Lewis acidic EMIC–$AlCl_3$ (1:2) until it was saturated. The saturation concentration of W_6Cl_{12} was 49 mM at 80 °C. W_6Cl_{12} and Mo_6Cl_{12} have the same atomic arrangement in their crystal structures, which both comprise a $[M_6Cl_8]^{4+}$ core, where M = W or Mo [36,37]. Mo_6Cl_{12} is believed to dissolve in Lewis acidic EMIC–$AlCl_3$ while maintaining the form of the $[Mo_6Cl_8]^{4+}$ core in solution [38]. W_6Cl_{12} should also dissolve in EMIC–$AlCl_3$ in the same manner as Mo_6Cl_{12} by the following reaction:

$$x Al_2Cl_7^- + W_6Cl_{12} = 2x AlCl_4^- + [W_6Cl_8]Cl_{4-x}^{x+} \quad [1]$$

Cyclic voltammetry

Figure 2–1 shows cyclic voltammograms recorded at a Pt electrode in the EMIC–$AlCl_3$ bath before and after the addition of 49 mM W_6Cl_{12}. Before adding W_6Cl_{12} (Fig. 2–1a), the cathodic current rises steeply at −0.1 V during the cathodic scan. After the scan is reversed at −0.2 V, an anodic current with a peak at +0.1 V is observed. These cathodic and anodic currents are due to the deposition and stripping, respectively, of Al. After the addition of 49 mM W_6Cl_{12} (Fig. 2–1b), a small cathodic current is observed in the potential range from +0.4 V to −0.15 V, and the cathodic current rises steeply at −0.15 V. After the scan is reversed, a small anodic current is observed with a peak at +0.4 V. The small cathodic current in the potential range from +0.4 V to −0.15 V is not observed before the addition of W_6Cl_{12}. Therefore, there is a possibility that this cathodic current is caused by the reduction of W ions. The shift in the anodic current peak to a more positive potential upon the addition of W_6Cl_{12} indicates that an Al–W alloy phase is formed during the cathodic scan. By alloying with W, which is more noble than Al, Al becomes more difficult to dissolve during the anodic scan.

Potentiostatic electrodeposition and characterization of the deposits

Potentiostatic electrodeposition was carried out at every 0.1 V in the potential range from −0.5 to +0.4 V vs. Al/Al(III). The amount of charge was set at 8.0 C cm^{-2}, which corresponds to the value required to electrodeposit a 2.8-μm thick pure Al film or a 3.9-μm thick pure W film, assuming 100% current efficiency.

The steady-state cathodic current density is as low as 0.3 mA cm^{-2} at potentials more positive than 0 V. In contrast, at potentials more negative than 0 V, the current density increases with decreasing potential, and reaches 38 mA cm^{-2} at −0.5 V.

Every electrodeposition in the potential range from −0.5 V to +0.4 V yields deposits on the Cu cathode substrates. The appearance of the deposit varies significantly at a potential of 0 V. In the potential range from 0 to +0.4 V, the deposits are black, and exhibit poor adhesion to the substrates. In

the potential range from −0.5 to −0.1 V, the deposits are gray, and exhibit good adherence. The typical EDX spectra of the deposits obtained at potentials: >0 V and <0 V, are shown in Fig. 2–2. EDX shows that all these deposits contain Al and W. The presence of other elements such as Cu and O is also observed, owing to substrate and surface oxidation, respectively. The larger signals of Cu and O from the deposits obtained at potentials >0 V are probably derived from the presence of many cracks in the deposits, as discussed in detail later. The W content calculated by considering the presence of Al and W is plotted against the deposition potential, as shown in Fig. 2–3. The W content of the deposit also changes drastically across 0 V. In the potential range from 0 to +0.4 V, the W content is high (64–92 at.%) with a large scattering. In the potential range from −0.5 to −0.1 V, the W content is low (6.6–12 at.%), and has a small potential dependency.

Figure 2–4 shows the surface SEM images of the deposits. The deposit containing 64 at.% W obtained at +0.1 V (Fig. 2–4a) exhibits many cracks. The enlarged image reveals that some parts of the deposit are exfoliated from the substrate. This cracking and exfoliation are typical for deposits with high W contents electrodeposited at potentials more positive than 0 V. The deposit containing 6.6 at.% W obtained at −0.1 V (Fig. 2–4b) is composed of grains with leaf-like morphology. The deposits containing 9.1–11.8 at.% W electrodeposited at −0.2–−0.5 V (Figs. 2–4c–f) are composed of rounded and needle-like nodules with diameters less than 3 μm and no crystallographic facets. As shown by the arrow in the insets of Fig. 2–4d and 2–4e, some of the rounded nodules appear to have grown into those with needle-like shapes. The deposits at −0.2–−0.5 V (Figs. 2–4c–f) form dense films with no cracks.

The XRD patterns of the deposits are shown in Fig. 2–5. The deposit obtained at +0.3 V presents no clear diffractions, except for those from the Cu substrate. All the deposits containing > 64 at.% W obtained at potentials more positive than 0 V present no clear diffractions. This suggests that these deposits are amorphous, or not thick enough to cause detectable diffractions. In contrast, clear signals are detected from the deposits with up to 12 at.% W obtained at potentials more negative than 0 V. The deposit with 6.6 at.% W obtained at −0.1 V show a characteristic diffraction pattern for fcc Al. The

deposits with 9.1–11.4 at.% W obtained at −0.2, −0.4, and −0.5 V also show the pattern for fcc Al, but the peak intensities are significantly smaller. In addition, a broad halo appears at around 2θ = 42°. The deposit with 11.8 at.% W obtained at −0.3 V shows only a broad halo.

An enlarged view of the Al(111) diffraction peaks is shown in the right-hand graph in Fig. 2–5. The Al(111) peak positions of the deposits with 6.6–11.4 at.% W shift to higher angles compared to that of the electrodeposited Al metal. These peak shifts indicate the formation of a solid solution of fcc Al containing W atoms, which have a smaller radius than the Al atoms. According to Al–W binary phase diagrams, the maximum solubility of W in fcc Al is 0.022 at.% at 640°C [6]. Therefore, a super-saturated Al–W solid solution constitutes the deposits with 6.6–11.4 at.% W. The deposit with 6.6 at.% W, which shows clear fcc Al diffractions, is mainly composed of a solid solution. In contrast, the deposits with 9.1–11.4 at.% W show weaker diffractions for fcc Al and a broad halo around 2θ = 42°, indicating that these deposits contain a small amount of the solid solution phase, and a large amount of an amorphous phase. The deposit with 11.8 at.% W shows only a halo around 2θ = 42°, indicating that this deposit is composed of an amorphous phase only. The presence of amorphous phase in the deposits with 9–12 at.% W agrees with the fact that the deposits are composed of nodules with no crystallographic facets (Figs. 2–4c–f). The formation of the super-saturated solid solution and the amorphous phase was also observed in the electrodeposition of Al–W alloy in the bath containing $K_3W_2Cl_9$, although the amorphous phase appeared at a lower W content (5 at.%) [32].

The XRD analysis was not able to reveal the phase of the deposits with a high W content obtained at potentials more positive than 0 V, because the diffraction signals were too small. In these cases, the deposits were examined with XPS. Fig. 2–6 shows the W 4 f and Al 2s spectra of the deposit obtained at +0.3 V (92 at.% W) before and after Ar^+ etching. The peak seen at 122.5 eV in Fig. 2–6b is the Cu 3s peak derived from the substrate [39]. Before Ar^+ etching, the W 4f spectra (Fig. 2–6a) shows peaks ascribable to W_2O_5 and WO_3. The Al 2s spectra (Fig. 2–6b) show peaks for Al_2O_3. After Ar^+ etching for 30 s, the peak intensity for the W oxides in the W 4f spectra decreases, and peaks ascribed to W metal appear. In the Al 2s spectra, the Al_2O_3 peak is present as well as before etching. After etching for

870 s, the peaks for the W metal become more intense relative to those of the W oxides, while the Al signal disappears.

The peak shifts in the W 4f spectra upon etching may imply that W in the metallic state is electrodeposited but the surface of the deposit is oxidized in air after electrodeposition. However, the electrodeposition of W metal cannot be concluded, because long-time Ar^+ etching during XPS measurement can reduce W oxides to a lower oxidation state, and eventually to W metal [40]. Although the oxidation state of W is ambiguous, Al clearly exists only in the oxide state, because Al 2s spectra do not show any peak shift after etching. The Al 2s signal disappears after the 870-s etching, while the W 4f signal is still clearly observed. This means that Al exists only near the deposited surface. Therefore, the Al_2O_3 detected by XPS is probably derived from residues of the bath components on the deposited surface. The large scattering of the W content determined by EDX (Fig. 2–3) is attributable to variations in the amount of residue from the bath components.

The examination of the deposits described above shows that Al–W alloy films containing up to 12 at.% W are electrodeposited at potentials <0 V, while deposits with a high content of W, whose oxidation state is unclear, are obtained at potentials >0 V.

Partial current density and current efficiency

The amount of W in deposits obtained at each potential was measured with ICP-AES to calculate the partial current density for W deposition (J_W). The partial current density for Al deposition (J_{Al}) was also calculated from J_W and the W content of the deposits. The steady-state total current density (J_{total}), J_W, and J_{Al} are plotted against the deposition potential in Fig. 2–7. At potentials more positive than 0 V, J_W is calculated to be as low as 5.0×10^{-3} mA cm^{-2}, assuming that all the W atoms in the deposits are in the metallic state. As revealed by XPS, Al is not electrodeposited at potentials >0 V, and therefore J_{Al} is negligible. From the comparison of J_W with J_{total}, the current efficiency for W deposition at potentials >0 V is estimated to be less than 2%. The current loss is most probably due to the reduction of protonic impurities in the electrolytic bath. The presence of protonic impurities was

confirmed by a cathodic wave at around +1.0 V in cyclic voltammetry using a Pt electrode [41]. The deposition rate at potentials >0 V is so low that the impurity reduction current accounts for a large part of J_{total}, leading to the low current efficiency. Since the deposit is fragile as evidenced by the SEM image (Fig. 2–4a), exfoliation of the deposits from the electrode during electrodeposition could also be responsible for the low current efficiency. In contrast, at potentials <0 V, J_W as well as J_{Al} increase at more negative potentials and J_W reaches 1.2 mA cm^{-2} at −0.3 V. From the comparison of $J_W + J_{Al}$ with J_{total}, the current efficiency for Al–W alloy deposition is estimated to be approximately 90%.

The deposition rate is low at potentials >0 V, whereas the rate increases drastically when W is co-deposited with Al at potentials <0 V. This means that at potentials more negative than 0 V, the deposition of W is induced by the deposition of Al. This induced-electrodeposition behavior for W was not observed in the previous study on Al–W electrodeposition using $K_3W_2Cl_9$ as the W ion source. The difference in the deposition behaviors for W arises mainly from the solubility of the W ion source in the ionic liquid. Because the solubility of $K_3W_2Cl_9$ is low, the deposition rate of W is limited by the diffusion of W ions in the bath. In contrast, W_6Cl_{12} dissolves in the ionic liquid at a higher concentration, and therefore the deposition rate of W is increased by Al deposition without being limited by diffusion of the W ions.

Pitting corrosion resistance of Al–W alloy films

As mentioned above, potentiostatic electrodeposition at <0 V yields dense and adherent Al–W alloy films containing up to 12 at.% W. The corrosion resistance of the Al–W alloy films was examined by measuring the pitting potential in 3.5 wt.% aqueous NaCl solution through potentiodynamic polarization. Figure 2–8 shows polarization curves for an Al–W alloy film (10.5 at.% W) and an Al plate. In the polarization curve for the pure Al plate, the anodic current density presents a steep rise at −0.48 V, which is close to the rest potential (−0.53 V vs. SHE). Conversely, in the polarization curve for the Al–W alloy film, the anodic current density presents a steep rise at +0.14 V, which is more positive than the rest potential (−0.34 V). The steep rise in the anodic current density is attributed to

the pitting corrosion on the surface. The Al–W alloy film exhibits a pitting potential that is +0.62 V more positive than that for the pure Al plate.

In a previous report, an Al–2.3 at.% W alloy film electrodeposited from an EMIC–$AlCl_3$–$K_3W_2Cl_9$ bath displayed a pitting potential that was +0.3 V more positive than that for pure Al [32]. As reported in a series of studies on sputtered Al–W alloys, Al–W alloys exhibit higher pitting potentials with increasing W content [4,5,7,9–11]. However, the Al–W alloys electrodeposited from the $K_3W_2Cl_9$ bath had powdery morphologies and were easily exfoliated from the substrate when the W content was > 5 at.%, making it difficult to carry out polarization experiments. In contrast, the Al–W alloys electrodeposited from the W_6Cl_{12} bath in the present study are dense and adherent, even when the W content is > 10 at.%. As a result, the alloy film obtained from the W_6Cl_{12} bath shows a higher pitting potential than those from the $K_3W_2Cl_9$ bath.

2.4. Conclusion

W_6Cl_{12} dissolves in an EMIC–2$AlCl_3$ ionic liquid at concentrations as high as 49 mM at 80 °C. Potentiostatic electrodeposition at various potentials in the bath containing 49 mM W_6Cl_{12} revealed that Al–W alloy films containing up to 12 at.% W were electrodeposited at potentials more negative than 0 V vs. Al/Al(III). The deposition current density at > 0 V was lower than 0.3 mA cm^{-2}, while that for Al–W alloy films was higher and reached 38 mA cm^{-2} at −0.5 V. The deposition of W was induced by the deposition of Al at potentials more negative than 0 V. The Al–W alloy films were composed of a super-saturated solid solution at lower W content, and they comprised an amorphous phase in the W content range of 9–12 at.%. The Al–W alloy films comprising an amorphous phase exhibited a high pitting corrosion resistance.

References

[1] J. Zhang, C. Yan, F. Wang, Electrodeposition of Al-Mn alloy on AZ31B magnesium alloy in molten salts, Appl. Surf. Sci. 255 (2009) 4926–4932. https://doi.org/10.1016/j.apsusc.2008.12.039.

[2] T. Tokunaga, K. Sotomoto, M. Ohno, K. Matsuura, Coating on magnesium alloy with super duralumin by hot extrusion and evaluation of its surface properties, Mater. Trans. 59 (2018) 432–436. https://doi.org/10.2320/jinstmet.J2017019.

[3] T. Tsuda, G.R. Stafford, C.L. Hussey, Review—Electrochemical Surface Finishing and Energy Storage Technology with Room-Temperature Haloaluminate Ionic Liquids and Mixtures, J. Electrochem. Soc. 164 (2017) H5007–H5017. https://doi.org/10.1149/2.0021708jes.

[4] B.A. Shaw, T.L. Fritz, G.D. Davis, W.C. Moshier, The Influence of Tungsten on the Pitting of Aluminum Films, J. Electrochem. Soc. 137 (1990) 1317–1318. https://doi.org/10.1149/1.2086658.

[5] B.A. Shaw, G.D. Davis, T.L. Fritz, B.J. Rees, W.C. Moshier, The Influence of Tungsten Alloying Additions on the Passivity of Aluminum, J. Electrochem. Soc. 138 (1991) 3288–3295. https://doi.org/10.1149/1.2085404.

[6] S.V.N. Naidu, P.R. Rao, eds., Phase Diagrams of Binary Tungsten Alloys, Indian Institute of metals, Calcutta, 1991.

[7] G.D. Davis, B.A. Shaw, B.J. Rees, M. Ferry, Mechanisms of passivity of nonequilibrium Al-W alloys, J. Electrochem. Soc. 140 (1993) 951–959. https://doi.org/10.1149/1.2056234.

[8] N. Radić, A. Tonejc, M. Milun, P. Pervan, J. Ivkov, M. Stubičar, Preparation and structure of AlW thin films, Thin Solid Films. 317 (1998) 96–99. https://doi.org/10.1016/S0040-6090(97)00508-7.

[9] M. Metikos-Hukovic, N. Radic, Z. Grubac, A. Tonejc, The corrosion behavior of sputter-deposited aluminum-tungsten alloys, Electrochim. Acta. 47 (2002) 2387–2397.

[10] D. Kek Merl, P. Panjan, J. Kovač, Corrosion and surface study of sputtered Al-W coatings with a range of tungsten contents, Corros. Sci. 69 (2013) 359–368. https://doi.org/10.1016/j.corsci.2013.01.002.

[11] D. Kek Merl, P. Panjan, I. Milošev, Effect of tungsten content on properties of PVD sputtered Al–W_x alloys, Surf. Eng. 29 (2013) 281–286. https://doi.org/10.1179/1743294412Y.0000000086.

[12] C.M. Rangel, M.A. Travassos, J. Chevallier, Microstructural modifications of aluminium surfaces ion implanted with W and its effect on corrosion and passivation, Surf. Coatings Technol. 89 (1997) 101–107. https://doi.org/10.1016/S0257-8972(96)02907-6.

[13] R.S. Rajamure, H.D. Vora, S.G. Srinivasan, N.B. Dahotre, Laser alloyed Al-W coatings on aluminum for enhanced corrosion resistance, Appl. Surf. Sci. 328 (2015) 205–214. https://doi.org/10.1016/j.apsusc.2014.12.037.

[14] T. Tsuda, C.L. Hussey, G.R. Stafford, Progress in Surface Finishing with Lewis Acidic Room-Temperature Chloroaluminate Ionic Liquids, ECS Trans. 3 (2007) 217–231. https://doi.org/10.1149/1.2798664.

[15] T. Tsuda, Y. Ikeda, T. Arimura, A. Imanishi, S. Kuwabata, C.L. Hussey, G.R. Stafford, Al-W Alloy Deposition from Lewis Acidic Room-Temperature Chloroaluminate Ionic Liquid, ECS Trans. 50 (2013) 239–250. https://doi.org/10.1149/05011.0239ecst.

[16] K. Sato, H. Matsushima, M. Ueda, Electrodeposition of Al-W Alloys in $AlCl_3$-NaCl-KCl Molten Salt Containing WCl_4, ECS Trans. 75 (2016) 305–312. https://doi.org/10.1149/07515.0305ecst.

[17] S. Higashino, M. Miyake, H. Fujii, A. Takahashi, T. Hirato, Electrodeposition of Al-W Alloy Films in a 1-Ethyl-3-methyl-imidazolium Chloride-$AlCl_3$ Ionic Liquid Containing W_6Cl_{12}, J. Electrochem. Soc. 164 (2017) D120–D125. https://doi.org/10.1149/2.0131704jes.

[18] S. Higashino, M. Miyake, A. Takahashi, Y. Matamura, H. Fujii, R. Kasada, T. Hirato, Evaluation of the hardness and Young's modulus of electrodeposited Al–W alloy films by

nano-indentation, Surf. Coatings Technol. 325 (2017) 346–351. https://doi.org/10.1016/j.surfcoat.2017.06.064.

[19] S. Higashino, M. Miyake, H. Fujii, A. Takahashi, R. Kasada, T. Hirato, Electrodeposition of Aluminum-T-ungsten Alloy Films Using EMIC–$AlCl_3$–W_6Cl_{12} Ionic Liquids of Different Compositions, Mater. Trans. 59 (2018) 944–949. https://doi.org/10.2320/matertrans.M2018051.

[20] W.R. Pitner, C.L. Hussey, G.R. Stafford, Electrodeposition of Nickel-Aluminum Alloys from the Aluminum Chloride-1-methyl-3-ethylimidazolium Chloride Room Temperature Molten Salt, J. Electrochem. Soc. 143 (1996) 130. https://doi.org/10.1149/1.1836397.

[21] T. Tsuda, C.L. Hussey, G.R. Stafford, J.E. Bonevich, Electrochemistry of Titanium and the Electrodeposition of Al-Ti Alloys in the Lewis Acidic Aluminum Chloride–1-Ethyl-3-methylimidazolium Chloride Melt, J. Electrochem. Soc. 150 (2003) C234–C243. https://doi.org/10.1149/1.1554915.

[22] T. Tsuda, C.L. Hussey, G.R. Stafford, O. Kongstein, Electrodeposition of Al-Zr Alloys from Lewis Acidic Aluminum Chloride-1-Ethyl-3-methylimidazolium Chloride Melt, J. Electrochem. Soc. 151 (2004) C447. https://doi.org/10.1149/1.1753231.

[23] T. Tsuda, C.L. Hussey, G.R. Stafford, Electrodeposition of Al-Mo Alloys from Lewis Acidic Aluminum Chloride-1-Ethyl-3-methylimidazolium Chloride Melt, J. Electrochem. Soc. 151 (2004) C379–C384. https://doi.org/10.1149/1.1753231.

[24] S. Ruan, C.A. Schuh, Electrodeposited Al-Mn alloys with microcrystalline, nanocrystalline, amorphous and nano-quasicrystalline structures, Acta Mater. 57 (2009) 3810–3822. https://doi.org/10.1016/j.actamat.2009.04.030.

[25] T. Tsuda, S. Kuwabata, G.R. Stafford, C.L. Hussey, Electrodeposition of aluminum-hafnium alloy from the Lewis acidic aluminum chloride-1-ethyl-3-methylimidazolium chloride molten salt, J. Solid State Electrochem. 17 (2013) 409–417. https://doi.org/10.1007/s10008-012-1933-y.

[26] F. Endres, D. MacFarlane, A. Abbott, eds., Electrodeposition from ionic liquids, Wiley, Weinheim, 2008.

[27] G.R. Stafford, C.L. Hussey, Electrodeposition of Transition Metal-Aluminum Alloys from Chloroaluminate Molten Salts, in: R.C. Alkire, D.M. Kolb (Eds.), Adv. Electrochem. Sci. Eng. Vol. 7, Willey, Weinheim, 2002: pp. 275–347.

[28] T. Tsuda, Application of Room-Temperature Ionic Liquid to Electrolyte for Alloy Electrodeposition, J. Surf. Finish. Soc. Japan. 60 (2009) 497–501. https://doi.org/10.4139/sfj.60.497.

[29] S. Shiomi, M. Miyake, T. Hirato, Electrodeposition of aluminum at near-ambient temperature, J. Japan Inst. Light Met. 63 (2013) 234–242.

[30] M. Ueda, Overview over studies of electrodeposition of Al or Al alloys from low temperature chloroaluminate molten salts, J. Solid State Electrochem. 21 (2017) 641–647. https://doi.org/10.1007/s10008-016-3428-8.

[31] Y. Gu, J. Liu, S. Qu, Y. Deng, X. Han, W. Hu, Electrodeposition of alloys and compounds from high-temperature molten salts, J. Alloys Compd. 690 (2017) 228–238. https://doi.org/10.1016/j.jallcom.2016.08.104.

[32] T. Tsuda, Y. Ikeda, T. Arimura, M. Hirogaki, A. Imanishi, S. Kuwabata, G.R. Stafford, C.L. Hussey, Electrodeposition of Al-W Alloys in the Lewis Acidic Aluminum Chloride-1-Ethyl-3-Methylimidazolium Chloride Ionic Liquid, J. Electrochem. Soc. 161 (2014) D405–D412. https://doi.org/10.1149/06404.0563ecst.

[33] V. Kolesnichenko, D.C. Swenson, L. Messerle, Facile Reduction of Tungsten Halides with Nonconventional, Mild Reductants. I. Tungsten Tetrachloride: Several Convenient Solid-State Syntheses, a Solution Synthesis of Highly Reactive (WCl4)x, and the Molecular Structure of Polymeric Tungsten Tetrachlori, Inorg. Chem. 37 (1998) 3257–3262.

[34] M. Strobele, T. Justel, H. Bettentrup, H.-J. Meyer, The synthesis and Luminescence of W6Cl12 and Mo6Cl12 revisited, Zeitschrift Fur Anorg. Und Allg. Chemie. 635 (2009) 822–

827. https://doi.org/10.1002/zaac.200801383.

[35] S. Kamiguchi, T. Chihara, Catalytic dehydration of alcohol to olefin and ether by halide clusters of Nb, Mo, Ta and W posessing an octahedral metal core, Catal. Letters. 85 (2003) 97–100. https://doi.org/10.1016/S1381-1169(02)00546-0.

[36] G. Wilkinson, R.D. Gillard, J.A. McCleverty, eds., Comprehensive Coordination Chemistry: The Synthesis, Reactions, Properties & Applications of Coordination Compounds., Pergamon Press, Oxford, 1987.

[37] W. C. Dorman and R. E. McCarley, Chemistry of the Polynuclear Metal Halides . XII . Preparation of Molybdenum and Tungsten M6X84 + Clusters by Reduction of Higher Halides in Molten Sodium Halide- Aluminum Halide Mixtures, Inorg. Chem. 13 (1974) 491.

[38] P.A. Barnard, I. Sun, C.L. Hussey, Molybdenum(II) Chloride in the Aluminum Chloride-1-Methyl-3-ethylimidazolium Chloride Molten Salt. Electrochemical and Spectroscopic Characterization of the [(Mo6C18)Cl6]2- Ion in Neutral and Basic Melts, Inorg. Chem. 29 (1990) 3670–3674.

[39] A.N. Mansour, Copper Mg Kα XPS Spectra from the Physical Electronics Model 5400 Spectrometer, Surf. Sci. Spectra. 3 (1994) 202. https://doi.org/10.1116/1.1247748.

[40] H.Y. Wong, C.W. Ong, R.W.M. Kwok, K.W. Wong, S.P. Wong, W.Y. Cheung, Effects of ion beam bombardment on electrochromic tungsten oxide films studied by X-ray photoelectron spectroscopy and Rutherford back-scattering, Thin Solid Films. 376 (2000) 131–139. https://doi.org/10.1016/S0040-6090(00)01204-9.

[41] S. Sahami, R.A. Osteryoung, Voltammetric Determination of Water in an Aluminum Chloride-N-n-Butylpyridinium Chloride Ionic Liquid, Anal. Chem. 55 (1983) 1970–1973.

[42] A. Katrib, F. Hemming, P. Wehrer, L. Hilaire, G. Maire, The multi-surface structure and catalytic properties of partially reduced WO3, WO2 and WC + O2 or W + O2 as characterized by XPS, J. Electron Spectros. Relat. Phenomena. 76 (1995) 195–200. https://doi.org/10.1016/0368-2048(95)02451-4.

[43] C. Hinnen, D. Imbert, J.M. Siffre, P. Marcus, An in situ XPS study of sputter-deposited aluminium thin films on graphite, Appl. Surf. Sci. 78 (1994) 219–231. https://doi.org/10.1016/0169-4332(94)90009-4.

[44] B.R. Strohmeier, Characterization of an Activated Alumina Claus Catalyst by XPS, Surf. Sci. Spectra. 3 (1994) 141. https://doi.org/10.1116/1.1247775.

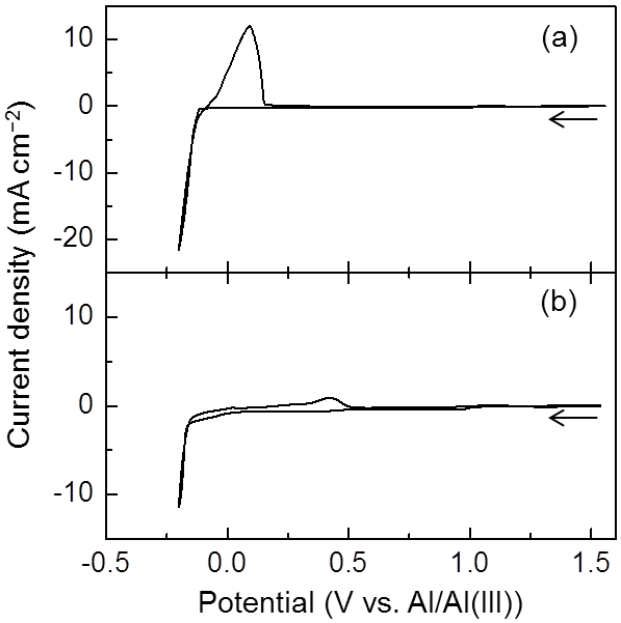

Figure 2–1. Cyclic voltammograms recorded at a Pt electrode in an EMIC–$AlCl_3$ (1:2) bath at 80 °C (a) before and (b) after adding 49 mM W_6Cl_{12}. The scan rate was 10 mV s^{-1}.

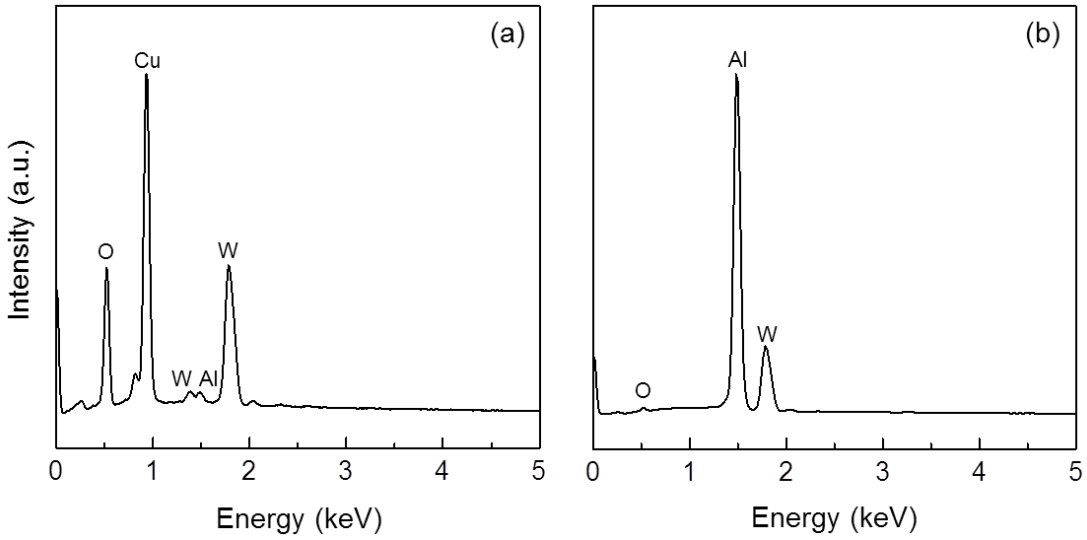

Figure 2–2. Typical EDX spectra of the deposits obtained from an EMIC–$AlCl_3$ bath containing 49 mM W_6Cl_{12}. The applied potentials are: (a) +0.3 V and (b) −0.5 V.

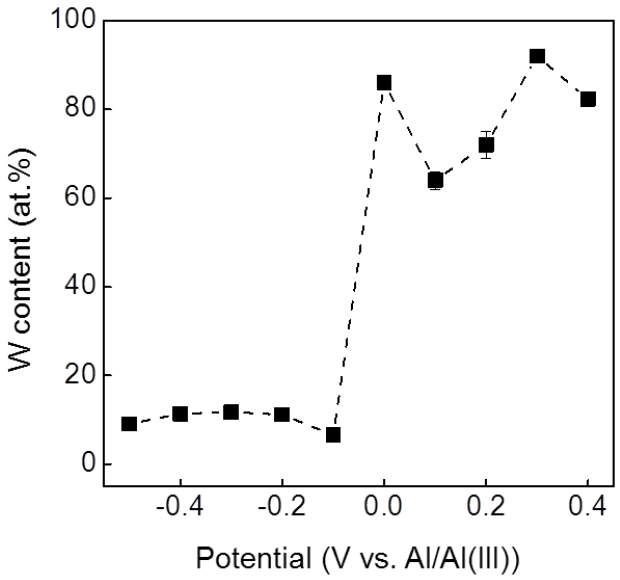

Figure 2–3. W content of the deposits obtained at various applied potentials in an EMIC–$AlCl_3$ bath containing 49 mM W_6Cl_{12}.

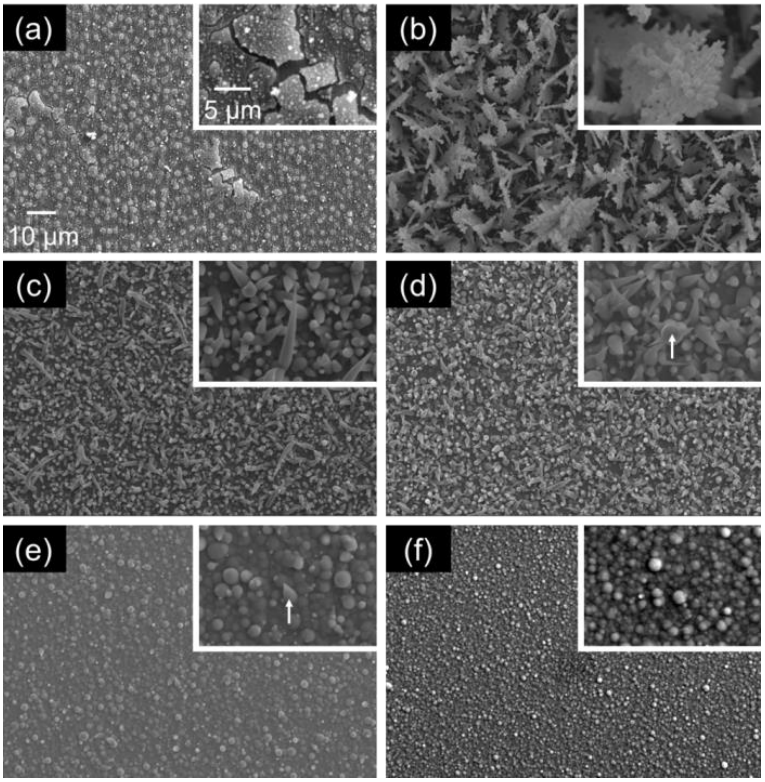

Figure 2–4. Surface SEM images of the deposits obtained in an EMIC–$AlCl_3$ bath containing 49 mM W_6Cl_{12}. The applied potentials and the W contents of the deposits are; (a) +0.1 V, 64 at.%, (b) −0.1 V, 6.6 at.%, (c) −0.2 V, 11.2 at.%, (d) −0.3 V, 11.8 at.%, (e) −0.4 V, 11.4 at.%, (f) −0.5 V, 9.1 at.%.

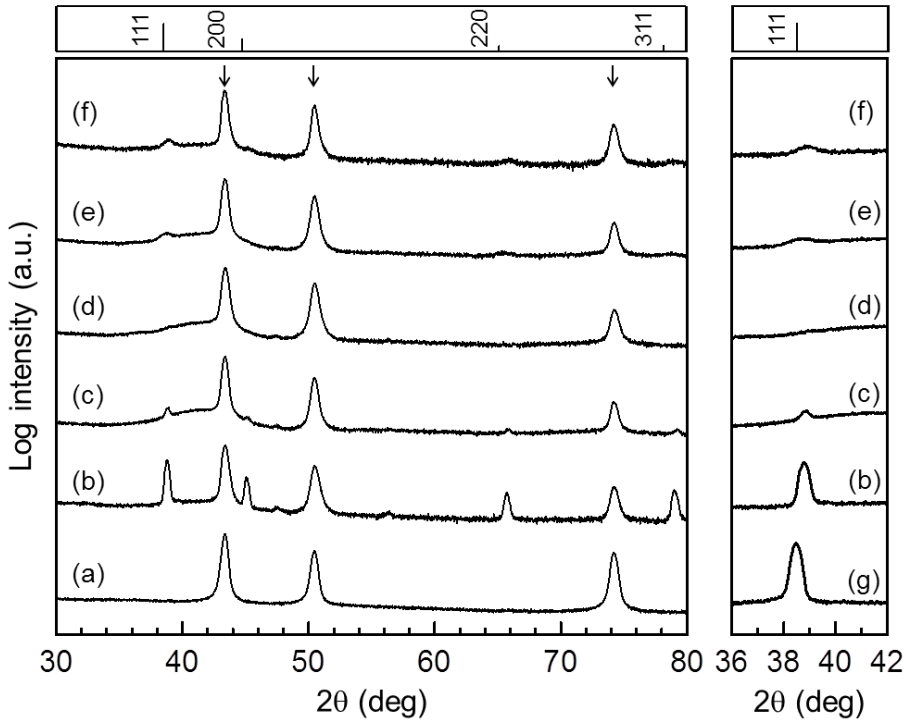

Figure 2–5. (Left) XRD patterns of the deposits obtained in an EMIC–$AlCl_3$ bath containing 49 mM W_6Cl_{12}. The applied potentials and the W contents of the deposits are; (a) +0.3 V, 92 at.%, (b) −0.1 V, 6.6 at.%, (c) −0.2 V, 11.2 at.%, (d) −0.3 V, 11.8 at.%, (e) −0.4 V, 11.4 at.%, (f) −0.5 V, 9.1 at.%. The arrows indicate the diffraction peaks from the Cu substrate. The peak positions for fcc Al (ICDD: 00-004-0787) are shown at the top of the figure. (Right) An enlarged view of the Al(111) diffraction peaks of the deposits and (g) an electrodeposited Al film.

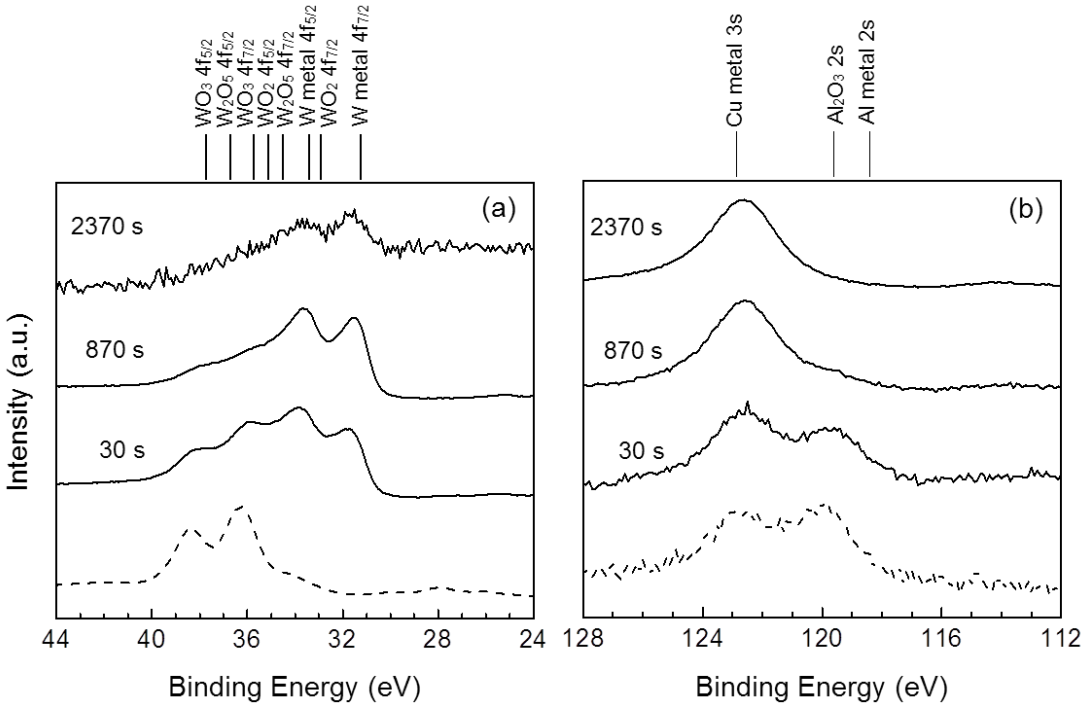

Figure 2–6. The XPS spectra of the deposit with 92 at.% W obtained at +0.3 V before (dashed line) and after (solid line) Ar^+ etching. The spectra are (a) W 4f, and (b) Al 2s. The etching times were 30, 870, and 2370 s. The binding energy of W metal, WO_2, W_2O_5, WO_3 [42], Al metal [43], and Al_2O_3 [44] are denoted at the top of the figure.

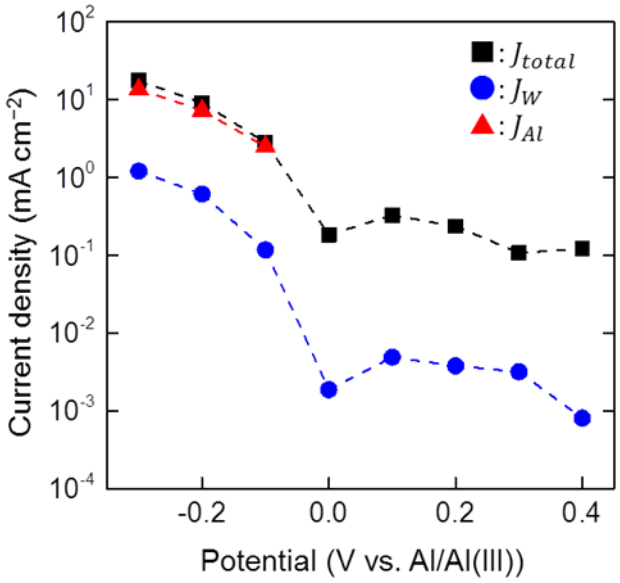

Figure 2–7. Steady-state total current density (J_{tatol}) and partial current densities for W and Al deposition (J_W and J_{Al}) during electrodeposition in an EMIC–$AlCl_3$ bath containing 49 mM W_6Cl_{12}.

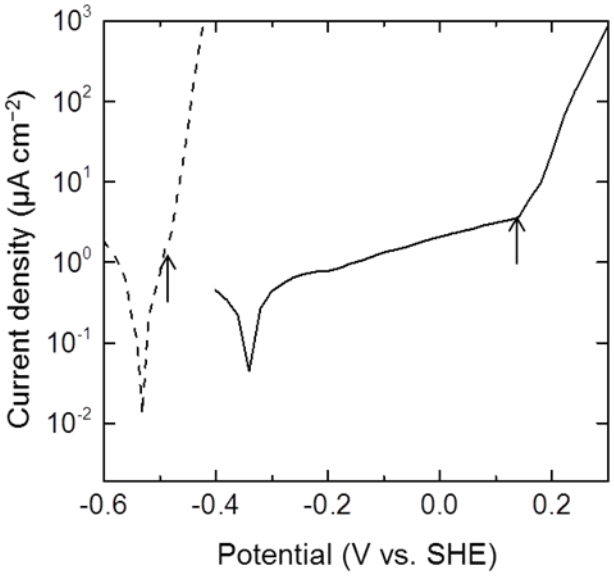

Figure 2–8. Polarization curves for the Al–W alloy film containing 10.5 at.% W (solid line) and an Al plate (dashed line) in 3.5 wt.% aqueous NaCl solution. The scan rate was 0.5 mV s^{-1}. The pitting potential for each curve is indicated by the arrow.

Chapter 3

Evaluations of hardness and Young's modulus of electrodeposited Al–W alloy films using nanoindentation

3.1. Introduction

In the previous chapter, dense Al–W alloy films with a W content of up to 12 at% were electrodeposited from an EMIC–$AlCl_3$ ionic liquid containing W_6Cl_{12} [1]. These Al–W alloy films showed a high resistance to chloride-induced pitting corrosion. When Al–W alloy films are employed as corrosion-protective coatings, the mechanical strength of the films is also an important factor to consider. In particular, if the film is applied onto a reactive material such as Mg alloys and steels, mechanical damage penetrating through the film can accelerate the corrosion of the base material due to the formation of a galvanic couple [2]. To avoid such corrosion, the film needs to have a high mechanical strength. However, the data on the mechanical properties of Al–W alloy films are limited.

A few reports on the Vickers hardness of sputtered Al–W alloy films are available in the literature [3,4]. According to the reports [3,4], the hardness increases from 1.7 GPa for an Al–0.6 at% W alloy to 20 GPa for an Al–50 at% W alloy. No data for electrodeposited films has been published. The mechanical properties of the alloy films should depend on their composition, constituting phase, grain size, and process conditions. In this study, films with different W contents and different phases were prepared by electrodeposition using EMIC–$AlCl_3$ ionic liquids at several W_6Cl_{12} concentrations. The hardness and Young's modulus of the resulting films were measured by nano-indentation. The effects of W content, phase, and grain size on the hardness and Young's modulus are discussed.

3.2. Methods

The preparation of EMIC–$AlCl_3$–W_6Cl_{12} bath and experimental setup of electrochemical measurement were described in chapter 2. Galvanostatic electrodeposition was performed on a polished Ni plate. The purpose of using Ni plates instead of Cu plates as in chapter 2 is to avoid the deformation of the substrate during the nano-indentation tests. A section of the Ni plate was covered with polytetrafluoroethylene tape so to expose a defined area (5 mm × 5 mm). An Al plate was used as the counter electrode.

Film characterization using SEM, EDX and XRD was described in chapter 2. The hardness and Young's modulus of the Al–W alloy films were determined by nano-indentation tests using a nano-indenter (G200, Agilent Technologies) with a diamond Berkovich tip. The surfaces of the electrodeposited 10-μm thick pure Al and Al–W alloy films were mirror polished prior to the indentation tests to minimize the errors caused by surface roughness. Indentation data were collected with the continuous stiffness measurement technique [5–8] with a vibration frequency of 45 Hz. In each indentation, the hardness and Young's modulus values were obtained at a depth of 200 nm, where the influence of the Ni substrate was not influential. The indentation size effect [9] and the influence of the residual stress caused by polishing were also negligible at this depth. Each value reported for the hardness and Young' s modulus are averages of the values taken at 12 indentation points, which were separated by more than 50 μm in all directions. In the evaluation of the Young's modulus, the Poisson's ratio of the Al–W alloy films was assumed to be 0.3, which is a typical value for metallic materials [10]. The error of the Young's modulus caused by varying Poisson's ratio between 0.2 and 0.4 was within 10% [11]. The Young's modulus of the Al film was calculated using the Poisson's ratio reported for Al (0.34) [12,13].

3.3. Results and discussion

3.1. Electrodeposition and composition of the deposits

To obtain Al and Al–W alloy films with different W content, galvanostatic electrodeposition was

carried out at 20 mA cm^{-2} in EMIC–$AlCl_3$ baths containing 0–49 mM W_6Cl_{12}. The amount of charge was set at 30 C cm^{-2}, which corresponds to the value required to electrodeposit a 10.4-μm-thick pure Al film or a 14.8-μm-thick pure W film. Every electrodeposition cycle in the 0–49 mM W_6Cl_{12} baths yielded a whitish-gray film on the Ni substrate. Fig. 3–1 shows the typical EDX spectra of the deposits, showing that the deposit was composed only from Al and W. No other element was detected, except for a slight amount of O owing to surface oxidation. The W content of the deposits determined by EDX is plotted against the W_6Cl_{12} concentration in Fig. 3–2, where only the Al and W presence was considered. The W content increases with increasing W_6Cl_{12} concentration, reaching 12.4 at% when the W_6Cl_{12} concentration is 24 mM. When the W_6Cl_{12} concentration is higher than 24 mM, the W content is almost constant between 12 and 13 at%. The behavior of the W content with respect to the W_6Cl_{12} concentration is like the Langmuir type adsorption isotherm, suggesting that the electrodeposition of W_6Cl_{12} to W(0) occurs via adsorption of W(II) ions on the cathode surface. It can be inferred that the reduction process of the adsorbed W(II) ions to W(0) is slow, and therefore, the number of the W(II) ions adsorbed on the cathode surface is nearly in equilibrium with the W_6Cl_{12} concentration during the electrodeposition. Saturation of W content of the electrodeposited alloy would be due to the saturated adsorption site of W(II) ions on the cathode surface at the bulk W_6Cl_{12} concentration of > 24 mM.

3.2. Morphology

Surface and cross-sectional SEM images of the Al film and the Al–W alloy films are shown in Fig. 3–3. The 0–9.8 at% W films obtained from the 0–20 mM W_6Cl_{12} baths are composed of angular grains. The grain size of the 0–7.2 at% W films increases with the increase of the W content from ~3 μm for the 0 at% W film to ~10 μm for the 7.2 at% W film, although smaller grains (< 3 μm) are also present in the 7.2 at% W film. The 9.8 at% W film is composed of grains smaller than those observed in the 7.2 at% film. The films with 12–13 at% W obtained from the baths containing more than 24 mM W_6Cl_{12} (Figs. 3–3f and g) are composed of rounded nodules with diameters less than 10 μm. Grains

with crystallographic facets are not observed in these films. The cross-sectional image of the 12.4 at% W film obtained from the 49 mM W_6Cl_{12} bath shows that the film is dense and has good adhesion to the substrate. The average thickness is ~11 μm, which agrees with the value estimated from the electric charge.

3.3. Phase identification

The XRD patterns of the Al and Al–W alloy films are shown in Fig. 3–4. The films with 0–7.2 at% W show characteristic diffraction patterns for fcc Al. The 9.8 and 12.4 at% W films from the 20 and 24 mM W_6Cl_{12} baths show weak fcc Al peaks and a halo around $2\theta = 42°$. The 12–13 at% W films from the baths containing more than 32 mM W_6Cl_{12} show only the halo around $2\theta = 42°$.

An enlarged view of the Al(111) diffraction peaks is shown in the right-hand graph in Fig. 3–4. The Al(111) peak position shifts to a higher angle with the increase of the W content. These peak shifts indicate the formation of a substitutional solid solution of fcc Al containing W atoms, which have a smaller radius than the Al atoms. According to the Al–W binary phase diagram, the maximum solubility of W in fcc Al phase is 0.022 at% at 640°C [14]. Therefore, the 2.0–12.4 at% W films from the 2–24 mM W_6Cl_{12} baths comprise a super-saturated solid solution of fcc Al phase. The 2.0–7.2 at% W films show only the distinctive diffraction pattern for fcc Al, indicating that these films are mainly composed of the fcc solid solution. The 9.8 and 12.4 at% W films from the 20 and 24 mM W_6Cl_{12} baths show the diffraction pattern for fcc Al and a halo around $2\theta = 42°$, indicating that the fcc Al solid-solution phase coexists with an amorphous phase. The halo is more evident in the 12.4 at% W film than in the 9.8 at% W film, and therefore the volume fraction of the amorphous phase is higher in the 12.4 at% W film than in the 9.8 at% W film. The 12–13 at% W films from the baths containing more than 32 mM W_6Cl_{12}, showing only the broad halo, should be composed of a single amorphous phase.

The lattice parameters of the fcc Al phase in the 0–12.4 at% W films were calculated from the peak positions of Al(111) based on Bragg's law. In this calculation, the Ni(111) peak position of the Ni substrate was employed as the internal standard. The aluminum lattice parameter (a_{Al}) is plotted

against W content in Fig. 3–5. The value of a_{Al} decreases linearly with increasing W content at 0–7.2 at% W. When the W contents are 9.8 and 12.4 at% W, however, the value of a_{Al} is greater than that expected from the linear relationship seen for 0–7.2 at% W (solid line in Fig. 3–5). This indicates that some of the W atoms in the 9.8 and 12.4 at% W films are not involved in the fcc Al phase and form the amorphous Al–W alloy phase.

As shown in Figs. 3–4f and g, even though the W contents are almost the same at around 12–13 at%, the film from the 24 mM W_6Cl_{12} bath is composed of fcc and amorphous phases, whereas those from the higher W_6Cl_{12} concentration baths are composed of a single amorphous phase. This fact indicates that, besides the W content, the W_6Cl_{12} concentration affects the formation of the amorphous phase. Similar observations were reported for several alloys electrodeposited from aqueous solutions [15,16]. According to the explanations given in these reports [15,16], ions adsorbed on the electrode surface prevent the surface diffusion of adatoms and their incorporation into the crystal lattice. Therefore, an amorphous phase tends to be formed in a bath with a higher ion concentration. The formation of the single amorphous phase in higher W_6Cl_{12} concentration baths can be explained by the same mechanism.

The formation of a super-saturated solid solution and the transition to the amorphous phase at a higher W content were also observed in previous studies [1,17,18]. The same trend was also been reported for electrodeposited Al–Mn alloy films [19].

3.4. Hardness and Young's modulus

The hardness (*H*) and Young's modulus (*E*) of the electrodeposited Al and Al–W alloy films were determined by nano-indentation. In Fig. 3–6a, the *H* values of these films are plotted with solid symbols against the W content. The *H* value increases with increasing W content up to 9.8 at% but decreases with a further increase in the W content to 12.4 at%. This trend is described in more detail in relation to the phase. In films comprising the fcc single phase (0–7.2 at% W), the *H* value monotonically increases with increasing W content. Further increases in the *H* value are observed by the transition from the fcc single phase to the fcc and amorphous phases. However, an increase in the

W content in the two-phase region (9.8–12.4 at% W) decreases the *H* value. The *H* value of the single amorphous film is almost the same within the error as that of the two-phase film with the same W content (12.4 at%).

As shown in Fig. 3–6a, a comparison with the data reported for electrodeposited Al–Mn alloy films reveals that the *H* values at the same solute (W or Mn) content and the behavior of the *H* values depending on the phase are almost the same in the Al–W and Al–Mn alloy films. This fact suggests that the strengthening mechanisms are basically the same in both cases. In the 0–7.2 at% W crystalline films, the increase in *H* value can be attributed to the effects of solution strengthening. Although grain refinement (the Hall–Petch effect) also accounts for the increase in *H* values in the electrodeposited Al–Mn films, it is ruled out in the present case because a decrease in the grain size with increasing W content is not observed in 0–7.2 at% W films by SEM (Figs. 3–3a–d) and XRD; the full width at half maximum (FWHM) of the Al(111) XRD peak for these films is almost constant regardless of the W content (the right-hand graph in Fig. 3–4). According to the report on electrodeposited Al–Mn alloy films [19], the strengthening of the two-phase films is attributed to their microstructure, where fine crystal grains are dispersed in an amorphous matrix, and explained in the manner well known for amorphous metals containing nanocrystals [20,21]. It is suggested that the decrease in the *H* value with increasing Mn content in this two-phase region is caused by a decreasing volume fraction of the reinforcing crystalline phase. The same explanation can be applied to the high *H* values of the 9.8 and 12.4 at% W two-phase films. The grain refinement of these films is confirmed by the SEM images (Figs. 3–3e and f) and the fact that the FWHM of the XRD peak is larger for the two-phase films than for the 0–7.2 at% W films (the right-hand graph in Fig. 3–4). The decrease in *H* value with increasing W content from 9.8 to 12.4 at% W is reasonable in terms of the decreasing volume fraction of the crystalline phase, as evidenced by XRD.

The *H* values for the electrodeposited Al–W films are lower by ~2 GPa than the values reported for sputtered Al–W alloy films with similar W contents [4]. The lower values are probably because the grain size of the fcc phase is larger in the electrodeposited films.

Figure 3–6b shows the *E* values of the films. The *E* value of the Al film (78±4 GPa) was slightly higher than the value reported in literature of 70 GPa [12,13], which was determined by the pulsed ultrasonic method, but close to the value (75–80 GPa) determined by nano-indentation by other research groups [22,23]. Radvic et al. demonstrated that the *E* value of an Al alloy determined by nano-indentation is slightly higher than that determined by other techniques such as resonant ultrasound microscopy, impulse excitation, and four-point bending [24]. The higher value by nano-indentation is ascribed to material pile-up around the indenter tip during the indentation test [25].

As is shown in Fig. 3–6b, the trend of the change in the *E* value with W content is similar to that in the *H* value, but the decrease in the *E* value from 9.8 to 12.4 at% W is larger than that in the *H* value.

The increase in *E* value with increasing W content in the 0–7.2 at% W films is attributed to stiffer interatomic bonding caused by solute W atoms. In general, the stiffness of interatomic bonding increases with decreasing interatomic distance [10,26,27]. In the 0–7.2 at% W films, solute W atoms decrease the interatomic distance, as evidenced by the decrease in the value of a_{Al} (Fig. 3–5). The drastic decrease in *E* values at 12.4 at% W is attributed to the amorphous phase. The interatomic distance in amorphous alloys is slightly larger than in their crystalline counterparts, and therefore, in elastic deformation of amorphous alloys, each atom experiences larger displacements that cannot be prescribed by the macroscopic strain, leading to lower *E* values [28,29].

In general, hard materials exhibit a high resistance to mechanical damages. Furthermore, Leyland et al. suggested that materials with a high ratio of hardness to Young's modulus (*H*/*E)* exhibit a high wear resistance [30,31]. The *H*/*E* ratios of the electrodeposited 0–12.4 at% W films are shown in Fig. 3–6c. The *H*/*E* ratio increases with increasing W content, and the 9.8–12.4 at% W films show a relatively high *H*/*E* ratio of 0.03–0.05. These alloy films, which have relatively high *H* values and *H*/*E* ratios, can be expected to have a higher resistance to mechanical damage than Al films.

3.4. Conclusion

The electrodeposited Al–W alloy films were composed of a super-saturated fcc Al solid solution phase when the W content was lower than ~9 at%, and an amorphous phase was formed with higher W contents. The hardness (*H*) and Young's modulus (*E*) of the electrodeposited Al–W alloy films with 0–12.4 at% W were measured by nano-indentation. The *H* value increased with increasing W content up to 9.8 at% but then decreased slightly with a further increase in the W content to 12.4 at%. A similar trend is observed for the change in the *E* value. These changes in *H* and *E* values can be explained by the structural behavior. The 9.8–12.4 at% W films exhibited relatively high *H* values and *H*/*E* ratios, and therefore these films are expected to have a higher resistance to mechanical damage than Al films.

References

[1] S. Higashino, M. Miyake, H. Fujii, A. Takahashi, T. Hirato, Electrodeposition of Al-W Alloy Films in a 1-Ethyl-3-methyl-imidazolium Chloride-$AlCl_3$ Ionic Liquid Containing W_6Cl_{12}, J. Electrochem. Soc. 164 (2017) D120–D125. https://doi.org/10.1149/2.0131704jes.

[2] G. Song, B. Johannesson, S. Hapugoda, D. StJohn, Galvanic corrosion of magnesium alloy AZ91D in contact with an aluminium alloy, steel and zinc, Corros. Sci. 46 (2004) 955–977. https://doi.org/10.1016/S0010-938X(03)00190-2.

[3] M. Stubičar, A. Tonejc, N. Radić, Microhardness characterization of Al-W thin films, Vacuum. 61 (2001) 309–316. https://doi.org/10.1016/S0042-207X(01)00135-X.

[4] D. Kek Merl, P. Panjan, I. Milošev, Effect of tungsten content on properties of PVD sputtered Al–W_x alloys, Surf. Eng. 29 (2013) 281–286. https://doi.org/10.1179/1743294412Y.0000000086.

[5] W.C. Oliver, G.M. Pharr, An improved technique for determining hardness and elastic modulus using load and displacement sensing indentation experiments, J. Mater. Res. 7 (1992) 1564–1583.

[6] W.C. Oliver, G.M. Pharr, Measurement of hardness and elastic modulus by instrumented indentation: Advances in understanding and refinements to methodology, J. Mater. Res. 19 (2004) 3–20. https://doi.org/10.1557/jmr.2004.19.1.3.

[7] X. Li, B. Bhushan, A review of nanoindentation continuous stiffness measurement technique and its applications, Mater. Charact. 48 (2002) 11–36. https://doi.org/10.1016/S1044-5803(02)00192-4.

[8] J. Hay, P. Agee, E. Herbert, Continuous stiffness measurement during instrumented indentation testing, Exp. Tech. 34 (2010) 86–94. https://doi.org/10.1111/j.1747-1567.2010.00618.x.

[9] G.M. Pharr, E.G. Herbert, Y. Gao, The Indentation Size Effect: A Critical Examination of Experimental Observations and Mechanistic Interpretations, Annu. Rev. Mater. Res. 40

(2010) 271–292. https://doi.org/10.1146/annurev-matsci-070909-104456.

[10] T. Rouxel, Elastic properties and short-to medium-range order in glasses, J. Am. Ceram. Soc. 90 (2007) 3019–3039. https://doi.org/10.1111/j.1551-2916.2007.01945.x.

[11] P.K. Zysset, X. Edward Guo, C. Edward Hoffler, K.E. Moore, S.A. Goldstein, Elastic modulus and hardness of cortical and trabecular bone lamellae measured by nanoindentation in the human femur, J. Biomech. 32 (1999) 1005–1012. https://doi.org/10.1016/S0021-9290(99)00111-6.

[12] D. Lazarus, The variation of the Adiabatic Elastic Constants of KCl, NaCl, CuZn, Cu, and Al with Pressure to 10,000 Bars, Phys. Rev. 76 (1949) 545–553. https://doi.org/10.1103/PhysRev.76.545.

[13] G. Simmons, H. Wang, Single Crystal Elastic Constants and Calculated Aggregate Properties: A Handbook, 2nd ed, The M.I.T. Press, Cambridge, MA, 1971.

[14] S.V.N. Naidu, P.R. Rao, eds., Phase Diagrams of Binary Tungsten Alloys, Indian Institute of metals, Calcutta, 1991.

[15] Y. Fukunaka, S. Aikawa, Z. Asaki, Fundamental Study on Electrodeposition of Co and Co-P Films, J. Electrochem. Soc. 141 (1994) 1783–1791. https://doi.org/10.1149/1.2055005.

[16] T. Burchardt, V. Hansen, T. Våland, Microstructure and catalytic activity towards the hydrogen evolution reaction of electrodeposited NiPx alloys, Electrochim. Acta. 46 (2001) 2761–2766. https://doi.org/10.1016/S0013-4686(01)00456-X.

[17] B.A. Shaw, G.D. Davis, T.L. Fritz, B.J. Rees, W.C. Moshier, The Influence of Tungsten Alloying Additions on the Passivity of Aluminum, J. Electrochem. Soc. 138 (1991) 3288–3295. https://doi.org/10.1149/1.2085404.

[18] T. Tsuda, Y. Ikeda, T. Arimura, M. Hirogaki, A. Imanishi, S. Kuwabata, G.R. Stafford, C.L. Hussey, Electrodeposition of Al-W Alloys in the Lewis Acidic Aluminum Chloride-1-Ethyl-3-Methylimidazolium Chloride Ionic Liquid, J. Electrochem. Soc. 161 (2014) D405–D412. https://doi.org/10.1149/06404.0563ecst.

[19] S. Ruan, C.A. Schuh, Electrodeposited Al-Mn alloys with microcrystalline, nanocrystalline, amorphous and nano-quasicrystalline structures, Acta Mater. 57 (2009) 3810–3822. https://doi.org/10.1016/j.actamat.2009.04.030.

[20] Y.-H. Kim, A. Inoue, T. Masumono, Ultrahigh Tensile Strength of Al88Y2Ni9M1 (M=Mn or Fe) Amorphous Alloys Containing Finely Dispersed fcc-Al Particles, Mater. Trans. 31 (1990) 747.

[21] A. Inoue, H. Kimura, Fabrications and mechanical properties of bulk amorphous, nanocrystalline, nanoquasicrystalline alloys in aluminum-based system, J. Light Met. 1 (2001) 31–41. https://doi.org/10.1016/S1471-5317(00)00004-3.

[22] Z. Lee, C. Ophus, L.M. Fischer, N. Nelson-Fitzpatrick, K.L. Westra, S. Evoy, V. Radmilovic, U. Dahmen, D. Mitlin, Metallic NEMS components fabricated from nanocomposite Al-Mo films, Nanotechnology. 17 (2006) 3063–3070. https://doi.org/10.1088/0957-4484/17/12/042.

[23] S. Varam, K. V. Rajulapati, K. Bhanu Sankara Rao, Strain rate sensitivity studies on bulk nanocrystalline aluminium by nanoindentation, J. Alloys Compd. 585 (2014) 795–799. https://doi.org/10.1016/j.jallcom.2013.09.116.

[24] M. Radovic, E. Lara-Curzio, L. Riester, Comparison of different experimental techniques for determination of elastic properties of solids, Mater. Sci. Eng. A. 368 (2004) 56–70. https://doi.org/10.1016/j.msea.2003.09.080.

[25] T.Y. Tsui, G.M. Pharr, Substrate effects on nanoindentation mechanical property measurement of soft films on hard substrates, J. Mater. Res. 14 (1999) 292–301. https://doi.org/10.1557/JMR.1999.0042.

[26] J.G. Wang, B.W. Choi, T.G. Nieh, C.T. Liu, Crystallization and nanoindentation behavior of a bulk Zr–Al–Ti–Cu–Ni amorphous alloy, J. Mater. Res. 15 (2000) 798–807. https://doi.org/10.1557/JMR.2000.0114.

[27] C.C. Yuan, X.K. Xi, On the correlation of Young's modulus and the fracture strength of metallic glasses, J. Appl. Phys. 109 (2011) 033515. https://doi.org/10.1063/1.3544202.

[28] C.A. Schuh, T.C. Hufnagel, U. Ramamurty, Mechanical behavior of amorphous alloys, Acta Mater. 55 (2007) 4067–4109. https://doi.org/10.1016/j.actamat.2007.01.052.

[29] D. Weaire, M.F. Ashby, J. Logan, M.J. Weins, On the use of pair potentials to calculate the properties of amorphous metals, Acta Metall. 19 (1971) 779–788. https://doi.org/10.1016/0001-6160(71)90134-9.

[30] A. Leyland, A. Matthews, On the significance of the H/E ratio in wear control: A nanocomposite coating approach to optimised tribological behaviour, Wear. 246 (2000) 1–11. https://doi.org/10.1016/S0043-1648(00)00488-9.

[31] A. Leyland, A. Matthews, Design criteria for wear-resistant nanostructured and glassy-metal coatings, Surf. Coatings Technol. 177–178 (2004) 317–324. https://doi.org/10.1016/j.surfcoat.2003.09.011.

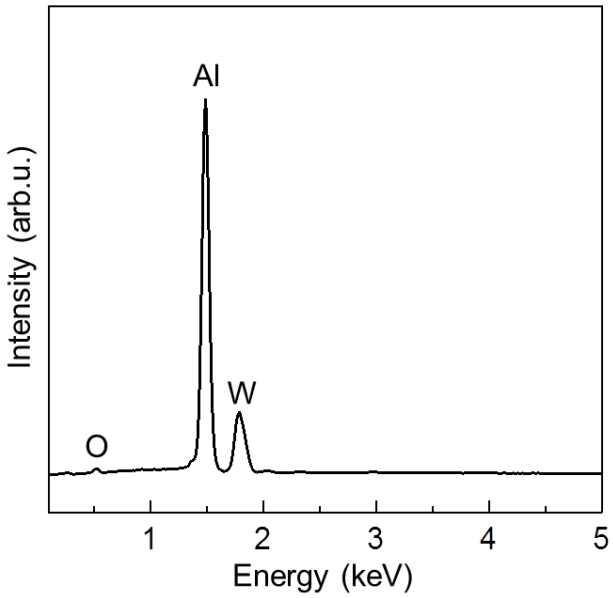

Fig. 3–1 EDX spectrum of the electrodeposited film at 20 mA cm^{-2} in an EMIC–$AlCl_3$ bath containing 49 mM W_6Cl_{12}.

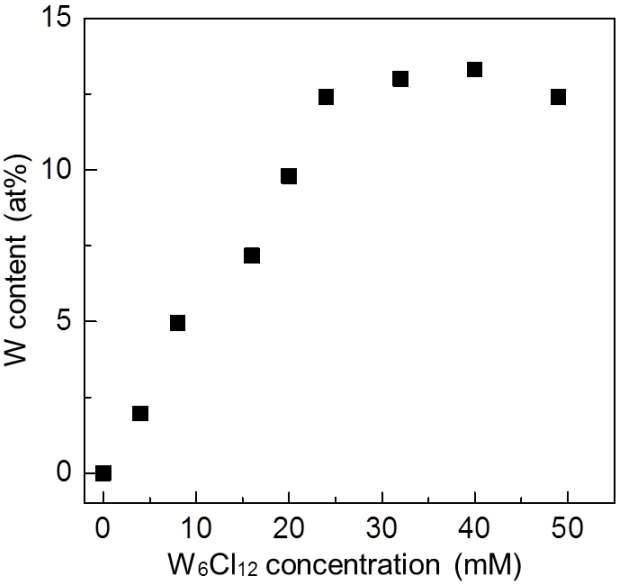

Fig. 3–2 W content of Al–W alloy films electrodeposited at 20 mA cm^{-2} in EMIC–$AlCl_3$ baths containing 0–49 mM W_6Cl_{12}.

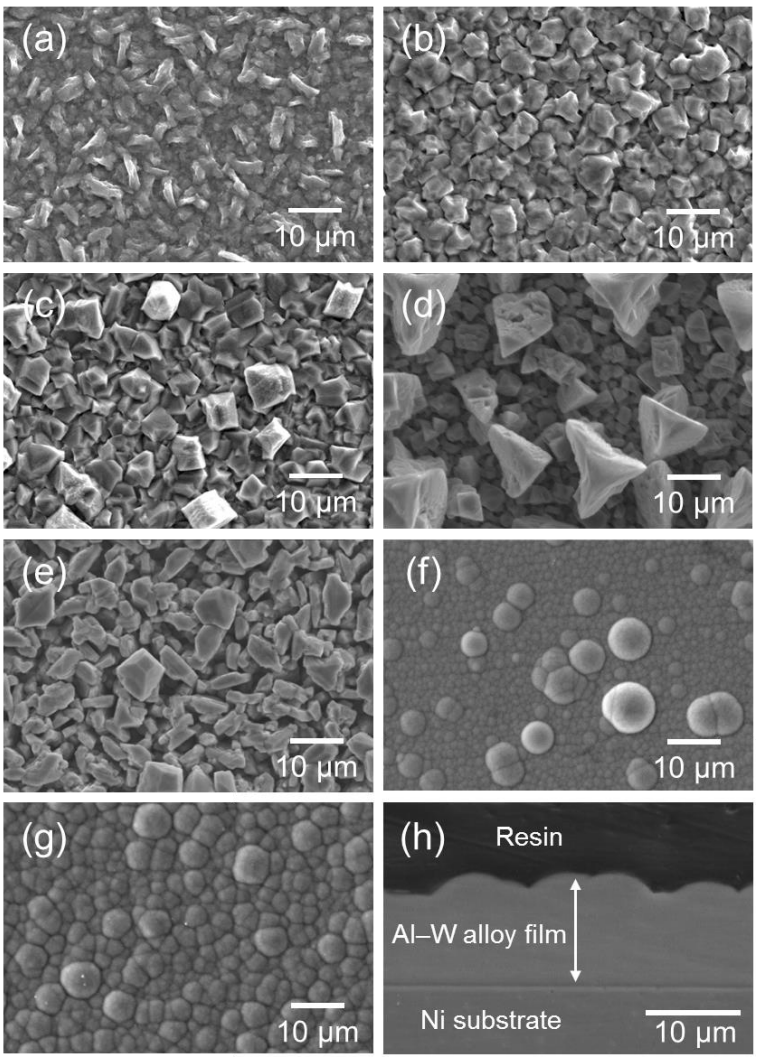

Fig. 3–3 (a–g) Surface and (h) cross-sectional SEM images of Al and Al–W alloy films obtained from EMIC–$AlCl_3$ baths containing 0–49 mM W_6Cl_{12}. The W_6Cl_{12} concentration and the W content of the films are (a) 0 mM, 0 at%, (b) 4 mM, 2.0 at%, (c) 8 mM, 5.0 at%, (d) 16 mM, 7.2 at%, (e) 20 mM, 9.8 at%, (f) 24 mM, 12.4 at%, and (g, h) 49 mM, 12.4 at%

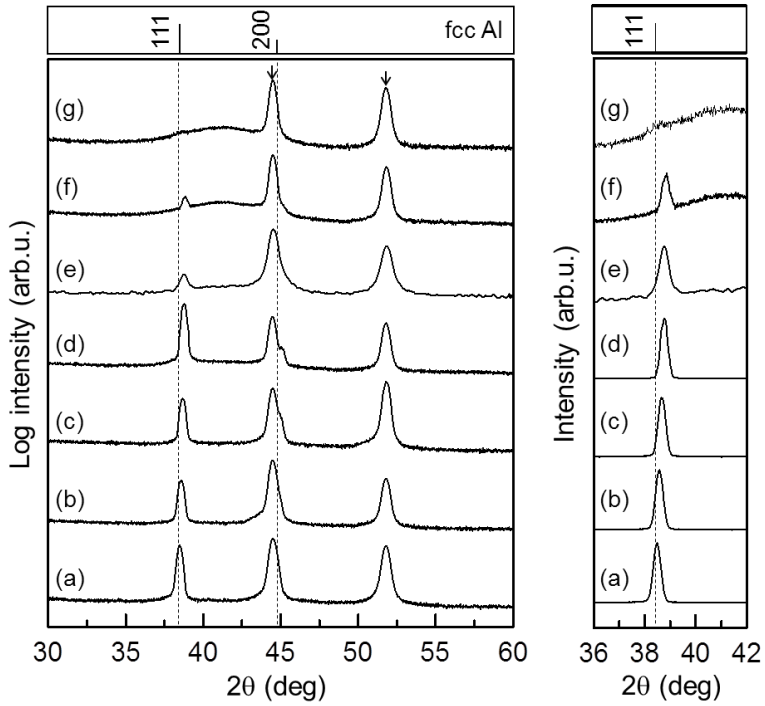

Fig. 3–4 (Left) XRD patterns of Al and Al–W alloy films obtained from EMIC–$AlCl_3$ baths containing 0–49 mM W_6Cl_{12}. The W_6Cl_{12} concentration and the W content of the films are: (a) 0 mM, 0 at%, (b) 4 mM, 2.0 at%, (c) 8 mM, 5.0 at%, (d) 16 mM, 7.2 at%, (e) 20 mM, 9.8 at%, (f) 24 mM, 12.4 at%, and (g) 49 mM, 12.4 at%. The arrows indicate the diffraction peaks from the Ni substrate. The peak positions for fcc Al (ICDD: 00-004-0787) are shown at the top of the figure. (Right) An enlarged view of the Al(111) diffraction peaks of the films.

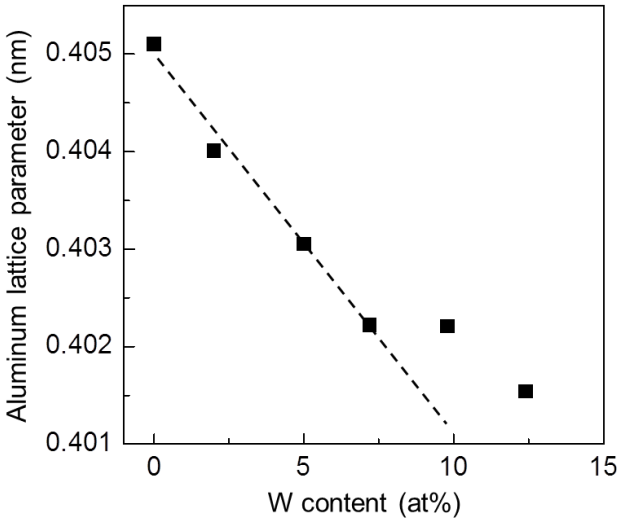

Fig. 3–5 Lattice parameter of fcc Al phase in Al and Al–W alloy films obtained from EMIC–$AlCl_3$ baths containing 0–49 mM W_6Cl_{12}.

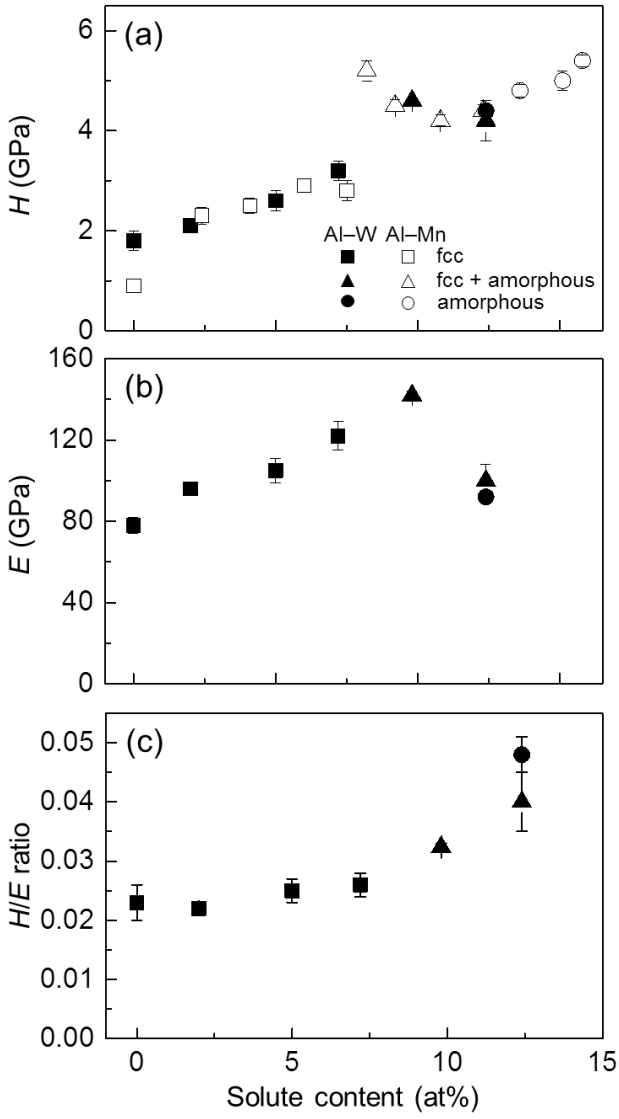

Fig. 3–6 (Solid symbols) (a) Hardness (*H*), (b) Young's modulus (*E*), and (c) *H*/*E* ratio of Al and Al–W alloy films electrodeposited from EMIC–$AlCl_3$ baths containing 0–49 mM W_6Cl_{12}. (Open symbols) Hardness of Al and Al–Mn alloy films electrodeposited from EMIC–$AlCl_3$ baths containing 0–200 mM $MnCl_2$ as reported by Ruan and Schuh (2009) [19].

Chapter 4

Electrodeposition of Al–W alloy films from electrolytes with different compositions

4.1. Introduction

In chapter 2 and 3, dense Al–W alloy films with up to ~12 at.% W were successfully electrodeposited from EMICAlCl3 bath containing W(II) chloride (W_6Cl_{12}). The resulting films were confirmed to exhibit a good corrosion resistance. In addition, these films were proven to have a higher hardness and a higher ratio of hardness to Young's modulus than Al metal, suggesting that these films could have a higher mechanical strength.

Based on these results, it was expected that Al–W alloy films with an even higher W content (>12 at.% W) would have an even higher mechanical strength. However, Al–W alloy films with the W content higher than ~12 at.% were not obtained using EMIC–$AlCl_3$ (1:2) bath. As discussed in chapter 3, the W content of the alloy films electrodeposited at a constant current density increased linearly up to ~12 at.% with increasing W_6Cl_{12} concentration of the bath in a low W_6Cl_{12} concentration range, but the W content of the films saturated at ~12 at.% at a higher W_6Cl_{12} concentration. Potentiostatic electrodeposition at various potentials in an EMIC–$AlCl_3$ bath saturated with W_6Cl_{12} also failed to produce alloy films with >~12 at.% W as discussed in chapter 2.

One of the parameters that have not yet been explored in this system is the $AlCl_3$/EMIC molar ratio of the bath. A decrease in the $AlCl_3$/EMIC molar ratio below the previously tested value of 2 is expected to suppress the electrodeposition rate of Al, and therefore, increase the W content of the resulting films. In the present study, electrodeposition in EMIC–$AlCl_3$–W_6Cl_{12} baths with an $AlCl_3$/EMIC molar ratio of 1.5 was carried out to obtain Al–W alloy films with a higher W content. The surface morphology, crystal structure, hardness, and Young's modulus of the electrodeposited films were investigated.

4.2. Methods

Preparation of the electrolytic bath, setups of the electrochemical experiments, film characterizations using SEM, EDX, XRD and nano-indentation were carried out in the same way as those described in chapter 2 and 3.

4.3. Results and Discussions

Electrolytic bath composition

Previous studies have shown that a maximum of ~12 at.% W could be obtained in Al–W alloy films were electrodeposited in EMIC–$AlCl_3$–W_6Cl_{12} baths where the $AlCl_3$/EMIC molar ratio was 2. In the present study, electrodeposition was carried out using ionic liquids with a lower $AlCl_3$/EMIC molar ratio (1.5), with the aim of obtaining alloy films with a higher W content. The compositions of the electrolytic baths employed are shown in Table 1. In the EMIC–$2AlCl_3$ bath, which had been employed in the previous studies, W_6Cl_{12} concentration reached saturation at 49 mM. The composition of this bath (bath A) is expressed as EMIC–$2AlCl_3$–$0.015W_6Cl_{12}$ in molar ratio. Bath B (EMIC–$1.5AlCl_3$–$0.015W_6Cl_{12}$ in molar ratio) has the lower $AlCl_3$/EMIC ratio of 1.5, while the W_6Cl_{12}/EMIC ratio is fixed at 0.015, as in bath A. The volume molar concentration of W_6Cl_{12} in bath B is 56 mM, which is a little higher than, but almost the same as, that in bath A. We found that W_6Cl_{12} was more soluble in EMIC–$1.5AlCl_3$ than in EMIC–$2AlCl_3$, with a W_6Cl_{12} saturation concentration in EMIC–$1.5AlCl_3$ of 105 mM. The composition of this W_6Cl_{12}-saturated bath (bath C) is expressed as EMIC–$1.5AlCl_3$–$0.027W_6Cl_{12}$.

Electrodeposition and characterization

Electrodeposition was carried out using bath B to examine the influence of the lower $AlCl_3$/EMIC ratio (1.5) on the W content of the resulting Al–W alloy films. The charge for each electrodeposition experiment was set at 8 C cm^{-2}, which is the charge required for the electrodeposition of a 2.8 μm Al film or a 3.9 μm thick W film.

Figure 4–1 compares the current density vs. electrolysis potential plots obtained during electrodeposition in baths A and B. An Al wire immersed in an EMIC–2$AlCl_3$ ionic liquid separated from the bath with a porous glass frit was used as the reference electrode. In bath A, the current density increased with the decrease in the potential from −0.1 V, which is close to the equilibrium potential of Al (0 V). In bath B, a similar trend was observed, except that the current density observed for bath B was almost half of that for bath A at each potential. Previously, Al–W alloy films with <~12 at.% W were electrodeposited in bath A at potentials of <−0.1 V, where the current efficiency was ~90% [1]. Accordingly, about 80% of the current density observed for bath A at <−0.1 V is attributed to the deposition of Al. Therefore, the lower current density observed for bath B in comparison to bath A reflects the lower deposition rate of Al in bath B. This is reasonable because of the lower $AlCl_3$ concentration of bath B.

Electrodeposition in bath B at potentials more negative than −0.1 V produced deposits on the substrate. However, the deposits obtained at >−0.2 V were fragile and easily exfoliated from the substrate during the washing process, making further analysis impossible. A typical EDX spectrum of the deposits obtained from bath B at <−0.2 V is shown in Fig. 4–2. The EDX spectrum indicates that the deposit is composed of Al and W, except for a small amount of O, which is derived from the surface oxidation layer, confirming that Al–W alloys can also be electrodeposited in bath B. The W content of the deposits determined by the EDX is shown in Fig. 4–3. The W content of the alloys obtained from bath B was higher than that from bath A at each potential. The maximum W content of the alloys obtained from bath B reached 15.7 at.%, which was higher than that from bath A, ~12 at.%.

With the aim of obtaining alloys with a further increase in W content, electrodeposition in an EMIC–1.5$AlCl_3$ bath saturated with W_6Cl_{12} (bath C) was carried out. Deposits firmly adhering to the substrate could be obtained by electrodeposition at potentials <−0.2 V, as was the case in bath B; the deposits obtained at >−0.2 V were too fragile and easily washed away. The W contents of the alloys obtained at >−0.2 V are shown in Fig. 4–3. The W contents of the alloys obtained from bath C were higher than those of the alloys from bath B, and reached 19.4 at.%, reflecting the higher W_6Cl_{12} concentration in bath C in comparison to bath B.

Figure 4–4 presents the typical surface SEM images of the alloys with >15 at.% W obtained from the EMIC–1.5$AlCl_3$ baths. These alloys are mainly composed of globular grains without defined facets. The alloys with W content up to ~18 at.% exhibit a dense and relatively smooth morphology (Fig. 4–4a). However, the alloys with higher W contents, exceeding 18 at.%, exhibit a rough surface with conical-shaped needle-like grains (Fig. 4–4b). Similar needle-like grains have also been observed in the electrodeposition of other Al-based alloys such as Al-Mo-Mn and Al-Mo-Ti [2,3]. Although the detailed mechanism is not clear, the needle-like grains commonly tend to be formed when the electrodeposition is performed at a low overpotential (i.e., at a low deposition rate) in a bath with a high concentration of the ions of the alloy constituents. The formation of the needle-like grains may be attributed to the adsorption of the metal ions, which suppress the electrodeposition of Al onto the surface of the electrodeposit.

Figure 4–5 presents the typical XRD patterns of the alloy films with >15 at.% W obtained from the EMIC–1.5$AlCl_3$ baths. Apart from the diffraction peaks of the Cu substrate, the XRD patterns of these alloy films show only a halo at around $2\theta = 42°$, indicating that these films are composed of an amorphous phase. Previous studies using EMIC–2$AlCl_3$ baths showed that the electrodeposited alloys with <~10 at.% W are composed of a single phase, a solid-solution of fcc Al containing W atoms; the alloys with >~10 at.% W comprise two phases, the fcc Al and an amorphous phase, with the proportion of the amorphous phase increasing with increasing W content; the alloys with ~12 at.% W are composed of a single amorphous phase [4]. The present results show that the single amorphous phase extends up to at least 19.4 at.% W.

As described above, Al–W amorphous alloy films with high W contents exceeding ~12 at.% were obtained by using baths with the low $AlCl_3$/EMIC molar ratio of 1.5. We also examined baths with an even lower $AlCl_3$/EMIC molar ratio of 1.2. However, alloys with a high W content could not be obtained because only a small amount of W_6Cl_{12} dissolved in such baths.

Nano-indentation test

The hardness (*H*) and Young's modulus (*E*) values of a high W content film (17.7 at.% W) were evaluated using nano-indentation. Although a higher W content alloy (19.4 at.% W) was obtained, reliable data for this alloy could not be obtained from the nano-indentation test because of the increased surface roughness visible in Fig. 4–4b.

The *H* and *E* values of the 17.7 at.% W film are shown in Figs. 4–6a and b. The figures also show the *H* and *E* values of the 0–12 at.% W films examined in chapter 3. The trend in the variation of the *H* and *E* values is explained by the W content and phase of the films. The *H* value of the <10 at.% W films, which are single-phase fcc Al solid solutions, increases with increasing W content. The *H* value of the ~10 at.% W film, where the fcc Al phase coexists with an amorphous phase, shows a local maximum. With a further increase in W content to ~12 at.%, the presence of the amorphous phase increases and the *H* value slightly decreases. The variation in *E* is similar to that for the *H* values.

The 17.7 at.% W film obtained in the present study is composed of a single amorphous phase, and its W content is higher than that of the single amorphous W film obtained previously (12 at.%). The *H* and *E* values for the 17.7 at.% W films are higher than those for the ~12 at.% W films. The increases in *H* and *E* values for the single amorphous films with increasing W content can be understood in terms of the average interatomic distance. As is the case with crystalline alloys, the elastic behavior of amorphous alloys depends on the interatomic distance [5–7]. A decrease in interatomic distance leads to stiffer interatomic bonding, resulting in a higher *E* value. In addition, the plastic deformation, which is related to *H*, of an amorphous alloy is considered to proceed by the propagation of shear displacement in a group of atoms wherein the interatomic distance is relatively large [8,9]. Therefore, the decrease in the average interatomic distance increases the resistance to shear displacement, resulting in a higher *H* value [10]. Because W has a smaller atomic radius than Al, the average interatomic distance in Al–W alloy films should decrease with increasing content of W atoms [1,4,11]. Therefore, the higher *H* and *E* values of the 17.7 at.% W film in comparison to those of the ~12 at.% W amorphous films are reasonable.

Coating materials with a high hardness (*H*) value and a high ratio of hardness to Young's modulus (*H*/*E*) are believed to have a high wear resistance. As shown in Figs. 4–6a and c, the *H* value and *H*/*E* ratio of the 17.7 at.% W film are higher than those of the <~12 at.% W film containing the fcc Al phase. A comparison between the values of the single-phase amorphous films with ~12 at.% W and 17.7 at.% W proves that the *H*/*E* ratio is almost the same for these two films, but *H* value is higher for the 17.7 at.% W film. Therefore, the 17.7 at.% W film obtained in the present study is expected to have a higher resistance to mechanical damages than the films obtained previously.

4.4. Conclusion

Electrodeposition of Al–W alloys in EMIC–$AlCl_3$–W_6Cl_{12} baths with $AlCl_3$/EMIC molar ratios lower than 2 was examined. W_6Cl_{12} was more soluble in EMIC–1.5$AlCl_3$ than in EMIC–2$AlCl_3$, but was much less soluble in EMIC–1.2$AlCl_3$ bath. Electrodeposition in the EMIC–1.5$AlCl_3$ baths generated alloy films with up to 19.4 at.% W, which was higher than those previously obtained from EMIC–2$AlCl_3$ baths (~12 at.% W). The increase in W content for the EMIC–1.5$AlCl_3$ baths can be explained by the lower deposition ratio of Al and higher W_6Cl_{12} concentration. Alloy films with up to ~18 at.% W were dense and smooth, whereas those with >~18 at.% W exhibited a rough surface. The hardness of the 17.7 at.% W film was higher than those of the Al–W alloy films previously obtained from EMIC–2$AlCl_3$ baths, owing to the higher W content of the film. Young's modulus also increased with the increase in W content from 12 to 17.7 at.%, while the ratio of hardness to Young's modulus remained almost constant.

References

[1] S. Higashino, M. Miyake, H. Fujii, A. Takahashi, T. Hirato, Electrodeposition of Al-W Alloy Films in a 1-Ethyl-3-methyl-imidazolium Chloride-$AlCl_3$ Ionic Liquid Containing W_6Cl_{12}, J. Electrochem. Soc. 164 (2017) D120–D125. https://doi.org/10.1149/2.0131704jes.

[2] T. Tsuda, C.L. Hussey, G.R. Stafford, Electrodeposition of Al-Mo-Mn Ternary Alloys from the Lewis Acidic AlCl3-EtMeImCl Molten Salt, J. Electrochem. Soc. 152 (2005) C620–C625. https://doi.org/10.1149/1.1995696.

[3] T. Tsuda, S. Arimoto, S. Kuwabata, Electrodeposition of Al–Mo–Ti Ternary Alloys in the Lewis Acidic Aluminum Chloride–1-Ethyl-3-methylimidazolium Chloride Room-Temperature Ionic Liquid, J. Electrochem. Soc. 155 (2008) D256–D262. https://doi.org/10.1149/1.2833305.

[4] S. Higashino, M. Miyake, A. Takahashi, Y. Matamura, H. Fujii, R. Kasada, T. Hirato, Evaluation of the hardness and Young's modulus of electrodeposited Al–W alloy films by nano-indentation, Surf. Coatings Technol. 325 (2017) 346–351. https://doi.org/10.1016/j.surfcoat.2017.06.064.

[5] T. Rouxel, Elastic properties and short-to medium-range order in glasses, J. Am. Ceram. Soc. 90 (2007) 3019–3039. https://doi.org/10.1111/j.1551-2916.2007.01945.x.

[6] J.G. Wang, B.W. Choi, T.G. Nieh, C.T. Liu, Crystallization and nanoindentation behavior of a bulk Zr–Al–Ti–Cu–Ni amorphous alloy, J. Mater. Res. 15 (2000) 798–807. https://doi.org/10.1557/JMR.2000.0114.

[7] C.C. Yuan, X.K. Xi, On the correlation of Young's modulus and the fracture strength of metallic glasses, J. Appl. Phys. 109 (2011) 033515. https://doi.org/10.1063/1.3544202.

[8] C.A. Schuh, T.C. Hufnagel, U. Ramamurty, Mechanical behavior of amorphous alloys, Acta Mater. 55 (2007) 4067–4109. https://doi.org/10.1016/j.actamat.2007.01.052.

[9] A.S. Argon, Plastic deformation in metallic glasses, Acta Metall. 27 (1979) 47–58. https://doi.org/10.1016/0001-6160(79)90055-5.

[10] D. Pan, Y. Yokoyama, T. Fujita, Y.H. Liu, S. Kohara, A. Inoue, M.W. Chen, Correlation between structural relaxation and shear transformation zone volume of a bulk metallic glass, Appl. Phys. Lett. 95 (2009) 141909. https://doi.org/10.1063/1.3246151.

[11] T. Tsuda, Y. Ikeda, T. Arimura, M. Hirogaki, A. Imanishi, S. Kuwabata, G.R. Stafford, C.L. Hussey, Electrodeposition of Al-W Alloys in the Lewis Acidic Aluminum Chloride-1-Ethyl-3-Methylimidazolium Chloride Ionic Liquid, J. Electrochem. Soc. 161 (2014) D405–D412. https://doi.org/10.1149/06404.0563ecst.

Table 4–1. Bath compositions employed in our previous (bath A) and present studies (baths B and C).

Bath	EMIC:$AlCl_3$:W_6Cl_{12} (molar ratio)	W_6Cl_{12} concentration (mM)
A	1:2:0.015	49
B	1:1.5:0.015	56
C	1:1.5:0.027	105

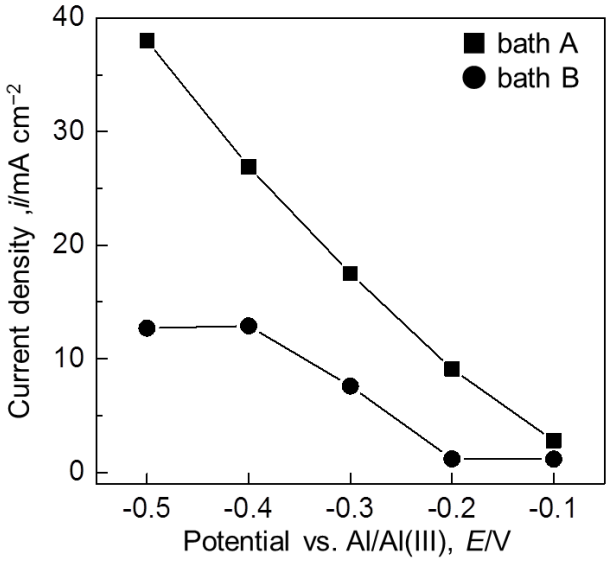

Figure 4–1. Current density vs. electrolysis potential during electrodeposition in baths A and B.

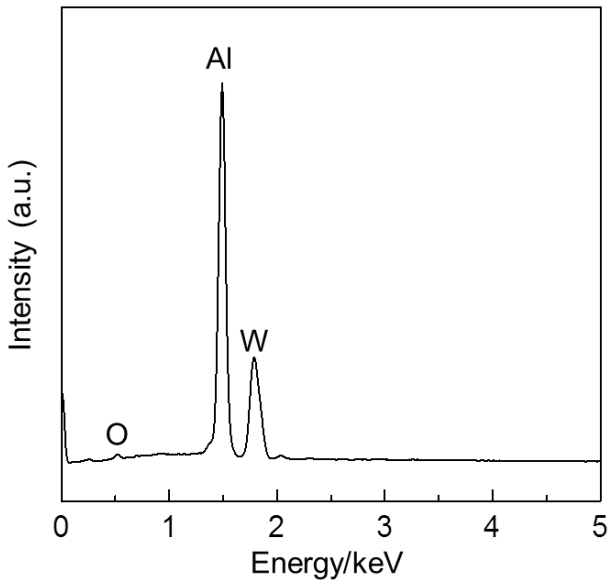

Figure 4–2. EDX spectra of the deposit electrodeposited in bath B at −0.2 V.

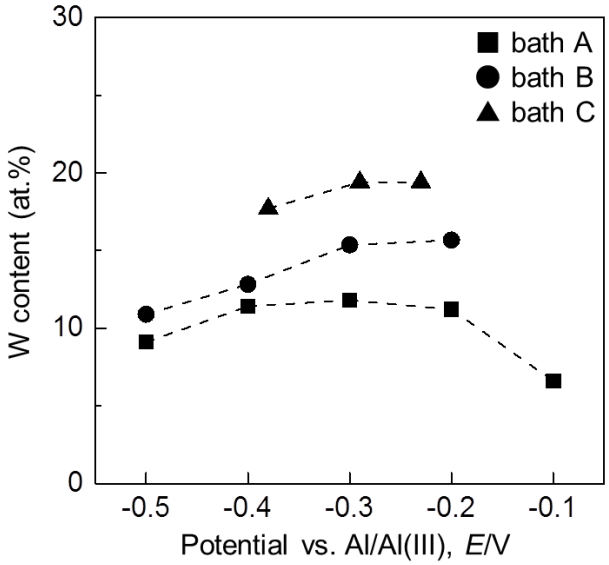

Figure 4–3. W contents of electrodeposited Al–W alloy films vs. electrolysis potential during electrodeposition.

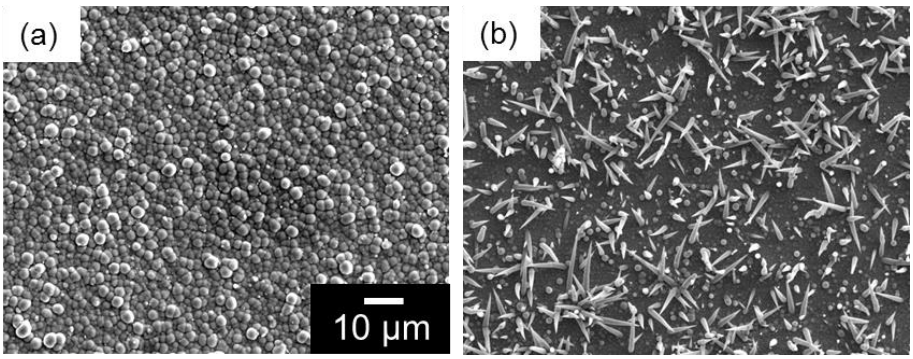

Figure 4–4. Surface SEM images of Al–W alloy films with (a) 17.7 and (b) 19.4 at.% W. These films were electrodeposited from bath C at potentials of −0.23 V and −0.38 V, respectively.

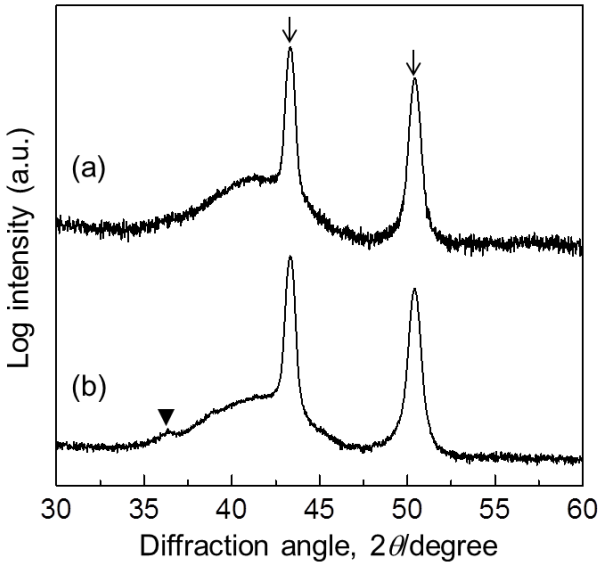

Figure 4–5. Typical XRD patterns of Al–W alloy films with >15 at.% W. The W contents are (a) 19.4 and (b) 17.7 at.%. The arrows indicate the diffraction peaks from the Cu substrate. The solid triangle (▼) indicates the diffraction peak from Cu_2O, which is obtained from the oxidation of the Cu substrate.

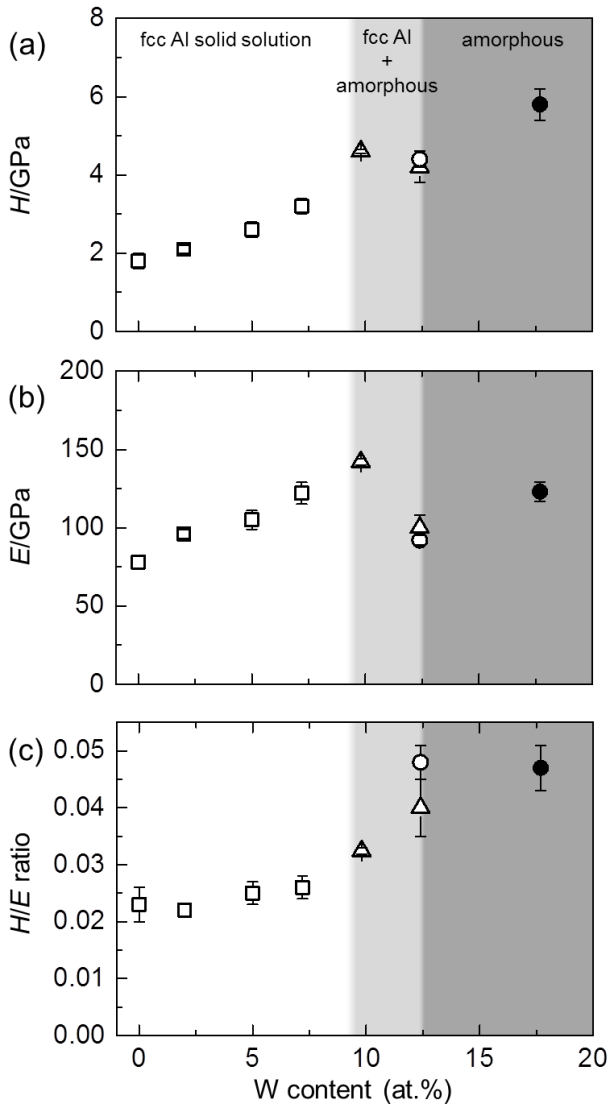

Figure 4–6. (a) Hardness (*H*), (b) Young's modulus (*E*), and (c) *H*/*E* ratio of Al–W alloy films. Solid symbols indicate the data for the 17.7 at.% W film, which was newly obtained in this study. The 17.7 at.% W film was electrodeposited from bath C at potentials of −0.38 V. Square, triangle, and circle symbols represent the fcc Al solid solution phase, fcc Al + amorphous coexisting phase, and single amorphous phase, respectively.

Chapter 5

Formation of a photocatalytic WO_3 surface layer on electrodeposited Al–W alloy films by selective dissolution and heat treatment

5.1. Introduction

In chapters 2–4, dense Al–W alloy films with W contents of up to 18 at.% were electrodeposited from EMIC–$AlCl_3$ ionic liquids containing W_6Cl_{12}.

Meanwhile, self-cleaning coatings have been developed extensively, owing to the practical advantages of energy savings and environmental compatibility [1–4]. Such coatings can be obtained by forming a hydrophilic surface layer with a photocatalytic material, such as titanium dioxide (TiO_2), which catalyzes the photodecomposition of adsorbed organic compounds [1,2,4–7]. TiO_2-based coatings only exhibit self-cleaning properties when exposed to UV illumination, such as sunlight. This behavior is due to the wide bandgap of TiO_2 (~3.2 eV). In contrast, tungsten oxide (WO_3), which has a narrower bandgap of 2.5–2.8 eV, can absorb visible light energy. WO_3 thus exhibits self-cleaning properties under visible light illumination [8–11].

This chapter describes a new process for imparting corrosion-resistant Al–W alloy films with self-cleaning properties through the formation of a WO_3 surface layer. This process is comprised of a chemical dissolution step and heat treatment. Al is selectively removed by dissolution in an acidic solution, and a W-enriched layer is formed at the surface of the Al–W alloy film. Subsequent heat treatment in air converts the W-enriched surface layer to photocatalytic WO_3. Through this process, a corrosion-resistant Al–W coating with self-cleaning ability under visible light illumination is obtained. Many strategies for preparing WO_3 surface layers have been reported in the literature, including sputtering [12–14], chemical vapor deposition [15], vacuum evaporation [16], spin-coating [8], spray pyrolysis [17,18], sol–gel processing [19,20], and hydrothermal growth [9,21]. The process described herein differs from these routes in that W present in the alloy film itself serves as the WO_3 precursor;

hence, no additional W precursor is required. For this reason, this process is cost-effective and facilitates successive and large-scale production.

In this study, the feasibility of forming photocatalytic WO_3 layers on Al–W alloy films via this process was examined. The conditions required for the formation of photocatalytic WO_3 on Al–W alloy films were determined. Then, the self-cleaning properties of the WO_3/Al–W alloy films were evaluated by monitoring the photodegradation of stearic acid (SA) and methylene blue (MB) under visible light illumination. Finally, the corrosion resistance of the WO_3/Al–W alloy films was confirmed.

5.2. Methods

Electrodeposition of Al–W alloy films

Preparation of the electrolytic bath and setups of the electrochemical experiments, film characterizations using XRD and potentiodynamic polarization were carried out in the same way as those described in chapter 2 and 3. In the present study, a 100 nm thick Cu film formed on a glass substrate by sputtering was used. The purpose of using this Cu/glass substrate was to make the cross-section observation easier. A part of the Cu/glass substrate was covered with polytetrafluoroethylene tape, such that a defined 1 × 1 cm^2 area was exposed to the bath.

Selective dissolution and heat treatment of Al–W alloy films

The electrodeposited Al–W alloy films were mechanically polished to obtain smooth surfaces. The portion of each Cu substrate on which the alloy film was not deposited was covered with KTC-AC-828T masking resin (Kakoki Trading Co., Japan), after which the films were immersed in 0.56 M (3.5 wt.%) aqueous HNO_3 solution at room temperature.

The films were heat treated in a KBF848N1 electric furnace (Koyo Thermo Systems Co., Japan) in air. The films were heated from room temperature to the desired temperature at a rate of 2 °C min^{-1}, held at that temperature for 10 h, and then cooled slowly over several hours to room temperature.

The surface and cross-sectional morphologies of the alloy films were examined by field-emission

scanning electron microscopy (FE-SEM), and the elemental compositions of the films were determined by EDX on a SU6600 field-emission scanning electron microscope (Hitachi, Japan) equipped with a Quantax Xflash 4010 detector (Bruker, USA). To prevent charging effects during the SEM analysis, a thin Au coating was deposited onto the samples by sputtering.

The XPS spectra of the film surfaces were analyzed by using JPS-9030 (JEOL, Japan) with Mg Kα (1253.6 eV) X-ray source. The spectra in this paper were calibrated using C1s peak at 285eV.

Evaluation of photocatalytic self-cleaning properties

The photocatalytic self-cleaning properties of the films were evaluated by monitoring the photodegradation of SA and MB [2]. The reagents used in these tests were purchased from Wako Chemical Co. (Japan) and used as received. For both tests, the films were illuminated with visible light at wavelengths from 380 to 520 nm. The light was emitted from a HAL-320 xenon solar simulator lamp (Asahi Spectra, Japan) with a light intensity of 1 sun passed through a Super Cold 750 filter and an SHPF-25C-533 short-pass filter (SIGMA KOKI, Japan) with a transmittance range of 380–520 nm. Wavelengths of >520 nm were blocked to prevent self-decomposition of MB via light absorption.

The photodegradation of SA was monitored according to the Japan Industrial Standards R_1753 method (2013). Each alloy film was illuminated with a LUV-16 UV lamp (ASONE Co., Japan) for 24 h in a dark room to ensure that the surface was devoid of interferents. Each film was then coated with a thin layer of SA by spin-coating 1 mL of 0.3 wt.% SA solution in heptane at 2000 rpm and dried at 70 °C on a hot plate for 10 min. Following SA coating, each film was illuminated under visible light from the solar simulator lamp in a dark room. The contact angle of a water droplet (<1 μL) on each film was measured with a ME2 contact angle meter (Asumi Giken Co., Japan).

For the photodegradation of MB, each film was first immersed in a large volume of aqueous 5 μM MB solution for >12 h to ensure that the adsorption/desorption equilibrium was reached. The film was then placed in a 4.5 mL acryl vial containing 1.5 mL of 5 μM MB solution and illuminated with visible light. The absorption spectrum of the MB solution was collected with a UV-2450 UV-VIS spectrometer

(Shimadzu, Japan). The absorbance at 663 nm was used to determine the MB concentration according to Beer's law.

5.3. Results and discussion

Electrodeposition of Al–W alloy films

The typical energy-dispersive X-ray spectroscopy (EDX) spectrum of an electrodeposited Al–W alloy film in Fig. 5–1a indicates that only Al and W are present in the film. No other elements were detected, except for a small amount of O due to surface oxidation. The W content of the alloy film was determined to be ~12 at.% based on the EDX spectrum. The X-ray diffraction (XRD) pattern (Fig. 5–3a) shows halos located at approximately $2\theta = 21°$ and 42°, indicating that the as-deposited alloy film was amorphous. The average film thickness was ~11 μm.

Selective dissolution of Al–W alloy films

In the first attempt to form a surface oxidation layer, the electrodeposited Al–W alloy film was heated in air. However, this thermal oxidation of the as-deposited film generated a complex oxide ($Al_2O_3 \cdot 3WO_3$) rather than single phase WO_3 (Fig. 5–2a). The photocatalytic activity of the thermally oxidized film ($Al_2O_3 \cdot 3WO_3$/Al–W alloy) was negligible (Fig. 5–2b).

To obtain WO_3 instead of the complex oxide, the W content of the alloy film had to be increased prior to thermal oxidation. The Al–W alloy films were immersed in 0.56 M (3.5 wt.%) aqueous nitric acid (HNO_3) solution before heat treatment, with the intention of dissolving Al selectively to form a W-enriched surface layer. Figure 5–1b shows a typical EDX spectrum collected from the surface of an alloy film immersed in aqueous HNO_3 for >15 h. The amount of Al was significantly reduced after immersion in aq. HNO_3, indicating that Al was selectively dissolved from the Al–W alloy films. This result is consistent with the expected behavior based on potential–pH diagrams [22], which show that Al dissolves in acidic solutions, whereas W is passivated. The increased amount of O indicated that oxidation of residual W proceeded simultaneously during the dissolution process. The XRD patterns

of the films after selective dissolution for different durations are shown in Fig. 5–3b–d. The pattern of the film after 9 h (Fig. 5–3b) contained no diffraction peaks except for the amorphous halo pattern of the Al–W alloy. In contrast, faint diffraction peaks attributed to $H_2WO_4 \cdot H_2O$ (JCPDS: 18-1420) and an intense peak near 28° were observed in the pattern of the film treated for 12 h (Fig. 5–3c). The peak near 28° may be derived from $WO_3 \cdot 0.33H_2O$, but this is not a certainty owing to the absence of other diffraction peaks. The film treated for >15 h (Fig. 5–3d) clearly yielded a diffraction pattern corresponding to $H_2WO_4 \cdot H_2O$.

Liu et al. reported that selective dissolution of a sputtered W-rich Al–W alloy film (>45 at.% W) under similar conditions yielded a metallic β-W phase [23]. The formation of $H_2WO_4 \cdot H_2O$ in the present work could be attributed to the lower W content of the starting alloy, which contained 12 at.% W. The dissolution of Al from the Al–W alloy with the lower W content should generate many atomic vacancies and the residual W atoms should have relatively weak metallic bonding to each other. Thus, these W atoms are highly active, resulting in a higher probability of being oxidized to form bulk $H_2WO_4 \cdot H_2O$ [24,25]. The formation of $H_2WO_4 \cdot H_2O$ by selective dissolution of electrodeposited Fe–W alloy films has also been reported, although the W content of the alloy films was not indicated [26].

Figure 5–4 shows surface scanning electron microscopy (SEM) images of the alloy films after selective dissolution for various durations. Small cracks a few hundred nanometers in length were observed at 9 h (Fig. 5–4a). These cracks were attributed to volume shrinkage caused by Al dissolution at the surface. With increasing duration, portions of the film along the cracks were exfoliated, but one side remained attached to the film surface to form petal-like structures, as indicated by arrows in Fig. 5–4b. Based on the XRD pattern shown in Fig. 5–3c, the petals in Fig. 5–4b were composed of $WO_3 \cdot 0.33H_2O$ and $H_2WO_4 \cdot H_2O$. The petals covered the entire surface by 15 h (Fig. 5–4c), at which point they were composed of $H_2WO_4 \cdot H_2O$ (Fig. 5–3d). The width and thickness of each $H_2WO_4 \cdot H_2O$ petal were <300 nm and <50 nm, respectively. A similar petal-like morphology is commonly observed following selective dissolution of sputtered Al–W alloy films containing >45 at.% W [23] and electrodeposited Fe–W alloy films [26], although the residue of the former is composed of β-W and

that of the latter is composed of $H_2WO_4 \cdot H_2O$. Increasing the dissolution duration from 15 to 24 h (Fig. 5–4c and d) did not cause a notable change in the petal-like morphology, but the film treated for 24 h suffered from significant volume shrinkage that generated macroscopic cracks a few micrometers in width. Based on these results, a dissolution duration of 15 h was selected for the following experiments.

Dehydration of $H_2WO_4 \cdot H_2O$ to WO_3

Since $H_2WO_4 \cdot H_2O$ is known to have negligible photocatalytic activity [27,28], heat treatment was performed in air to dehydrate $H_2WO_4 \cdot H_2O$ to photocatalytic WO_3. The XRD patterns obtained after heat treatment (Fig. 5–3e and f) show that $H_2WO_4 \cdot H_2O$ was converted to cubic (c)-WO_3 (JCPDS: 41-0905) at 300 °C and orthorhombic (o)-WO_3 (JCPDS: 20-1324) at 350 °C. These results were consistent with those in a previous report [29], which showed that $H_2WO_4 \cdot H_2O$ was dehydrated to c-WO_3 at 300 °C and converted to o-WO_3 by heating at 300 °C for a longer duration. The X-ray photoelectron spectroscopy (XPS) W 4f spectra of the films showed that W existed as W^{4+}, W^{5+}, and W^{6+} in $H_2WO_4 \cdot H_2O$, with subsequent heat treatment causing complete conversion to W^{6+} (Fig. 5–5a). The XPS Al 2s spectra confirmed that the WO_3 phase after heat treatment contained no elemental Al (Fig. 5–5b).

Surface SEM images (Fig. 5–6a and b) revealed that the petal-like grains were almost unchanged by heating at 300 °C, whereas the grains were sintered at 350 °C to form more compact grains. The cross-sectional image of an Al–W alloy film following heat treatment at 350 °C (Fig. 5–6c) shows that an ~300 nm thick WO_3 layer was formed on the film. The EDX spectrum of the Al–W alloy underlayer (Fig. 5–6d) indicated that it remained unoxidized, and the alloy composition was nearly identical to that of the as-deposited film.

It was thought that heat treatment at even higher temperatures might generate WO_3 with enhanced photocatalytic performance [30]. However, heat treatment at temperatures of 400 °C or higher crystallized the amorphous Al–W alloy to form intermetallic compounds such as Al_5W and $Al_{12}W$ (Fig. 5–7). The films containing these compounds were quite brittle and thus impractical for use as coatings.

Photocatalytic self-cleaning properties of WO_3/Al–W alloy films

Photocatalytic degradation of SA and methylene blue (MB) on the WO_3/Al–W alloy films obtained by selective dissolution and heat treatment as described above was examined to evaluate the self-cleaning properties of the films. The photodecomposition of SA was monitored by measuring the change in the water contact angle on the film coated with SA. Absorption spectra of MB solutions in contact with the films were analyzed to monitor the photodegradation of MB.

The water contact angle on each film was measured under illumination with visible light after the film was treated with SA solution in heptane. For comparison, the contact angle on a bare Al–W alloy film was also measured following treatment with SA solution in heptane. As shown in Fig. 5–8, the contact angle on each film prior to illumination (t = 0 h) exceeded 50° due to the hydrophobicity of the SA adsorbed on the film surfaces. The contact angle for the bare Al–W alloy films remained almost constant regardless of illumination time, indicating the SA was present on the surface. In contrast, the contact angles on the c-WO_3 and o-WO_3 films decreased with increasing illumination time, indicating these films photocatalyzed the degradation of SA. The contact angle decreased more rapidly on the o-WO_3 film than on the c-WO_3 film.

The concentrations of MB in aqueous solutions in contact with the o-WO_3 and c-WO_3 films under visible light illumination were calculated from the absorption spectra of MB (Fig. 5–9a). The variations of the MB concentration in aqueous solutions in contact with the c-WO_3 and o-WO_3 films under visible light illumination are shown in Fig. 5–9b. The MB concentration remained almost constant in the solution with the c-WO_3 film, whereas the MB concentration decreased with increasing illumination time in the solution with the o-WO_3 film. This result demonstrated that the o-WO_3 film could photocatalyze the degradation of MB. The inability of the c-WO_3 film to photocatalyze the degradation of MB has been reported elsewhere and was attributed to the c-WO_3 bandgap of 2.0 eV [31], which is lower than those of WO_3 in the orthorhombic and monoclinic phases (2.5–2.8 eV) [30,32,33].

Based on the photocatalytic degradation results for SA and MB, the o-WO_3/Al–W alloy film

photodegraded organic compounds adsorbed on its surface more effectively than the c-WO_3/Al–W film. Thus, the self-cleaning ability of the o-WO_3/Al–W alloy film is superior to that of the c-WO_3/Al–W film.

Corrosion resistance of the WO_3/Al–W alloy films

The resistance of the o-WO_3/Al–W alloy film to pitting corrosion was investigated by measuring the pitting potential in 3.5 wt.% aqueous NaCl solution through potentiodynamic polarization tests. The polarization curve of the o-WO_3/Al–W alloy film is shown in Fig. 5–10, with the polarization curves of bare Al–W alloy films containing 12.4 and 10.5 at.% W and an Al plate included for comparison. In each of the curves, the anodic current density exhibited a steep rise at a certain potential. This steep rise was attributed to pitting corrosion on the surface of the alloy films. The pitting potential of the o-WO_3/Al–W alloy film was lower than that of the bare alloy film with a similar W content (12.4 at.% W); however, it was higher than those of the Al–W alloy film with 10.5 at.% W and the Al plate.

5.4. Conclusion

A photocatalytic WO_3 surface layer was formed on electrodeposited Al–W alloy films by selective dissolution and heat treatment. The selective dissolution of Al and oxidation of W proceeded during immersion of the Al–W alloy films in an aqueous HNO_3 solution and nanostructured $H_2WO_4 \cdot H_2O$ was formed on the alloy surface. Subsequently, $H_2WO_4 \cdot H_2O$ was dehydrated to c-WO_3 or o-WO_3 by heat treatment at 300 or 350 °C, respectively. The orthorhombic WO_3/Al–W alloy film exhibited superior visible-light photocatalytic activity for the photodegradation of SA and MB adsorbed on the surface. Although the resistance of the WO_3/Al–W alloy film to pitting corrosion was slightly lower than that of the untreated Al–W alloy film, it was still better than that of the Al–W alloy film with 10.5 at.% W. These results demonstrate the feasibility of selective dissolution and heat treatment as a new process to obtain corrosion-resistant alloy films with photocatalytic self-cleaning abilities under visible light

illumination.

References

[1] I.P. Parkin, R.G. Palgrave, Self-cleaning coatings, J. Mater. Chem. 15 (2005) 1689–1695. https://doi.org/10.1039/b412803f.

[2] L. Zhang, R. Dillert, D. Bahnemann, M. Vormoor, Photo-induced hydrophilicity and self-cleaning: models and reality, Energy Environ. Sci. 5 (2012) 7491–7507. https://doi.org/10.1039/c2ee03390a.

[3] L. Yao, J. He, Recent progress in antireflection and self-cleaning technology — From surface engineering to functional surfaces, Prog. Mater. Sci. 61 (2014) 94–143. https://doi.org/10.1016/j.pmatsci.2013.12.003.

[4] S. Banerjee, D.D. Dionysiou, S.C. Pillai, Self-cleaning applications of TiO_2 by photo-induced hydrophilicity and photocatalysis, Appl. Catal. B Environ. 176–177 (2015) 396–428. https://doi.org/10.1016/j.apcatb.2015.03.058.

[5] M. Miyauchi, A. Nakajima, T. Watanabe, K. Hashimoto, Photocatalysis and Photoinduced Hydrophilicity of Various Metal Oxide Thin Films, Chem. Mater. 14 (2002) 2812–2816. https://doi.org/10.1021/cm020076p.

[6] S. Anandan, T. Narasinga Rao, M. Sathish, D. Rangappa, I. Honma, M. Miyauchi, Superhydrophilic graphene-loaded TiO_2 thin film for self-cleaning applications, ACS Appl. Mater. Interfaces. 5 (2013) 207–212. https://doi.org/10.1021/am302557z.

[7] S. Spanou, A.I. Kontos, A. Siokou, A.G. Kontos, N. Vaenas, P. Falaras, E.A. Pavlatou, Self cleaning behaviour of Ni/nano-TiO_2 metal matrix composites, Electrochim. Acta. 105 (2013) 324–332. https://doi.org/10.1016/j.electacta.2013.04.174.

[8] M. Miyauchi, M. Shibuya, Z.-G. Zhao, Z. Liu, Surface Wetting Behavior of a WO3 Electrode under Light-Irradiated or Potential-Controlled Conditions, J. Phys. Chem. C. 113 (2009) 10642–10646. https://doi.org/10.1021/jp901097b.

[9] D. Vernardou, H. Drosos, E. Spanakis, E. Koudoumas, C. Savvakis, N. Katsarakis, Electrochemical and photocatalytic properties of WO_3 coatings grown at low temperatures, J.

Mater. Chem. 21 (2011) 513–517. https://doi.org/10.1039/c0jm02413a.

[10] H. Zheng, J.Z. Ou, M.S. Strano, R.B. Kaner, A. Mitchell, K. Kalantar-Zadeh, Nanostructured tungsten oxide - Properties, synthesis, and applications, Adv. Funct. Mater. 21 (2011) 2175–2196. https://doi.org/10.1002/adfm.201002477.

[11] M. Miyauchi, Photocatalysis and photoinduced hydrophilicity of WO_3 thin films with underlying Pt nanoparticles, Phys. Chem. Chem. Phys. 10 (2008) 6258–6265. https://doi.org/10.1039/b807426g.

[12] M.H. Yaacob, M. Breedon, K. Kalantar-zadeh, W. Wlodarski, Absorption spectral response of nanotextured WO_3 thin films with Pt catalyst towards H_2, Sensors Actuators, B Chem. 137 (2009) 115–120. https://doi.org/10.1016/j.snb.2008.12.035.

[13] H. Zheng, A.Z. Sadek, K. Latham, K. Kalantar-Zadeh, Nanoporous WO_3 from anodized RF sputtered tungsten thin films, Electrochem. Commun. 11 (2009) 768–771. https://doi.org/10.1016/j.elecom.2009.01.033.

[14] V. Khatko, G. Gorokh, A. Mozalev, D. Solovei, E. Llobet, X. Vilanova, X. Correig, Tungsten trioxide sensing layers on highly ordered nanoporous alumina template, Sensors Actuators, B Chem. 118 (2006) 255–262. https://doi.org/10.1016/j.snb.2006.04.030.

[15] D. Vernardou, K. Psifis, D. Louloudakis, G. Papadimitropoulos, D. Davazoglou, N. Katsarakis, E. Koudoumas, Low Pressure CVD of Electrochromic WO_3 at 400°C, J. Electrochem. Soc. 162 (2015) H579–H582. https://doi.org/10.1149/2.0281509jes.

[16] A. Arfaoui, S. Touihri, A. Mhamdi, A. Labidi, T. Manoubi, Structural, morphological, gas sensing and photocatalytic characterization of MoO_3 and WO_3 thin films prepared by the thermal vacuum evaporation technique, Appl. Surf. Sci. 357 (2015) 1089–1096. https://doi.org/10.1016/j.apsusc.2015.09.124.

[17] V. V. Ganbavle, S. V. Mohite, J.H. Kim, K.Y. Rajpure, Effect of solution concentration on physicochemical and gas sensing properties of sprayed WO_3 thin films, Curr. Appl. Phys. 15 (2015) 84–93. https://doi.org/10.1016/j.cap.2014.11.004.

[18] D. Chatzikyriakou, A. Maho, R. Cloots, C. Henrist, Ultrasonic spray pyrolysis as a processing route for templated electrochromic tungsten oxide films, Microporous Mesoporous Mater. 240 (2017) 31–38. https://doi.org/10.1016/j.micromeso.2016.11.001.

[19] M. Breedon, P. Spizzirri, M. Taylor, J. Du Plessis, D. McCulloch, J. Zhu, L. Yu, Z. Hu, C. Rix, W. Wlodarski, K. Kalantar-zadeh, Synthesis of nanostructured tungsten oxide thin films: A simple, controllable, inexpensive, aqueous sol-gel method, Cryst. Growth Des. 10 (2010) 430–439. https://doi.org/10.1021/cg9010295.

[20] K.D. Lee, Preparation and electrochromic properties of WO_3 coating deposited by the sol–gel method., Sol. Energy Mater. Sol. Cells. 57 (1999) 21–30. https://doi.org/10.1016/S0927-0248(98)00162-7.

[21] D. Vernardou, H. Drosos, E. Spanakis, E. Koudoumas, N. Katsarakis, M.E. Pemble, Electrochemical properties of amorphous WO_3 coatings grown on polycarbonate by aerosol-assisted CVD, Electrochim. Acta. 65 (2012) 185–189. https://doi.org/10.1016/j.electacta.2012.01.035.

[22] M. Pourbaix, Atlas of Electrochemical Equilibria in Aqueous Solutions, National Association of Corrosion Engineers, 1974.

[23] Z. Liu, T. Yamazaki, Y. Shen, D. Meng, T. Kikuta, N. Nakatani, T. Kawabata, Dealloying derived synthesis of W nanopetal films and their transformation into WO_3, J. Phys. Chem. C. 112 (2008) 1391–1395. https://doi.org/10.1021/jp709659r.

[24] C. Xu, Y. Liu, C. Zhou, L. Wang, H. Geng, Y. Ding, An in situ dealloying and oxidation route to Co_3O_4 nanosheets and their ambient-temperature CO oxidation activity, ChemCatChem. 3 (2011) 399–407. https://doi.org/10.1002/cctc.201000275.

[25] C. Xu, R. Wang, Y. Zhang, Y. Ding, A general corrosion route to nanostructured metal oxides, Nanoscale. 2 (2010) 906–909. https://doi.org/10.1039/b9nr00351g.

[26] J. Zhang, Y. Ling, W. Gao, S. Wang, J. Li, Enhanced photoelectrochemical water splitting on novel nanoflake WO3 electrodes by dealloying of amorphous Fe–W alloys, J. Mater. Chem.

A. 1 (2013) 10677–10685. https://doi.org/10.1039/c3ta12273e.

[27] X. Wang, S. Li, Y. Ma, H. Yu, J. Yu, $H_2WO_4 \cdot H_2O$/Ag/AgCl composite nanoplates: A plasmonic Z-scheme visible-light photocatalyst, J. Phys. Chem. C. 115 (2011) 14648–14655. https://doi.org/10.1021/jp2037476.

[28] P. Wang, B. Huang, X. Zhang, X. Qin, Y. Dai, H. Jin, J. Wei, M.H. Whangbo, Composite semiconductor $H_2WO_4 \cdot H_2O$/AgCl as an efficient and stable photocatalyst under visible light, Chem. Eur. J. 14 (2008) 10543–10546. https://doi.org/10.1002/chem.200801733.

[29] C. Balázsi, M. Farkas-Jahnke, I. Kotsis, L. Petrás, J. Pfeifer, The observation of cubic tungsten trioxide at high-temperature dehydration of tungstic acid hydrate, Solid State Ionics. 141–142 (2001) 411–416. https://doi.org/10.1016/S0167-2738(01)00806-2.

[30] G. Xin, W. Guo, T. Ma, Effect of annealing temperature on the photocatalytic activity of WO_3 for O_2 evolution, Appl. Surf. Sci. 256 (2009) 165–169. https://doi.org/10.1016/j.apsusc.2009.07.102.

[31] S. Zhang, H. Li, Z. Yang, Controllable synthesis of WO_3 with different crystalline phases and its applications on methylene blue removal from aqueous solution, J. Alloys Compd. 722 (2017) 555–563. https://doi.org/10.1016/j.jallcom.2017.06.095.

[32] J.Z. Ou, R.A. Rani, S. Balendhran, A.S. Zoolfakar, M.R. Field, S. Zhuiykov, A.P. O'Mullane, K. Kalantar-Zadeh, Anodic formation of a thick three-dimensional nanoporous WO_3 film and its photocatalytic property, Electrochem. Commun. 27 (2013) 128–132. https://doi.org/10.1016/j.elecom.2012.11.009.

[33] W. Morales, M. Cason, O. Aina, N.R. de Tacconi, K. Rajeshwar, Combustion synthesis and characterization of nanocrystalline WO3, J. Am. Chem. Soc. 130 (2008) 6318–6319. https://doi.org/10.1021/ja8012402.

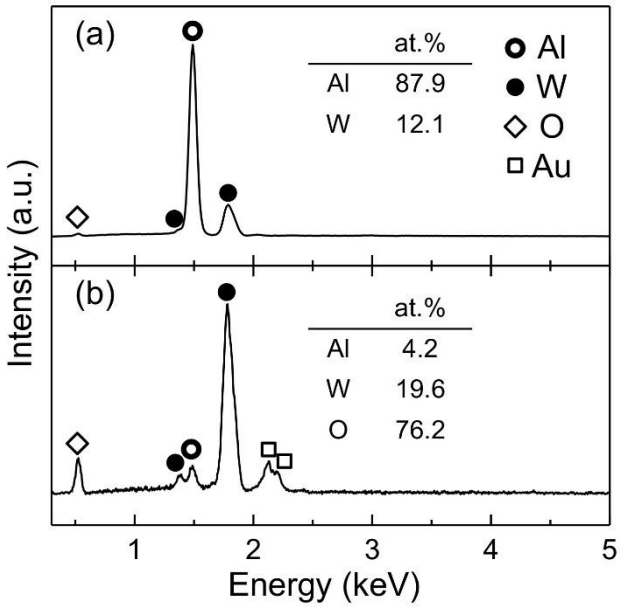

Fig. 5–1 EDX spectra of (a) as-deposited Al–W alloy film and (b) Al–W alloy film immersed in aq. HNO_3 for 15 h. The Au in (b) is due to the sputtered Au coating added to prevent charging effects.

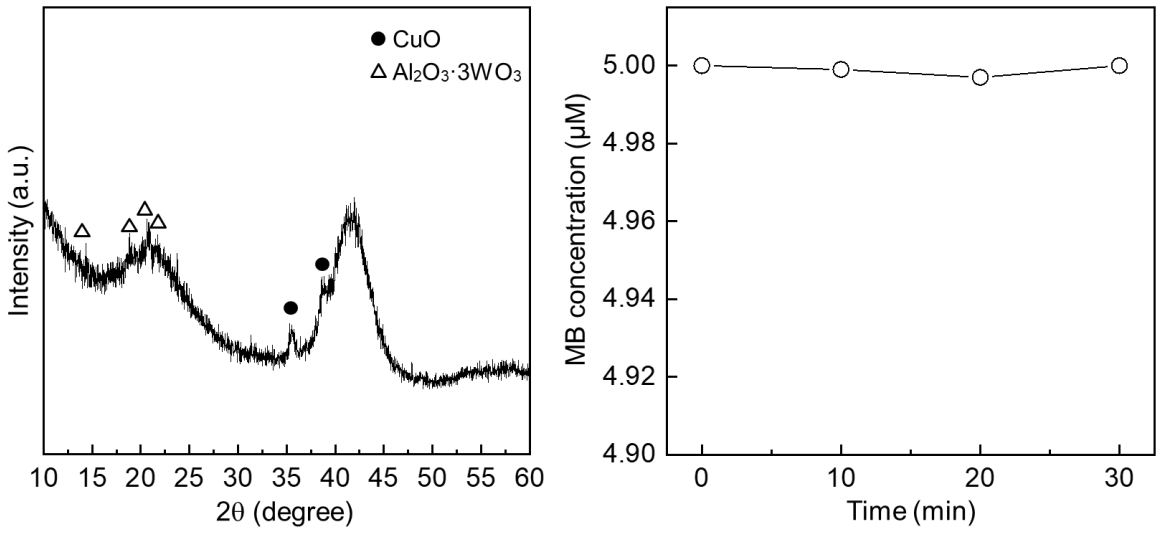

Fig. 5–2 (a) XRD pattern of the Al–W alloy film after heat treatment at 350 °C for 10 h. The diffraction pattern of CuO is derived from the oxidation layer of the Cu substrate outside the electrodeposition area. (b) Concentration of MB in aqueous solution in contact with the Al–W alloy film after heat treatment at 350 °C under visible light illumination.

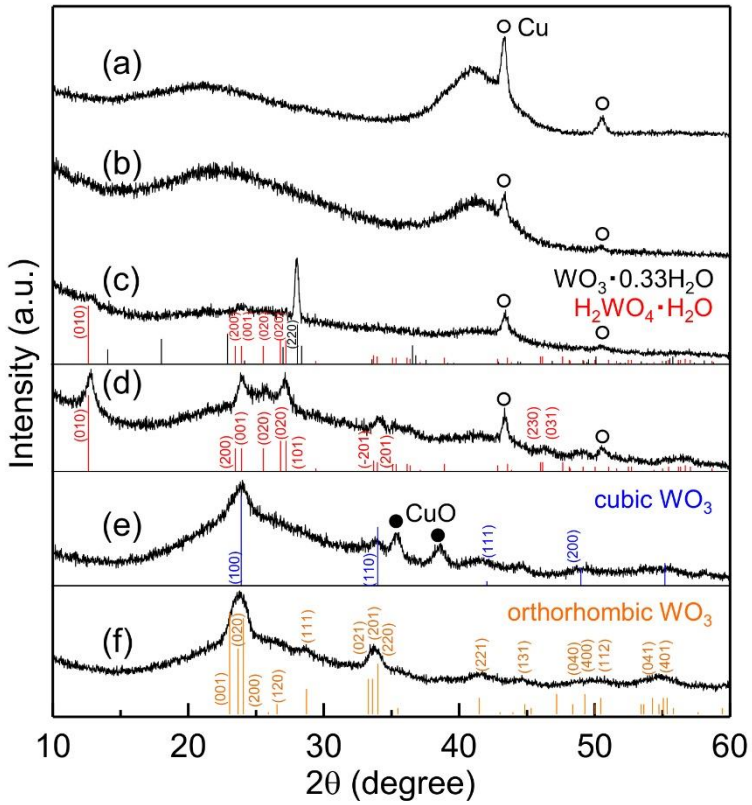

Fig. 5–3 XRD patterns of (a) as-deposited Al–W alloy films and the films after immersion in aq. HNO_3 for (b) 9 h, (c) 12 h, and (d) 15 h. XRD patterns of the films after heat treatment at (e) 300 °C and (f) 350 °C. The diffraction patterns for Cu and CuO are derived from the Cu substrate outside the electrodeposition area and its oxidation layer. The reported peak positions for $WO_3 \cdot 0.33H_2O$ (JCPDS: 01-087-1203, *Fmm2*, $Z = 12$; $a = 0.73447$ nm, $b = 1.25470$ nm, $c = 0.77367$ nm), $H_2WO_4 \cdot H_2O$ (JCPDS: 18-1420, *P2/m*, $Z = 2$; $a = 0.75000$ nm, $b = 0.69400$ nm, $c = 0.37000$ nm, $\beta = 90.5000°$), cubic WO_3 (JCPDS: 41-0905, $Pm\bar{3}m$, $Z = 1$, $a = b = c = 0.37140$ nm), and orthorhombic WO_3 (JCPDS: 20-1324, *Pcnb*, $Z = 4$, $a = 0.73840$ nm, $b = 0.75120$ nm, $c = 0.38460$ nm) are also shown.

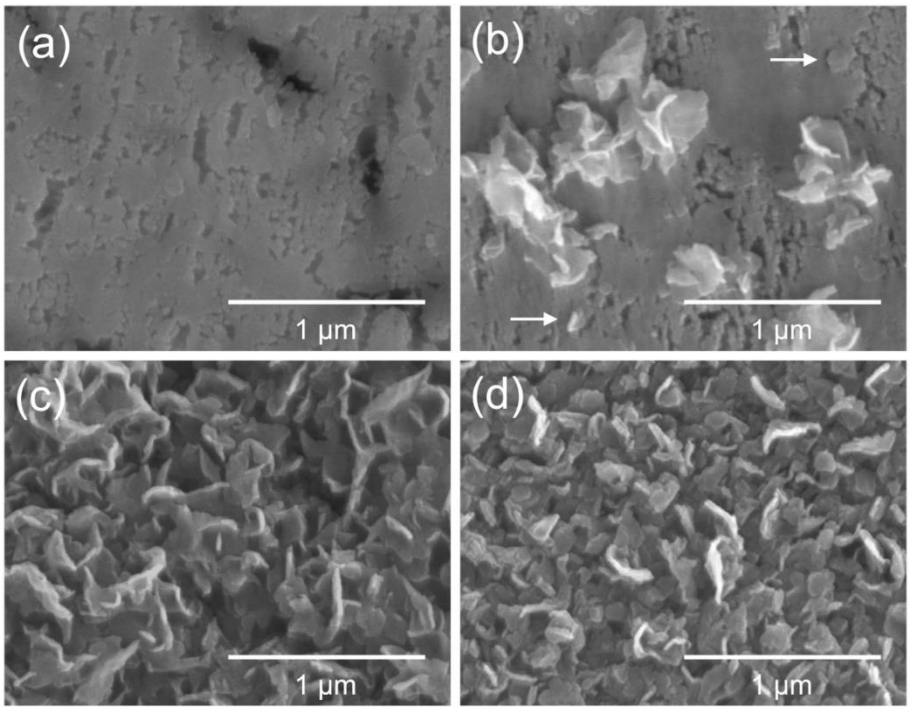

Fig. 5–4 Surface SEM images of Al–W alloy films after selective dissolution for (a) 9 h, (b) 12 h, (c) 15 h, and (d) 24 h. The arrows in (b) indicate exfoliation of the film along the cracks with one side remaining attached to the film surface.

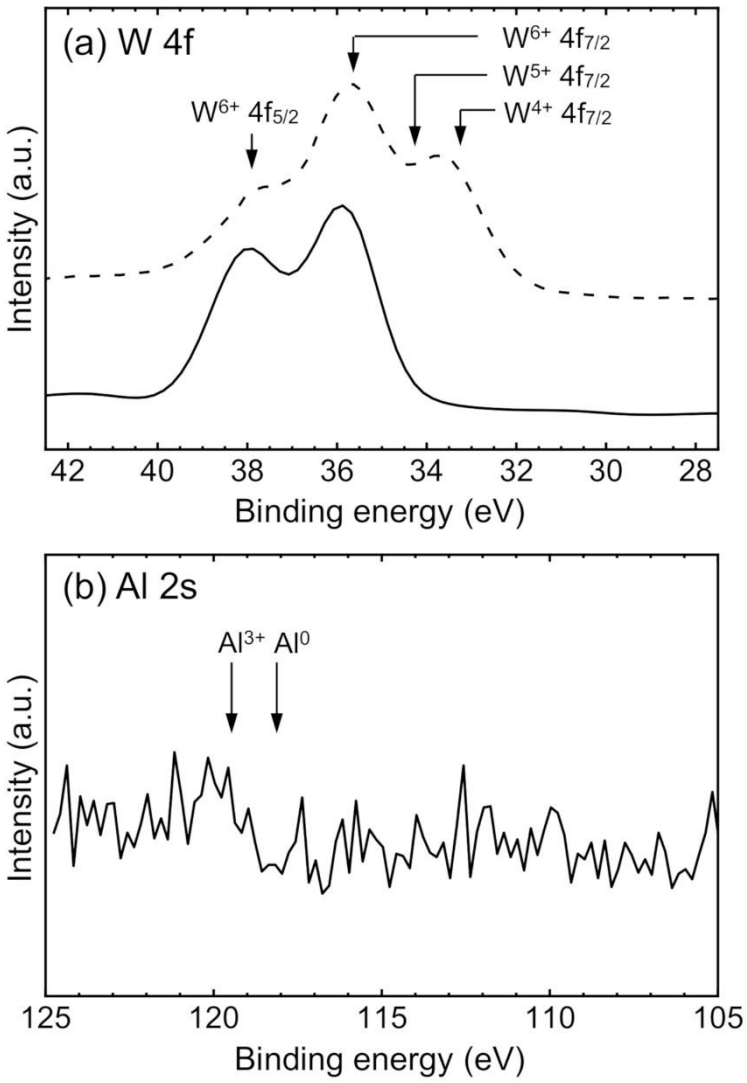

Fig. 5–5 (a) W 4f XPS spectra of Al–W alloy films after selective dissolution for 15 h (dashed line) and after selective dissolution and heat treatment at 350 °C (solid line). (b) Al 2s XPS spectra of an Al–W alloy film after selective dissolution and heat treatment at 350 °C. The binding energies of W^{4+}, W^{5+}, W^{6+}, Al^{0}, and Al^{3+} are denoted by arrows.

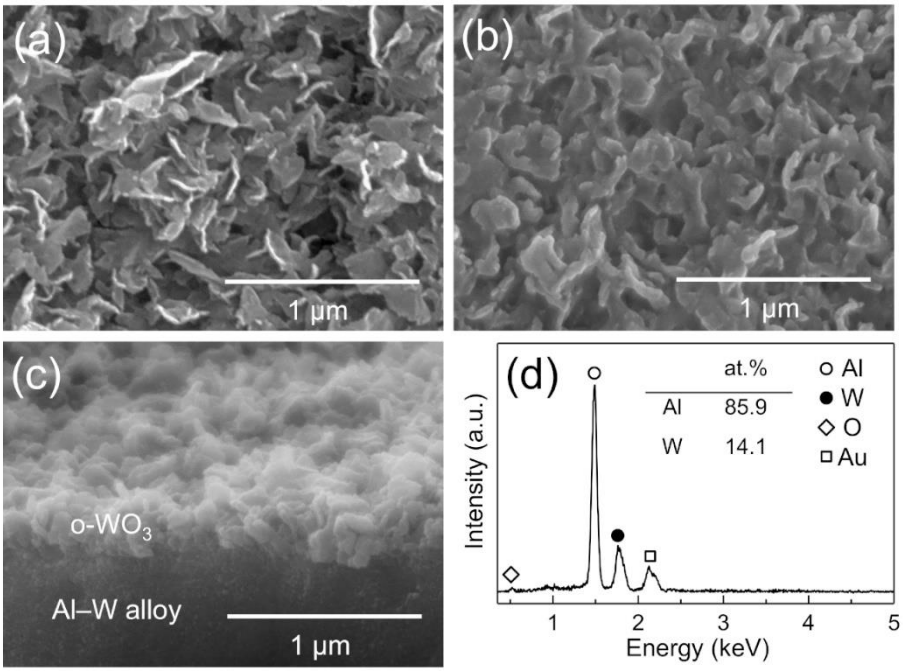

Fig. 5–6 Surface and cross-sectional SEM images of the Al–W alloy films after selective dissolution and heat treatment at (a) 300 °C and (b, c) 350 °C. (d) EDX spectrum of the Al–W underlayer.

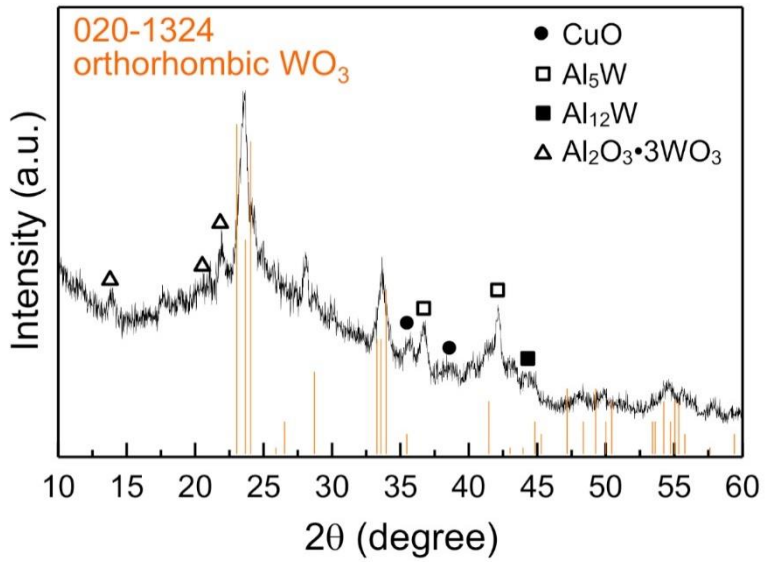

Fig. 5–7 XRD pattern of an Al–W alloy film after selective dissolution for 15 h and heat treatment at 400 °C. The diffraction pattern of aluminum tungsten oxide ($Al_2O_3 \cdot 3WO_3$) is attributable to oxidation of the Al–W alloy underlayer.

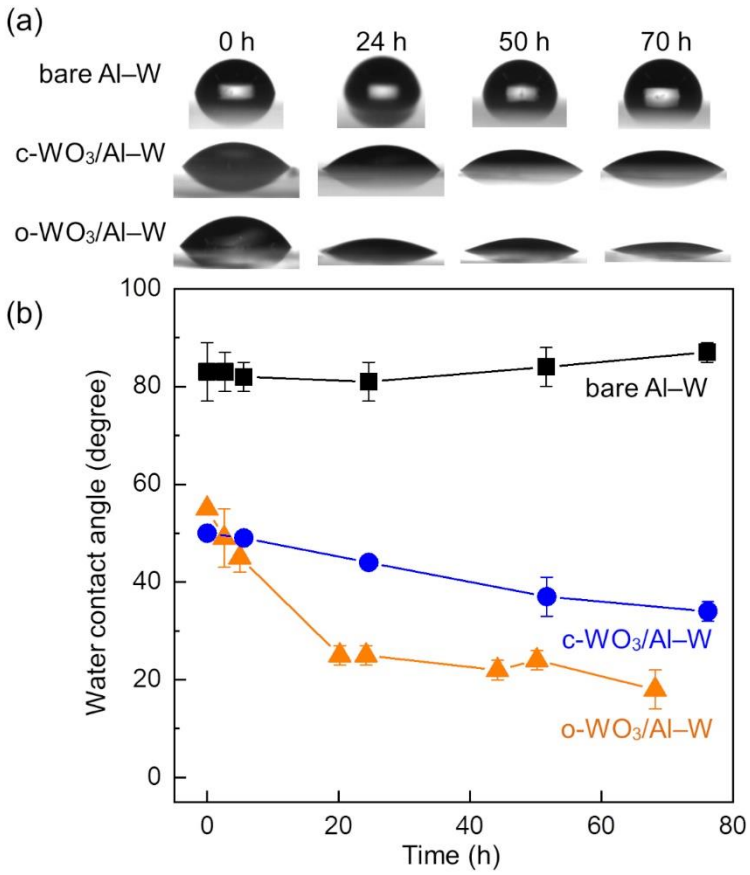

Fig. 5–8 (a) Shapes of water droplets and (b) water contact angles on bare Al–W, c-WO_3/Al–W, and o-WO_3/Al–W alloy films under visible light illumination.

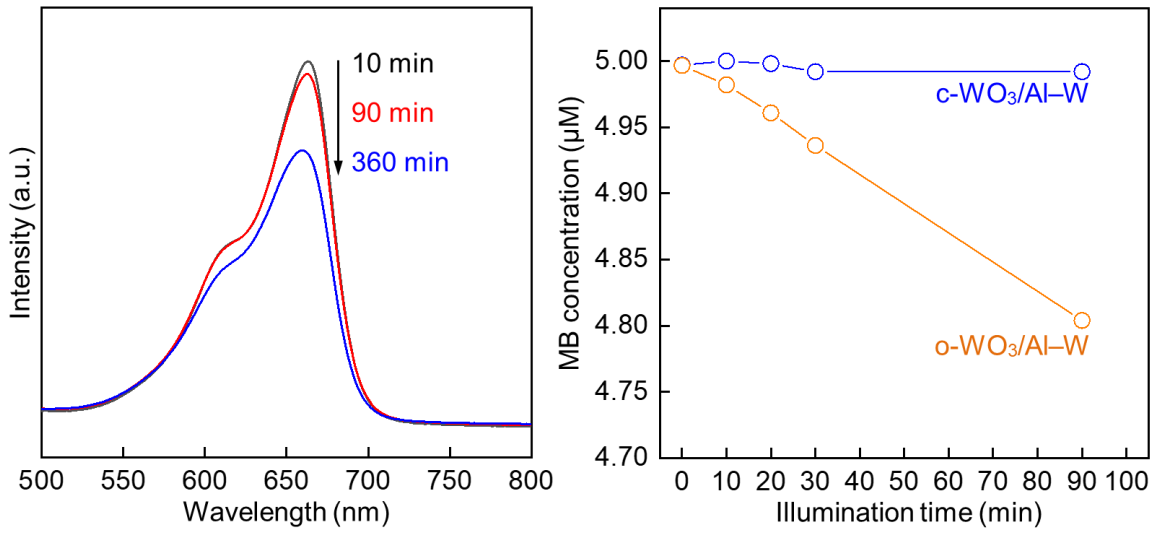

Fig. 5–9 (a) Absorption spectra of a MB aqueous solution in contact with the o-WO_3/Al–W alloy film under visible light illumination. (b) Concentration of MB in aqueous solutions in contact with c-WO_3/Al–W and o-WO_3/Al–W alloy films under visible light illumination.

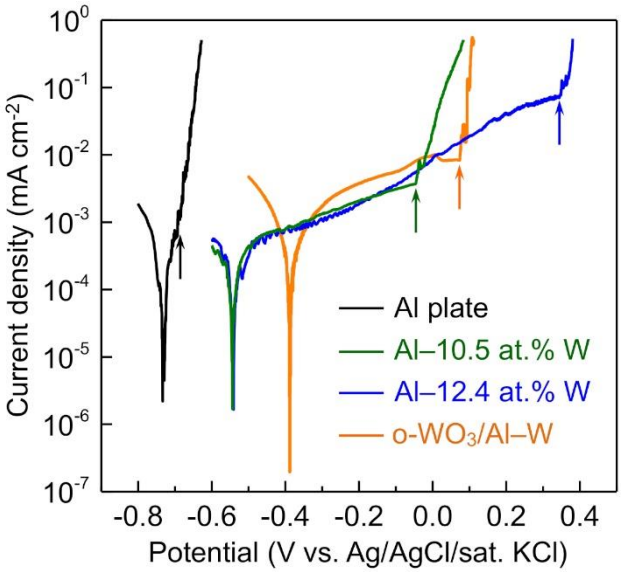

Fig. 5–10 Polarization curves for an o-WO_3/Al–W alloy film, bare Al–W alloy films with 12.4 and 10.5 at.% W, and an Al plate in 3.5 wt.% aq. NaCl solution. The arrows indicate the pitting potential in each curve.

Chapter 6

Iron(III) chloride and acetamide eutectic for the electrodeposition of iron and iron based alloys

6.1. Introduction

The electrodeposition of iron alloys is a significant research topic, owing to the potential applications such as corrosion/wear-resistant coatings [1], magnetic thin films [2–4], and catalyst electrodes [5]. Although aqueous electrolytes have been mostly used for electrodeposition, vigorous hydrogen evolution on the cathode can lead to hydrogen embrittlement and precipitation of metal hydroxides [4]. In addition, less noble elements such as aluminum and silicon cannot be co-deposited from aqueous electrolytes due to the limited electrochemical window [2].

To overcome the limitations of aqueous solutions, non-aqueous systems such as molten salts and ionic liquids have gained significant research attention [6–10]. Ionic liquids have wider potential windows and have been used to study alloy deposition. The electrochemical behavior of iron complexes in imidazolium- and pyrrolidinium-based ionic liquids, and electrodeposition of metallic Fe was demonstrated in some liquids [2,11–14]. Many ionic liquids are, however, not viable on a practical scale.

Deep Eutectic Solvents (DES) which are mixtures of quaternary ammonium salt with a metal halide or a hydrogen bond donor have been developed as alternatives to ionic liquids [15,16]. The low cost of constituting materials and easy synthesis make DESs suitable to large scale electrochemical applications. Several researchers have studied electrodeposition of Fe and Fe alloys using DESs that include ethylene glycol–choline chloride [3,4,17–19] and urea–choline chloride mixtures [20]. In these systems, Fe species were added to a relatively low concentration and hydrated Fe salts were used in some systems. This can make it difficult to avoid low deposition rates and precipitation of metal hydroxides. Fe-based DESs with anhydrous Fe species could be of interest for Fe electrodeposition,

because the high concentration of anhydrous species allows for fast deposition with a high purity. Mixtures of amide (urea and acetamide) or alcohol (ethylene glycol and hexanediol) with some metal halides such as $ZnCl_2$ and $AlCl_3$ are known to form DESs [16,21–23]. These systems are ionic because the metal salt disproportionates into an anionic and cationic species i.e.

$$2\,AlCl_3 + \text{urea} \rightarrow [AlCl_2\cdot\text{urea}]^+ + [AlCl_4]^-$$

In the present study, mixtures of $FeCl_3$–acetamide were investigated and their physicochemical properties such as melting point, viscosity and electrical conductivity were characterized. Chemical speciation of Fe was analyzed using different spectroscopic techniques and the electrodeposition of metallic Fe and Fe–Ni alloy films with tunable composition and phase was demonstrated.

6.2. Methods

Acetamide (CH_3CONH_2, Alfa Aesar, 99%) and iron(III) chloride ($FeCl_3$, Aldrich, 98%) were used as-received. The water content in pure acetamide was measured to be 0.1 wt.% using Karl Fischer titration. The DESs were formed by adding $FeCl_3$ to molten acetamide at around 90 °C with stirring until a homogeneous brown colored liquid had formed. Melting and glass transition points were determined using a Mettler Toledo DSC1 differential scanning calorimeter (DSC). DSC measurement started at −50 °C, heated up to 120 °C at a rate of 10 °C min^{-1}. Viscosity of the mixture was measured using a Brookfield DV-E Viscometer (Brookfield Instruments, USA) fitted with a temperature probe. The electrical conductivity was measured using a Yokogawa SC72 conductivity meter (Yokogawa Electric, Japan) fitted with an inherent temperature probe (cell constant = 5.14 cm^{-1}).

UV-VIS absorption spectra of the mixture were recorded using a Mettler Toledo UV5 Bio Spectrophotometer. All the spectra were recorded at 80 °C, which was maintained by a Mettler Toledo Cuve T cuvette thermostat accessory. Since diluting the liquid may change the metal speciation, neat liquid samples were placed between two quartz plates. Raman spectra were recorded using a LabRAM HR Raman microscope (HORIBA Jobin Yvon, France). Fourier Transmission Infrared (FTIR) spectra

were recorded using an Alpha II FTIR spectrometer with a diamond attenuated total reflectance module (Bruker, USA).

Cyclic voltammetry was carried out using an IVIUMSTAT electrochemical analyzer controlled with Iviumsoft. A three-electrode system was used, consisting of a platinum working-electrode with an area of 7.85×10^{-3} cm^2, a platinum flag counter-electrode and a platinum quasi-reference electrode. Using a Pt quasi-reference electrode in DES systems is common when the liquid contains a redox couple[4]. The working electrode was polished with alumina powder and cleaned by rinsing with distilled water and acetone prior to use. All CVs were recorded at 80 °C at a scan rate of 10 mV s^{-1}. Bulk electrodeposition experiments were carried out in a 100 mL Beaker. A copper plate (2×2 cm^2) was used as a cathode to facilitate subsequent characterizations. Copper plates were cleaned with acetone and distilled water prior to use. Part of copper plates was masked to expose a defined area of 1×1 cm^2 to the electrolyte. An iridium oxide-coated titanium mesh electrode (3×3 cm^2) was used as an anode. In all the experiments the electrolyte was maintained at 80 °C. Electrodeposition was carried out until the amount of charge reached 30 C cm^{-2}, which can theoretically produce a Fe film with thickness of 7.4 μm. After electrodeposition the cathode plates were removed from the cell and washed with acetone and distilled water.

The surface morphology characterization and elemental analysis of the deposit composition were carried out using a QUANTA FEG 650 scanning electron microscope (SEM, ThermoFisher Scientific, USA) equipped with a X-Max energy dispersive X-ray spectroscopy (EDX, Oxford Instruments, UK) with an accelerating voltage of 20 keV. X-ray diffraction (XRD) patterns of deposits were recorded using a BRUKER D8 ADVANCE X-ray diffractometer with Cu Kα radiation (λ = 1.5406 Å).

Linear sweep voltammetry (LSV) of Fe and Fe–Ni alloy deposits and a commercial Ni wire was carried out in 0.1 M potassium nitrate (KNO_3) aqueous solution using a three-electrode system. The deposits were covered with a masking tape to expose a 3×3 mm^2 area and were used as a working electrode. A platinum flag electrode and an Ag/AgCl reference electrode immersed in 3 M KCl aqueous solution and separated with porous glass were used as a counter and reference electrode, respectively.

All LSVs were recorded at room temperature at a scan rate of 5 mV s^{-1}.

6.3. Results and discussion

Melting/glass transition behavior, viscosity, and electrical conductivity

Mixture of $FeCl_3$:acetamide were made in the molar ratio range 1:2 to 1:10. All these mixtures were dark brown liquids at 80 °C. The 1:4 mixture was liquid at room temperature, whereas the other ones formed orange crystals. Phase transitions were analyzed using DSC and Figure 6–1 shows a typical DSC curves of $FeCl_3$–acetamide mixtures with 1:4 and 1:10 composition. The 1:10 mixture shows a heat capacity change (baseline shift) at around −22 °C and an endothermic peak at around 66 °C. The 1:4 mixture also shows a heat capacity change at −15 °C, but at higher temperature it does not show significant change in heat capacity. The baseline shift and endothermic peak in the DSC curves are attributed to a glass transition and melting, respectively. The absence of an endothermic peak as observed in 1:4 mixture is also the case with some other ionic liquids and deep eutectic solvents and it is attributed to slow transition from a viscous or rubbery state to a liquid [24]. The eutectic composition is 1: 4, where T_g is −15 °C and no discernable T_{mp} is observed (c.f. pure $FeCl_3$ (282 °C) and acetamide (84 °C)). Mixtures of $ZnCl_2$ and $AlCl_3$ with acetamide are also known to form eutectic liquids (type 4 DESs), and their eutectic composition and melting point are compared to the present $FeCl_3$ system in Table 1 [21,22]. The eutectic composition and T_g of the $FeCl_3$ and $ZnCl_2$ mixtures are quite similar, and these mixtures have a lower eutectic composition and a higher T_g than those of $AlCl_3$ mixture. This suggests that the $FeCl_3$ and $ZnCl_2$ mixtures have a similar chemical speciation and interaction in liquid. The higher T_g of the $FeCl_3$ and $ZnCl_2$ mixtures than that of the $AlCl_3$ mixture could be attributed to the higher T_{mp} of the first two metal halides. The narrower range of eutectic composition of the $FeCl_3$ and $ZnCl_2$ mixtures could be attributed to the less strong Lewis acidity than $AlCl_3$.

The viscosity of the $FeCl_3$–acetamide mixtures with a composition of 1:4 and 1:10 is plotted as a function of temperature (Fig. 6–2a). Both of these mixtures showed higher viscosity than that of pure molten acetamide (~2 cP [25]) and the viscosity increased with increasing $FeCl_3$/acetamide ratio. This

indicates $FeCl_3$ and acetamide molecules form a less mobile complex. Conductivity of the $FeCl_3$–acetamide mixtures is plotted as a function of temperature (Fig. 6–2b). The 1:10 mixture showed much higher conductivity than that of pure molten acetamide (31 μS cm^{-1} at 90 °C [26]) but higher concentration of $FeCl_3$ ($FeCl_3$:acetamide ratio of 1:4) lowered conductivity rather than increasing it. This implies the formation of complexes with lower ionic mobility in the 1:4 mixture. The $FeCl_3$ mixtures showed relatively high conductivity than the mixtures of $ZnCl_2$ and $AlCl_3$ with acetamide as compared in Table 2 [21,27].

Change in viscosity (η) and conductivity (σ) as a function of temperature (T) is described by the following Arrhenius equations 1 and 2;

$$\ln\eta = \ln\eta_0 + E_\eta/RT \quad (1)$$

$$\ln\sigma = \ln\sigma_0 - E_\sigma/RT \quad (2)$$

where η_0 and σ_0 are a constant, and E_η and E_σ are the activation energy for viscous flow and conductivity. E_η and E_σ corresponds to the activation energy for viscous flow and conductivity. The ln η and ln σ values for $FeCl_3$ mixtures are plotted as a function of $1000/T$ (Fig. 6–3c and d), and it is found that both 1:4 and 1:10 mixtures follow a good linear correlation in each plot. The least square fitting gives E_η and E_σ values shown in Table 2. The $FeCl_3$ mixtures have higher E_η and E_σ compared to those of the $ZnCl_2$ and $AlCl_3$ mixtures [21,27]. In $FeCl_3$ mixtures, E_η and E_σ increased with increasing $FeCl_3$ ratio. This makes a clear contrast with $AlCl_3$–acetamide mixtures with a composition range of 1:1–1:2. The different behavior of E_η and E_σ in $FeCl_3$ and $AlCl_3$ mixtures will be explained by the change in chemical interaction in the following section.

Chemical speciation of Fe

UV-VIS, Raman, FT-IR spectra were obtained to investigate the chemical speciation of Fe species (Fig. 6–3a–c). UV-VIS spectra (Fig. 6–4a) show three peaks located at 242, 319 and 367 nm and a faint shoulder peak located at around 270 nm. These peaks were also observed in aqueous $FeCl_3$ solution with concentrated Cl^-, and indicate the presence of $FeCl_4^-$ [28]. Raman spectra (Fig. 6–3b)

show that distinct peaks of pure acetamide located at 879, 1151 and 1360 cm^{-1} [29] are significantly weakened in $FeCl_3$–acetamide mixtures, indicating that acetamide molecules formed a complex with $FeCl_3$. The spectra of $FeCl_3$–acetamide mixtures also have a sharp peak at 334 cm^{-1} and a broad peak at around 302–305 cm^{-1}, both of which were not observed in pure acetamide. The peak at 334 cm^{-1} was also observed in $FeCl_3$–C_4mimCl ionic liquid with a composition of $FeCl_3$:C_4mimCl=1:1.5, and was attributed to $FeCl_4^-$ [30,31]. In Raman spectra of aqueous $FeCl_3$ solution, a broad peak was observed at around 315 cm^{-1} and it was attributed to the most abundant species, $FeCl_2(H_2O)_4^+$ [32]. The broad peak at around 302–305 cm^{-1} could be attributed to a similar Fe species such as $FeCl_2[CH_3CONH_2]_n^+$(Fig. 6–3d). FTIR spectra (Fig. 6–3c) show the N-H (3300 and 3150 cm^{-1}), C-H (2816 cm^{-1}), C=O (1674 cm^{-1}), and C-N (1392 cm^{-1}) vibration peaks of acetamide molecules [33]. In the $FeCl_3$–acetamide mixtures, the N-H peak shifted to higher wavenumbers and C-H, C=O and C-N peaks shifted to lower wavenumbers. It is also noted that in the $FeCl_3$–acetamide mixtures the intensity of N-H, C=O, C-N peaks increased compared to pure acetamide and the increment is most significant for the C=O peak. These variations of FTIR spectra were also observed in $ZnCl_2$–acetamide mixtures [23] and the authors suggested the formation of metal–oxygen bond between Zn^{2+} and C=O in acetamide. The formation of similar complex between Fe species and acetamide could be expected in the present $FeCl_3$–acetamide system. Combining all the information of spectra described above, the Fe species are thought to be $FeCl_4^-$ and $FeCl_2[CH_3CONH_2]_n^+$ that are formed by disproportionation of $FeCl_3$ (formula 3). $ZnCl_2$ and $AlCl_3$ are also known to cause similar disproportionation. A possible coordination number n in $FeCl_2[CH_3CONH_2]_n^+$ is 4, which forms an octahedral complex (Fig. 6–3d).

$$MCl_X + nCH_3CONH_2 = MCl_{X+1}^- + MCl_{X-1}[CH_3CONH_2]_n^+ (M = Fe, Zn, and Al) \quad (3)$$

The viscosity and conductivity of $FeCl_3$–acetamide mixtures are better understood in terms of chemical speciation. The increase in viscosity and decrease in conductivity with increasing $FeCl_3$ ratio could be attributed to the increasing amount of the less mobile complex, $FeCl_2[CH_3CONH_2]_n^+$.

Increasing E_η and E_σ with increasing $FeCl_3$ ratio could also be attributed to the strengthening of the ionic interaction due to the increasing ionic species ($FeCl_2[CH_3CONH_2]_n^+$ and $FeCl_4^-$) and the decreasing free acetamide molecules. By contrast, in $AlCl_3$ mixtures with $AlCl_3$/acetamide ratio of >1, E_η and E_σ remain almost constant with increasing $AlCl_3$ ratio. When $AlCl_3$/acetamide ratio is >1, there exists an equilibrium between $AlCl_2[CH_3CONH_2]_n^+$, $AlCl_4^-$ and $Al_2Cl_7^-$ ions and there is no free acetamide (formula 3 and 4) [27]. Therefore, the change in ionic interaction could be less significant than the $FeCl_3$ mixture.

$$AlCl_4^- + AlCl_3 = Al_2Cl_7^- \qquad (AlCl_3/\text{acetamide}>1)\ (4)$$

Cyclic Voltammetry

Cyclic Voltammetry on a Pt working electrode was carried out in $FeCl_3$–acetamide mixture with 1:10 composition (Fig. 6–4a and b) at 80 °C and scan rate of 10 mV s^{-1}. The working electrode potential was measured with a Pt quasi-reference electrode. CV was also carried out in $NiCl_2$–acetamide (Fig. 6–4c) and $FeCl_3$– $NiCl_2$–acetamide (Fig. 6–4d) mixtures, with an aim of examining co-deposition of Fe and Ni.

In the 1:10 $FeCl_3$–acetamide mixture, two reduction waves were observed at around 0 V and −1.5 V. After switching to anodic sweep at –2 V, two oxidation waves located at −0.65 V and −0.05 V and one oxidation wave at +0.5 V were observed. The reversible redox couple around 0 V was also observed when the potential sweep was switched to anodic direction at –1.2 V (Fig. 6–4b), and it is attributed to Fe(III)/Fe(II) redox couple. The cathodic wave at −1.5 V and anodic wave at −0.65 V are attributed to the reduction of Fe(II) to Fe(0) and the stripping of Fe(0), respectively. The difference between the potentials of Fe(III)/Fe(II) and Fe(II)/Fe(0) is around 1.3 V, which is similar to those observed in chlorine chloride–urea–$FeCl_3$ deep eutectic solvents [20,34]. The oxidation current at +0.5 V could be attributed to decomposition of acetamide. When the potential is swept to a more negative value such

as −3 V, irregular current waves were observed and they could also be attributed to decomposition of acetamide.

$NiCl_2$ dissolved quickly into molten acetamide and formed a mixture with slightly lower melting point than pure acetamide. CV in $NiCl_2$–acetamide (Fig. 6–4c) shows the Ni deposition and stripping at around −1 V and −0.1 V, respectively. In the ternary $FeCl_3$– $NiCl_2$–acetamide mixtures (Fig. 6–4d), lower reduction current density was observed, probably because of the increased viscosity. The onset potentials of Fe deposition and stripping shifted to more positive potentials and the stripping wave is much smaller than the deposition wave. The shift and decrease of the stripping wave could be attributed to the formation of a nobler Fe–Ni alloy phase and the passivation of the deposit, respectively.

Electrodeposition of Fe and Fe–Ni

Electrodeposition of Fe and Fe–Ni alloy onto a Cu substrate was examined in 1:10 $FeCl_3$–acetamide, 1:0.1:10 $FeCl_3$–$NiCl_2$–acetamide, and 1:1:10 $FeCl_3$–$NiCl_2$–acetamide mixtures) at 80 °C. The applied current density was 100 mA cm^{-2} for the first two mixtures and 30 mA cm^{-2} for the last mixture, because in the last mixture a higher current density caused decomposition of acetamide. The amount of charge passed was 30 C cm^{-2}, which can theoretically produce a Fe film with thickness of 7.4 μm.

Electrodeposition in each mixture produced metallic gray films, and SEM images show that all the films are dense (Fig. 6–5a-1–a-3). The 1:10 $FeCl_3$–acetamide and 1:0.1:10 $FeCl_3$–$NiCl_2$–acetamide mixtures produced a similar morphology composed of round grains which are a few micrometers in scale. The 1:1:10 $FeCl_3$–$NiCl_2$–acetamide mixture, on the other hand, produced much smaller grains. EDX spectra (Fig. 6–5b) show that these three deposits are Fe, $Fe_{72}Ni_{28}$ and $Fe_{12}Ni_{88}$ alloys. Traces of oxygen were detected in all deposits and a trace of chloride was detected only in the 1:1:10 $FeCl_3$–$NiCl_2$–acetamide mixture. The presence of O is attributed to surface oxidation in ambient air. Cl seems to be trapped during electrodeposition, probably because the 1:1:10 $FeCl_3$–$NiCl_2$–acetamide mixture is relatively more viscous. Cl trapping in electrodeposited film was also observed in $AlCl_3$–dimethyl

sulfone and $AlCl_3$–glyme baths [35,36].

XRD patterns were obtained to analyze the phase of the deposits (Fig. 6–5c). The deposits obtained from 1:10 $FeCl_3$–acetamide (Fe) and 1:0.1:10 $FeCl_3$–$NiCl_2$–acetamide ($Fe_{72}Ni_{28}$) mixtures showed peaks of bcc Fe (JCPDS No. 006-0696, a=b=c=2.8664Å). On the other hand, the one obtained from 1:1:10 $FeCl_3$–$NiCl_2$–acetamide mixture ($Fe_{12}Ni_{88}$) showed peaks of fcc Ni (JCPDS No. 004-0850, a=b=c=3.5238Å). It is expected that $Fe_{72}Ni_{28}$ and $Fe_{12}Ni_{88}$ deposits are substitutional solid solutions, but XRD peak shift is not evident because the atomic radii of Fe and Ni are almost the same.

Linear sweep voltammetry (LSV) of the deposits was carried out to characterize their oxidation behavior (Fig. 6–6). LSV of commercial Ni wire was also obtained as a comparison. The open circuit potentials are in the order of Fe<$Fe_{72}Ni_{28}$<$Fe_{12}Ni_{88}$<Ni and vice versa for the oxidation current density. This indicates that the $Fe_{72}Ni_{28}$ and $Fe_{12}Ni_{88}$ deposits are composed of a Fe–Ni alloy phase which is nobler than pure Fe.

6.4. Conclusion

The electrodeposition of iron and iron-nickel alloys has been demonstrated using a novel ferric chloride-acetamide eutectic. The liquid contains both anionic and cation iron containing species and was found to have higher conductivity and lower viscosity than corresponding eutectics with aluminum chloride and zinc chloride. Dense iron and iron-nickel alloys with tunable composition were obtained and displayed improved corrosion resistance with increasing nickel content.

References

[1] N. Tsyntsaru, H. Cesiulis, M. Donten, J. Sort, E. Pellicer, E.J. Podlaha-Murphy, Modern trends in tungsten alloys electrodeposition with iron group metals, Surf. Eng. Appl. Electrochem. 48 (2013) 491–520. https://doi.org/10.3103/S1068375512060038.

[2] P. Giridhar, B. Weidenfeller, S.Z. El Abedin, F. Endres, Electrodeposition of iron and iron-aluminium alloys in an ionic liquid and their magnetic properties, Phys. Chem. Chem. Phys. 16 (2014) 9317–9326. https://doi.org/10.1039/c4cp00613e.

[3] T. Yanai, K. Shiraishi, Y. Watanabe, M. Nakano, T. Ohgai, Electroplated Fe – Ni Films Prepared From Deep Eutectic Solvents, IEEE Trans. Magn. 50 (2014) 1–4. https://doi.org/10.1109/TMAG.2014.2323572.

[4] G. Panzeri, A. Accogli, E. Gibertini, C. Rinaldi, L. Nobili, L. Magagnin, Electrodeposition of high-purity nanostructured iron films from Fe(II) and Fe(III) non-aqueous solutions based on ethylene glycol, Electrochim. Acta. 271 (2018) 576–581. https://doi.org/10.1016/j.electacta.2018.03.174.

[5] N.-C. Lo, P.-C. Chung, W.-J. Chuang, S.C.N. Hsu, I.-W. Sun, P.-Y. Chen, Voltammetric Study and Electrodeposition of Ni(II)/Fe(II) in the Ionic Liquid 1-Butyl-1-Methylpyrrolidinium Dicyanamide, J. Electrochem. Soc. 163 (2016) D9–D16. https://doi.org/10.1149/2.0221602jes.

[6] F. Endres, D. MacFarlane, A. Abbott, eds., Electrodeposition from ionic liquids, Wiley, Weinheim, 2008.

[7] T. Tsuda, G.R. Stafford, C.L. Hussey, Review—Electrochemical Surface Finishing and Energy Storage Technology with Room-Temperature Haloaluminate Ionic Liquids and Mixtures, J. Electrochem. Soc. 164 (2017) H5007–H5017. https://doi.org/10.1149/2.0021708jes.

[8] Y. Gu, J. Liu, S. Qu, Y. Deng, X. Han, W. Hu, Electrodeposition of alloys and compounds from high-temperature molten salts, J. Alloys Compd. 690 (2017) 228–238.

https://doi.org/10.1016/j.jallcom.2016.08.104.

[9] F. Liu, Y. Deng, X. Han, W. Hu, C. Zhong, Electrodeposition of metals and alloys from ionic liquids, J. Alloys Compd. 654 (2016) 163–170. https://doi.org/10.1016/j.jallcom.2015.09.137.

[10] W. Simka, D. Puszczyk, G. Nawrat, Electrodeposition of metals from non-aqueous solutions, Electrochim. Acta. 54 (2009) 5307–5319. https://doi.org/10.1016/j.electacta.2009.04.028.

[11] P. Giridhar, B. Weidenfeller, S.Z. El Abedin, F. Endres, Electrodeposition and magnetic characterization of iron and iron-silicon alloys from the ionic liquid 1-butyl-1-methylpyrrolidinium trifluoromethylsulfonate, ChemPhysChem. 15 (2014) 3515–3522. https://doi.org/10.1002/cphc.201402406.

[12] Z. Guo, T. Zhang, M. Khan, S. Gao, T. Liu, J. Yu, Electrochemical behavior of iron-based imidazolium chloride ionic liquids, Electrochim. Acta. 142 (2014) 132–143. https://doi.org/10.1016/j.electacta.2014.07.110.

[13] Y. Zhu, Y. Katayama, T. Miura, Electrochemistry of Fe(II)/Fe in a Hydrophobic Amide-Type Ionic Liquid, J. Electrochem. Soc. 159 (2012) D699–D704. https://doi.org/10.1149/2.023212jes.

[14] P. Giridhar, S. Zein El Abedin, A. Bund, A. Ispas, F. Endres, Electrodeposition of Niobium from 1-Butyl-1-Methylpyrrolidinium bis(trifluoromethylsulfonyl)amide Ionic Liquid, Electrochim. Acta. 129 (2014) 312–317. https://doi.org/10.1016/j.electacta.2014.02.099.

[15] A.P. Abbott, G. Capper, D.L. Davies, R.K. Rasheed, V. Tambyrajah, Novel solvent properties of choline chloride/urea mixtures, Chem. Commun. (2003) 70–71. https://doi.org/10.1039/b210714g.

[16] E.L. Smith, A.P. Abbott, K.S. Ryder, Deep Eutectic Solvents (DESs) and Their Applications, Chem. Rev. 114 (2014) 11060–11082. https://doi.org/10.1021/cr300162p.

[17] G. Saravanan, S. Mohan, Electrodeposition of Fe-Ni-Cr alloy from Deep Eutectic System containing Choline chloride and Ethylene Glycol, Int. J. Electrochem. Sci. 6 (2011) 1468–1478.

[18] M.A. Miller, J.S. Wainright, R.F. Savinell, Iron Electrodeposition in a Deep Eutectic Solvent for Flow Batteries, J. Electrochem. Soc. 164 (2017) A796–A803. https://doi.org/10.1149/2.1141704jes.

[19] T. Yanai, K. Shiraishi, T. Akiyoshi, K. Azuma, Y. Watanabe, T. Ohgai, T. Morimura, M. Nakano, H. Fukunaga, Electroplated Fe-Co-Ni films prepared from deep-eutectic-solvent-based plating baths, AIP Adv. 6 (2016) 055917. https://doi.org/10.1063/1.4943533.

[20] R. Böck, S.E. Wulf, Electrodeposition of iron films from an ionic liquid (ChCl/urea/$FeCl_3$ deep eutectic mixtures), Trans. Inst. Met. Finish. 87 (2009) 28–32. https://doi.org/10.1179/174591908X379601.

[21] A.P. Abbott, J.C. Barron, K.S. Ryder, D. Wilson, Eutectic-based ionic liquids with metal-containing anions and cations, Chem. - A Eur. J. 13 (2007) 6495–6501. https://doi.org/10.1002/chem.200601738.

[22] H.M.A. Abood, A.P. Abbott, A.D. Ballantyne, K.S. Ryder, Do all ionic liquids need organic cations? Characterisation of $[AlCl_2 \cdot nAmide]^+$ $AlCl_4^-$ and comparison with imidazolium based systems, Chem. Commun. 47 (2011) 3523–3525. https://doi.org/10.1039/c0cc04989a.

[23] Y. Wang, Z. Niu, Q. Zheng, C. Zhang, J. Ye, G. Dai, Y. Zhao, X. Zhang, Zn-based eutectic mixture as anolyte for hybrid redox flow batteries, Sci. Rep. 8 (2018) 8–15. https://doi.org/10.1038/s41598-018-24059-x.

[24] M.A. Sedghamiz, S. Raeissi, Physical properties of deep eutectic solvents formed by the sodium halide salts and ethylene glycol, and their mixtures with water, J. Mol. Liq. 269 (2018) 694–702. https://doi.org/10.1016/j.molliq.2018.08.045.

[25] K. Mukherjee, A. Das, S. Choudhury, A. Barman, R. Biswas, Dielectric Relaxations of (Acetamide + Electrolyte) Deep Eutectic Solvents in the Frequency Window, $0.2 \leq \nu/\mathrm{GHz} \leq 50$: Anion and Cation Dependence, J. Phys. Chem. B. 119 (2015) 8063–8071. https://doi.org/10.1021/acs.jpcb.5b01502.

[26] M.S. Akhter, Conductance and surface tension of ionic surfactants in molten acetamide,

Colloids Surfaces A Physicochem. Eng. Asp. 125 (1997) 109–114. https://doi.org/10.1016/S0927-7757(96)03897-6.

[27] C. Liu, W. Chen, Z. Wu, B. Gao, X. Hu, Z. Shi, Z. Wang, Density, viscosity and electrical conductivity of $AlCl_3$-amide ionic liquid analogues, J. Mol. Liq. 247 (2017) 57–63. https://doi.org/10.1016/j.molliq.2017.09.091.

[28] W. Liu, B. Etschmann, J. Brugger, L. Spiccia, G. Foran, B. McInnes, UV-Vis spectrophotometric and XAFS studies of ferric chloride complexes in hyper-saline LiCl solutions at 25-90 °C, Chem. Geol. 231 (2006) 326–349. https://doi.org/10.1016/j.chemgeo.2006.02.005.

[29] J.M. Dudik, C.R. Johnson, S.A. Asher, UV resonance Raman Studies of Acetone, Acetamide, and N-Methylacetamide: Models for the Peptide Bond, J. Phys. Chem. 89 (1985) 3805–3814. https://doi.org/10.1021/j100264a008.

[30] J.S. Avery, C.D. Burbridge, D.M.L. Goodgame, Raman spectra of tetrahalo-anions of Fe^{III}, Mn^{II}, Fe^{II}, Cu^{II} and Zn^{II}, Spectrochim. Acta. 24A (1968) 1721–1726. https://doi.org/10.1039/JI9618500079.

[31] M.S. Sitze, E.R. Schreiter, E. V. Patterson, R.G. Freeman, Ionic liquids based on $FeCl_3$ and $FeCl_2$. Raman scattering and ab initio calculations, Inorg. Chem. 40 (2001) 2298–2304. https://doi.org/10.1021/ic001042r.

[32] L. Lin, J. Husek, S. Biswas, S.M. Baumler, T. Adel, K.C. Ng, L.R. Baker, H.C. Allen, Iron(III) Speciation Observed at Aqueous and Glycerol Surfaces: Vibrational Sum Frequency and X-ray, J. Am. Chem. Soc. 141 (2019) 13525–13535. https://doi.org/10.1021/jacs.9b05231.

[33] D.H. Kerridge, The chemistry of molten acetamide and acetamide complexes, Chem. Soc. Rev. 17 (1988) 181–227. https://doi.org/10.1039/CS9881700181.

[34] M. Palomar-Pardavé, J. Mostany, R. Muñoz-Rizo, L.E. Botello, J. Aldana-González, E.M. Arce-Estrada, M.G.M. de Oca-Yemha, M.T. Ramírez-Silva, M.R. Romo, Electrochemical

study and physicochemical characterization of iron nanoparticles electrodeposited onto HOPG from Fe(III) ions dissolved in the choline chloride-urea deep eutectic solvent, J. Electroanal. Chem. 851 (2019) 113453. https://doi.org/10.1016/j.jelechem.2019.113453.

[35] M. Miyake, H. Motonami, S. Shiomi, T. Hirato, Electrodeposition of purified aluminum coatings from dimethylsulfone-AlCl3 electrolytes with trimethylamine hydrochloride, Surf. Coatings Technol. 206 (2012) 4225–4229. https://doi.org/10.1016/j.surfcoat.2012.04.027.

[36] A. Kitada, K. Nakamura, K. Fukami, K. Murase, Electrochemically active species in aluminum electrodeposition baths of AlCl3/glyme solutions, Electrochim. Acta. 211 (2016) 561–567. https://doi.org/10.1016/j.electacta.2016.05.063.

Table 6–1. Glass transition temperatures and melting points of metal chloride mixtures with acetamide at their eutectic compositions.

MCl_x	MCl_x : acetamide	T_g (°C)	T_{mp} of MCl_x (°C)
$FeCl_3$	1:4	−15	282
$ZnCl_2$	1:4	−16	293
$AlCl_3$	1:1	−63	192

Table 6–2. Viscosity, conductivity, E_η and E_σ of MCl_x (M = Fe, Zn, and Al)–acetamide mixtures. Viscosity and conductivity were referred to at 90 °C.

	MClx: acetamide	Viscosity (cP)	Conductivity (mS cm^{-1})	E_η (kJ mol^{-1})	E_σ (kJ mol^{-1})
$FeCl_3$	1:10	6.5	13.5	36	32
$FeCl_3$	1:4	9.6	11.2	89	47
$ZnCl_2$	1:4	3.7	2.4	62	28
$AlCl_3$	1:1	13.4	6.78	25.6	23.4
$AlCl_3$	1.5:1	10.9	8.12	25.5	22.2

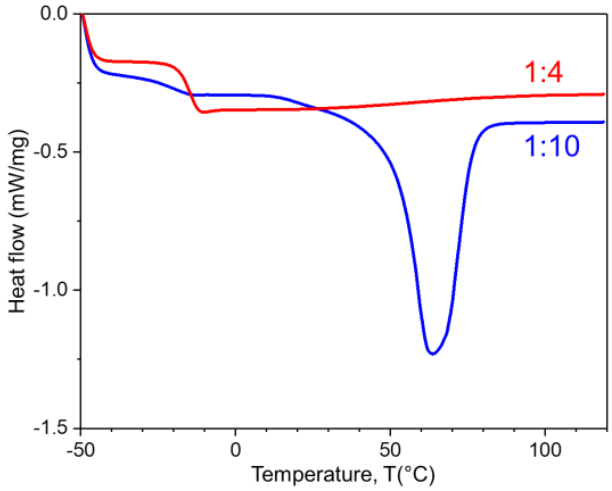

Figure 6–1. DSC curves of $FeCl_3$–acetamide mixtures with 1:10 and 1:4 molar ratio.

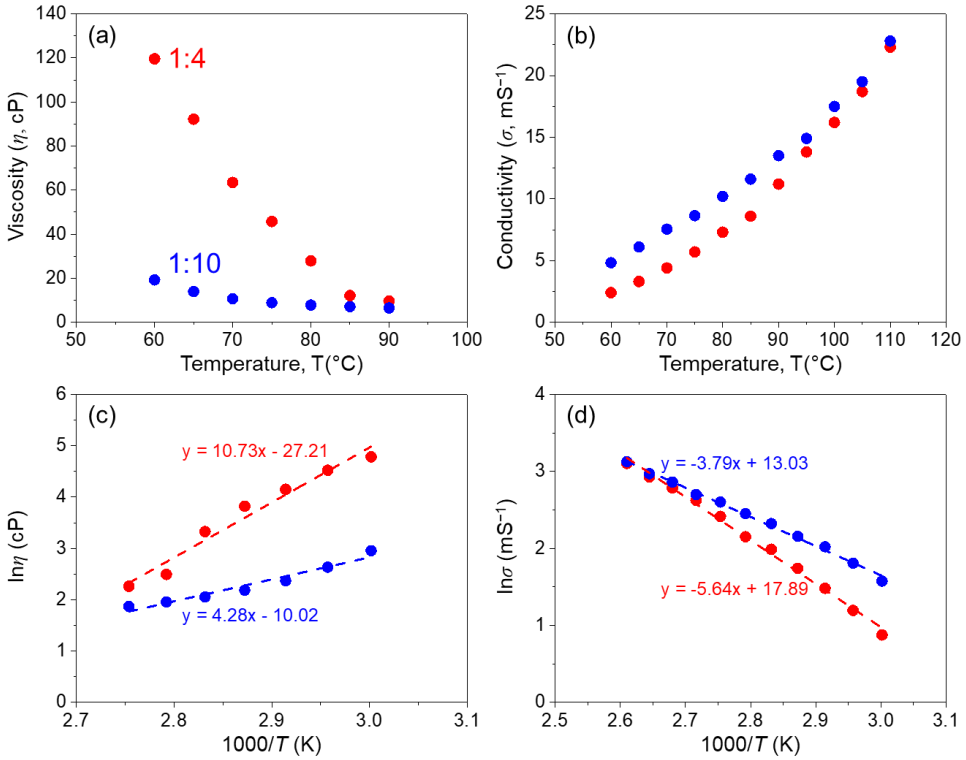

Figure 6–2. (a) Viscosity and (b) conductivity of $FeCl_3$–acetamide mixtures with 1:10 and 1:4 molar ratio. (c, d) Arrhenius plot of the viscosity and conductivity.

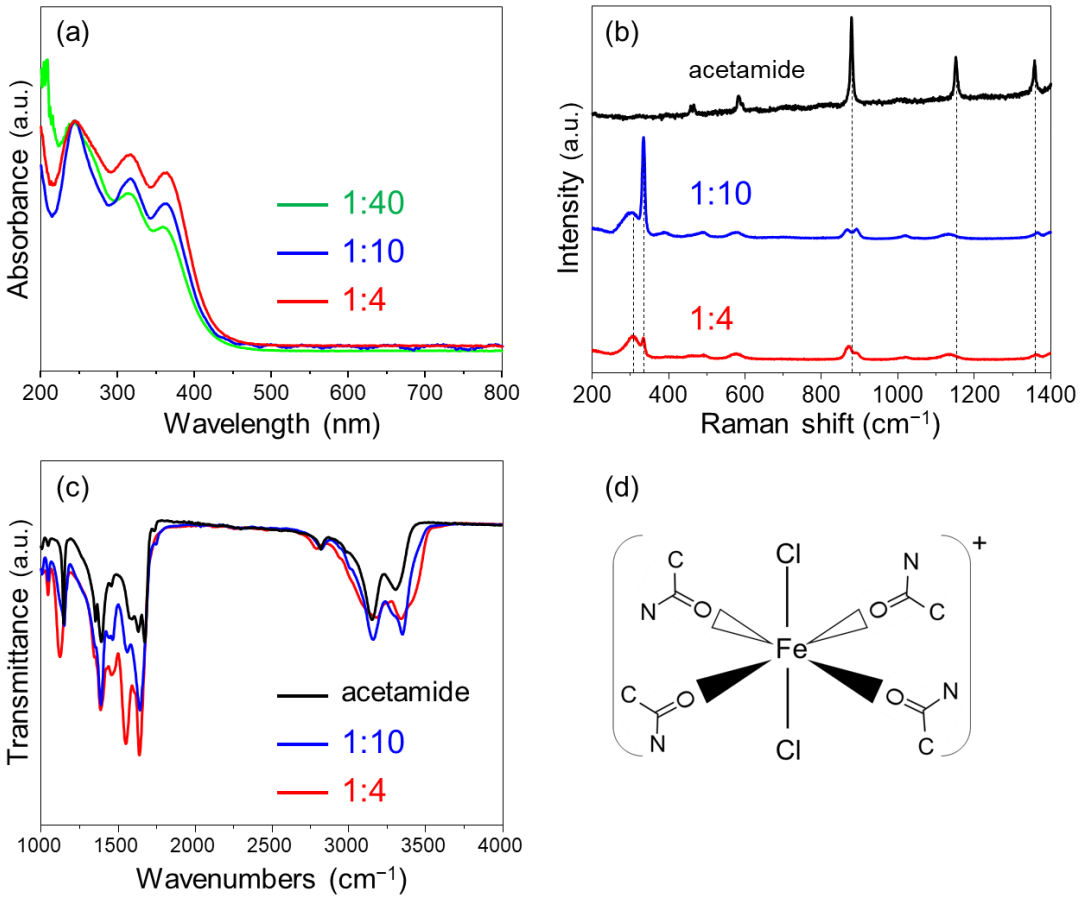

Figure 6–3. a) UV-VIS, b) Raman, c) FTIR spectra of $FeCl_3$-acetamide mixtures with different $FeCl_3$:acetamide molar ratio and d) proposed structure of cationic species.

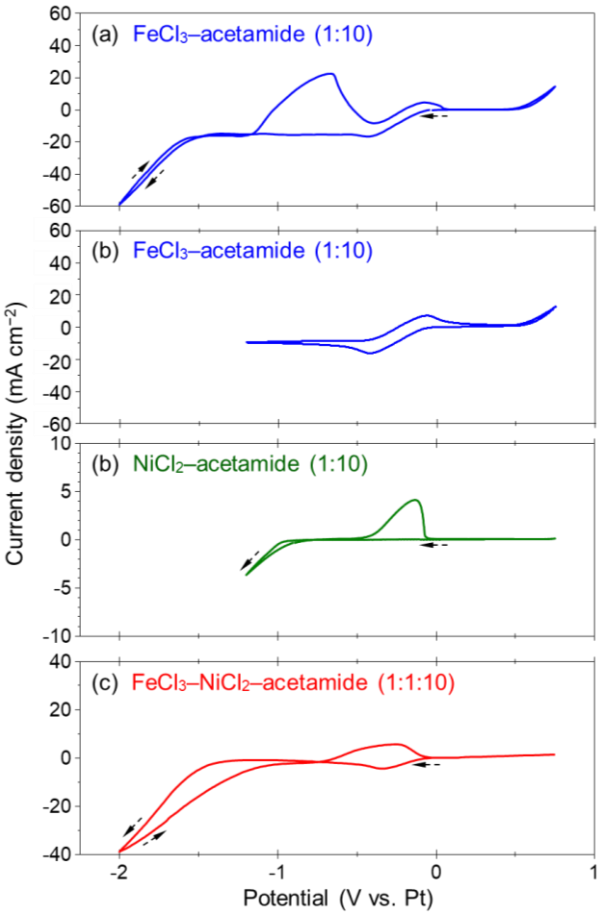

Figure 6–4. Cyclic voltammograms on Pt working electrode at 80 °C and 10 mV s^{-1} in (a, b) $FeCl_3$–acetamide (1:10), (c) $FeCl_3$– $NiCl_2$–acetamide (1:1:10) mixtures.

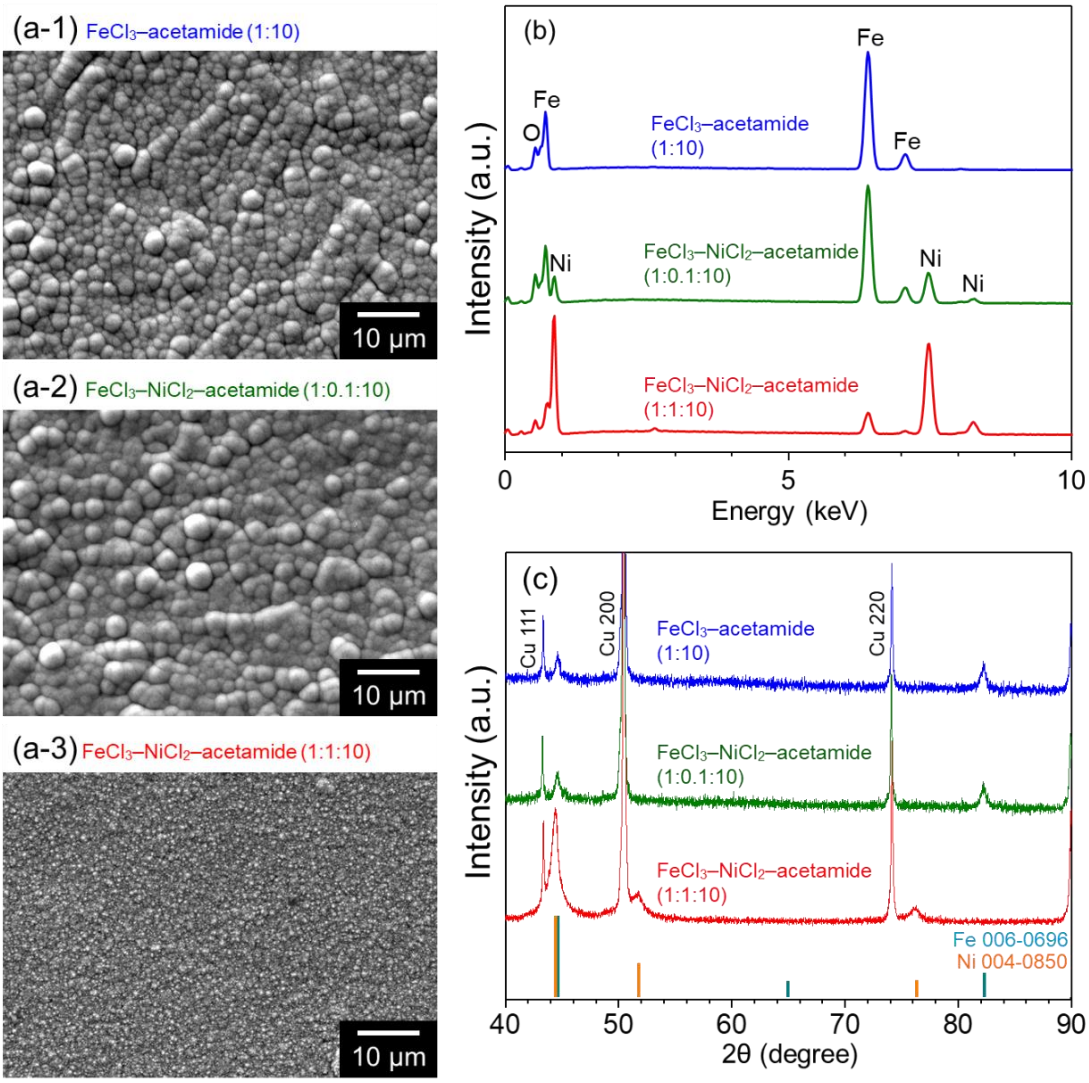

Figure 6–5. (a) SEM images, (b) EDX spectra and (c) XRD patterns of the deposits obtained from 1:10 $FeCl_3$–acetamide, 1:0.1:10 $FeCl_3$–$NiCl_2$–acetamide, and 1:1:10 $FeCl_3$–$NiCl_2$–acetamide mixtures at 80 °C. Current density was 100 mA cm^{-2} for the 1:10 $FeCl_3$–acetamide and 1:0.1:10 $FeCl_3$–$NiCl_2$–acetamide mixtures and 30 mA cm^{-2} for the 1:0.1:10 $FeCl_3$–$NiCl_2$–acetamide mixture.

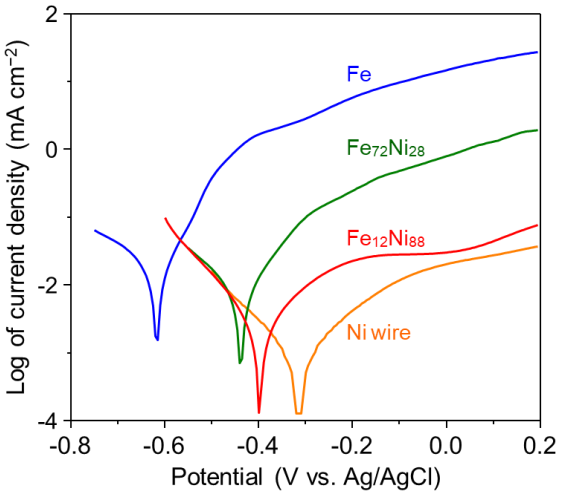

Figure 6–6. LSV curves of Ni wire and Fe, $Fe_{72}Ni_{28}$ and $Fe_{12}Ni_{88}$ deposits obtained from 1:10 $FeCl_3$–acetamide, 1:0.1:10 $FeCl_3$–$NiCl_2$–acetamide and 1:1:10 $FeCl_3$–$NiCl_2$–acetamide mixtures, respectively. LSV was recorded in 0.1 M KNO_3 aqueous solution at room temperature at a scan rate of 5 mV s^{-1}.

Chapter 7

General conclusions

In this thesis, electrodeposition of corrosion resistant Al–W alloy films with a high W content was investigated in EMIC–$AlCl_3$ bath containing W(II) chloride. The electrochemical behavior of Al and W, film morphology, crystallinity, corrosion resistance, and mechanical properties were investigated. The possibility of electrodeposition of elemental W is also discussed. This thesis also proposed a new process to provide the Al–W alloy films with photocatalytic self-cleaning ability through the formation of a WO_3 surface layer. Furthermore, the formation of a DES by the mixture of $FeCl_3$ and acetamide for a low cost non-aqueous electrolyte was also investigated. The results obtained through this work is summarized as follows:

Chapter 2

The electrodeposition of Al–W alloy films in an EMIC–$AlCl_3$ ionic liquid using W(II) chloride (W_6Cl_{12}) as the W ion source was investigated. W_6Cl_{12} dissolved in the ionic liquid at a higher concentration of 49 mM than other W ion sources such as WCl_4 and $K_3W_2Cl_9$, which were used in previous studies. Potentiostatic electrodeposition revealed that dense Al–W alloy films containing up to 12 at.% W were electrodeposited at potentials more negative than 0 V vs. Al/Al(III). W-rich deposits were obtained at potentials of 0 V and more positive values, but no evidence was obtained to confirm that these deposits are composed of metallic W. The deposition current density at > 0 V was lower than 0.3 mA cm^{-2}, whereas that for Al–W alloy films was higher and reached 38 mA cm^{-2} at −0.5 V. The deposition of W was induced by the deposition of Al. At lower W concentrations, the Al–W alloy films were composed of a super-saturated solid solution, and in the W content range of 9–12 at.% they comprised an amorphous phase. Potentiodynamic polarization showed that the Al–W alloy films containing >10 at.% W exhibited high pitting corrosion resistance.

Chapter 3

The hardness (*H*) and Young's modulus (*E*) of the Al–W alloy films with 0–12.4 at% W were examined by nano-indentation. These alloy films were composed of a super-saturated fcc Al solid solution phase when the W content was lower than ~9 at%, and an amorphous phase was formed with higher W contents.

The *H* value increased with increasing W content up to 9.8 at% and then decreased slightly with further increases in the W content up to 12.4 at%. A similar trend was observed in the *E* value with increasing W content, but the decrease in *E* value at 12.4 at% W was more significant than that in *H* value. These changes in the *H* and *E* values were explained by the grain size and the constituent phases. The 9.8–12.4 at% W films exhibited relatively high *H* values and *H*/*E* ratios, and therefore these films were expected to have a higher resistance to mechanical damage than Al films.

Chapter 4

Electrodeposition of Al–W alloy films with high W contents was investigated using EMIC–$AlCl_3$ – W_6Cl_{12} with different $AlCl_3$/EMIC molar ratios. Although the corrosion resistance and hardness of the alloy films are expected to be improved with an increase in the W content, dense films with W contents higher than ~12 at.% were not obtained from the baths with the $AlCl_3$/EMIC molar ratio of 2, as described in chapter 2 and 3. This chapter demonstrated that electrodeposition from baths with a lower $AlCl_3$/EMIC molar ratio can yield Al–W alloys with higher W contents owing to the lower deposition rate of Al and higher solubility of W_6Cl_{12}. The maximum W content of the dense alloy films electrodeposited using the EMIC–1.5$AlCl_3$ bath reached 18 at.%. The hardness (*H*) and Young's modulus (*E*) of the dense and smooth 18 at.% W film were determined by nano-indentation. The *H* and *E* of this film was confirmed to be higher than those of the Al–W alloy films previously obtained from the EMIC–2$AlCl_3$ baths.

Chapter 5

This chapter discussed the feasibility of the formation of WO_3 surface layer on electrodeposited Al–W alloy coatings by selective dissolution of Al and heat treatment, with the aim of providing corrosion-resistant Al–W alloy coatings with photocatalytic self-cleaning properties. The selective dissolution of Al and oxidation of residual W was realized by immersing Al–W alloy films in an aqueous HNO_3 solution. A nanostructured $H_2WO_4 \cdot H_2O$ surface layer was formed on the alloy film by this process. The $H_2WO_4 \cdot H_2O$ layer was dehydrated to cubic or orthorhombic WO_3 by heat treatment 300 or 350 °C, respectively, yielding a multilayered WO_3/Al–W alloy film with an approximately 300 nm thick WO_3 layer. The o-WO_3/Al–W alloy film exhibited photocatalytic self-cleaning, as demonstrated by the photodegradation of stearic acid and methylene blue. Although the resistance of the WO_3/Al–W alloy film to pitting corrosion was slightly lower than that of the untreated Al–W alloy film with the same W content (12 at.%), it was higher than that of the Al–W alloy film with 10.5 at.% W.

Chapter 6

This chapter demonstrated that eutectics of $FeCl_3$ and acetamide are easily formed and a 1:4 molar mixture gives a liquid at ambient temperature. The physicochemical properties and chemical speciation were investigated. Electrodeposition of Fe and Fe–Ni alloys was also demonstrated. These eutectic mixtures have a relatively high conductivity (>10 mS cm^{-1} at 90°C) compared to other eutectics formed from $AlCl_3$ or $ZnCl_2$. UV-VIS, Raman, FT-IR spectroscopy revealed that $FeCl_3$ disproportionates to form both anionic ($FeCl_4^-$) and cationic ($FeCl_2[CH_3CONH_2]_n^+$) species in these mixtures. The electrodeposition of dense Fe and Fe–Ni alloy films was demonstrated and it was shown that the Fe–Ni alloys had improved corrosion resistance.

Future perspectives

In chapter 2–4, corrosion resistant Al–W alloy films were electrodeposited using W_6Cl_{12}, owing to the high solubility of W_6Cl_{12} in EMIC–$AlCl_3$ ionic liquids. However, the mechanism of the dissolution of W_6Cl_{12} remained unclear. Elucidating the dissolution mechanism can lead to development of electrodeposition method for other metals such as Mo and Cr that are less soluble in non-aqueous solutions.

In chapter 2, the possibility of electrodeposition of W was investigated but no evidence to confirm the presence of elemental W was obtained. The W-rich deposits obtained in this study seemed to be some W oxide. The origin of oxygen could be attributed to the water or oxygen in the EMIC–$AlCl_3$ electrolyte or in W_6Cl_{12}. Eliminating the oxygen from the bath can potentially lead to electrodeposition of elemental W.

In chapter 5, a WO_3 surface layer was formed on electrodeposited Al–W alloy coatings by selective dissolution of Al and heat treatment, and photocatalytic self-cleaning properties were demonstrated. A variety of Al based alloys have been obtained by electrodeposition. Therefore, selective dissolution of Al from electrodeposited Al based alloys could also realize other nanostructured materials than WO_3 as in the present study, and many applications such as (photo)catalytic materials and battery electrodes.

In chapter 6, deep eutectic formation of $FeCl_3$ and acetamide was examined and Fe and Fe–Ni electrodeposition from these mixtures was demonstrated. This mixture is of interest as a non-protonic electrolyte for Fe electrodeposition, because the electrolytes used in the previous studies contained OH groups or hydrated Fe species. Using such non-protonic electrolytes can allow for alloying of Fe with less noble elements such as Si, Nd and Al, which are known to improve the magnetic properties of Fe and bring about thermovoltaic properties.

List of publications

Original paper

Chapter 2

Shota Higashino, Masao Miyake, Hisashi Fujii, Ayumu Takahashi, Tetsuji Hirato

Journal of The Electrochemical Society, 164, D120–D125, 2017.

"Electrodeposition of Al–W alloy films in a 1-ethyl-3-methyl-imidazolium chloride–$AlCl_3$ ionic liquid containing W_6Cl_{12}"

Chapter 3

Shota Higashino, Masao Miyake, Ayumu Takahashi, Yuya Matamura, Hisashi Fujii, Ryuta Kasada, Tetsuji Hirato

Surface and Coatings Technology, 325, 346–351, 2017

"Evaluation of the hardness and Young's modulus of electrodeposited Al–W alloy films by nano-indentation"

Chapter 4

Shota Higashino, Masao Miyake, Hisashi Fujii, Ayumu Takahashi, Ryuta Kasada, and Tetsuji Hirato,

Materials Transactions, 59, 944–949, 2018.

"Electrodeposition of Aluminum–Tungsten Alloy Films Using EMIC–$AlCl_3$–W_6Cl_{12} Ionic Liquids of Different Compositions"

Chapter 5

Shota Higashino, Masao Miyake, Takumi Ikenoue, and Tetsuji Hirato,

Scientific Reports, 9, 16008, 2019.

"Formation of a photocatalytic WO_3 surface layer on electrodeposited Al–W alloy coatings by

selective dissolution and heat treatment”

Chapter 6

Shota Higashino, Andrew P. Abbott, Masao Miyake, and Tetsuji Hirato,

Electrochimica Acta, 351, 136414, 2020.

“Iron(III) chloride and acetamide eutectic for the electrodeposition of iron and iron based alloys”

Oral presentations

International conference

Shota Higashino, Masao Miyake, Takumi Ikenoue, and Tetsuji Hirato

“Electrodeposition of Al–W Alloy Films Using W(II) Salts Synthesized Using Different Methods”

236th ECS Meeting, Atlanta, Georgia, October, 2019

Shota Higashino, Masao Miyake, Takumi Ikenoue, and Tetsuji Hirato

“Formation of a photocatalytic WO_3 layer on electrodeposited Al-W alloy films by selective leaching and heat treatment”

Joint International Symposium on Energy Science between Kyoto University and Indian Institute of Science, Indian Institute of Science, Bangalore, India, December, 2018

Shota Higashino, Masao Miyake, Takumi Ikenoue, and Tetsuji Hirato

“Electrodeposition of Al–W Alloys and Surface Modification by Anodization”

22nd Topical Meeting of the International Society of Electrochemistry, Tokyo, Japan, April, 2018

Shota Higashino, Ayumu Takahashi, Ryuta Kasada, Masao Miyake, and Tetsuji Hirato

"Mechanical Properties of Electrodeposited Al-W Alloy Films and the Effects of Subsequent Heat Treatment"

PRiME 2016, The Electrochemical Society, Honolulu, Hawaii, USA, October, 2016

Domestic conference

Shota Higashino, Masao Miyake, Takumi Ikenoue, and Tetsuji Hirato

"Formation of a photocatalytic surface layer on electrodepostited Al–W alloy films by selective dissolution"

138th meeting of the Surface Finishing Society of Japan, Hokkaido University of Science, September, 2018

Shota Higashino, Ayumu Takahashi, Hisashi Fujii, Takumi Ikenoue, Masao Miyake, and Tetsuji Hirato

"Electrodeposition of Al–W alloy films from ionic liquids containing a W(II) salt"

133th meeting of the Surface Finishing Society of Japan, Waseda University, March, 2016

Poster presentation

Shota Higashino, Masao Miyake, Takumi Ikenoue, and Tetsuji Hirato

"Electrodeposition and Anodization of Al–W Alloy Films"

232nd ECS Meeting, The Electrochemical Society, National Harbor, MD, USA, October, 2017

Shota Higashino, Ayumu Takahashi, Masao Miyake, Ryuta Kasada, Tetsuji Hirato

"Electrodeposition of Al–W Alloy Films from Ionic Liquid and Evaluation of Their Corrosion Resistance and Mechanical Properties"

229th ECS Meeting, The Electrochemical Society, San Diego, CA, USA, May 2016

Shota Higashino, Ayumu Takahashi, Masao Miyake, Ryuta Kasada, and Tetsuji Hirato

"Nano-indentation study of electrodeposited Al–W alloy films"

The 7th International Symposium of Advanced Energy Science, Institute of Advanced Energy, Kyoto, September, 2016

Acknowledgement

The author would like to express his deepest gratitude to Professor Tetsuji Hirato at Kyoto University for his supervision. The continuous support, guidance and encouragement he gave me throughout study have been a true blessing. The author is most grateful to Professors ?? and ?? for reviewing this thesis and giving a lot of invaluable instructions. The author is sincerely grateful to Associate Professor Masao Miyake for his detailed instructions and fruitful discussions. The author believes that this thesis has reached its present form owing to his immeasurable amount of help and guidance. The author is grateful to Assistant Professor Takumi Ikenoue for his continuous discussion and help on variety aspect of this study.

The author would like to thank Professor Ryuta Kasada at Tohoku University for the fruitful discussion on nanoindentation, and Associate Professor Masakatsu Hasegawa for his kind help on chemical synthesis.

The author is grateful to Professor Andrew Abbott at University of Leicester for hosting the author as a visiting scientist and for his supervision. Special thanks must be paid to Dr. Robert Harris, Dr. Jennifer Hartley, Dr. Stephen Viles, Dr. Igor Efimov, Dr. Chunhong Lei, Dr. Ioanna Maria Pateli, Dr. Stylianos Spathariotis, Mr. Jack Allen, and Mr. Graham Clerk. They made the life in Leicester enjoyable and comfortable.

The author greatly thanks Mr. Suguru Shiomi, Mr. Hisashi Fujii, Mr. Ayumu Takahashi, Mr. Yuya Matamura, Mr. Yoshikazu Takeuchi and all the people in the Materials Processing group in Energy Science Department for their kind help and the fruitful discussion throughout this study. Especially, Ms. Sachiko Yamamoto provided countless arrangements to make a comfortable environment for this study.

The author sincerely appreciates the financial aid from Japan Society for the Promotion of Science. The author would like to thank all his family and friends for their heartful encouragement. The author believes that their continuous assistance was indispensable for accomplishing this study. The author is

particularly grateful to his parents, Masahiro Higashino and Ryoko Higashino for their kind support and encouragement.